Study of interaction effects in magnetic granular systems for recording media application

Sergiu Ionel Ruta

Doctor of Philosophy

University of York
Physics

September 2017

Abstract

Magnetic nano-systems have a wide scope of applications ranging from data storage technologies to biomedicine. In data storage devices the information is encoded in the grain magnetisation corresponding to bit "0" and "1". The recording media industry is driven by increasing the areal density of stored data and decreasing cost, while in the same time maintaining the thermal stability and signal-to-noise ratio. For this, close-packed 2-dimensional granular systems are used, with nanometre grain size. The quality of such magnetic recording media depends on the intrinsic material properties and on the inter-granular coupling via exchange and magnetostatic interaction.

The work presented here studies the effects of inter-granular coupling and investigates different approaches to extract intrinsic properties from the bulk measurements. Due to the irregular shape of the grains, the dipole approximation for magnetostatic interaction is inaccurate. For higher accuracy, a 5-fold numerical integral is required for each pair of grains. Analytical integration over the grains height is possible reducing the numerical calculation to a 3-fold integral. The competition between the exchange and magnetostatic interactions leads to complex magnetic structures and correlated behaviour, where groups of grains behave collectively. The effects are observed and studied here based on the magnetic radial correlation function which shows a damped oscillatory form as a function of grain separation. The correlation length increases with increasing exchange interaction. An important consequence of correlated behaviour is that it alters the intrinsic switching field distribution (SFD), leading to an effective SFD. The intrinsic SFD is a fundamental characteristic of granular magnetic materials, defined as the distribution of irreversible switching events of magnetic grains in the absence of inter-granular interactions. Separating the intrinsic SFD from the effective SFD remains a challenge. Two methods that have been widely used to extract the intrinsic SFDs from hysteresis based measurements, the so-called FORC method and the $\Delta H(M,\Delta M)$-method are compared. It is shown here that the FORC diagrams contain useful information about the interactions in the system, but the ability to extract the intrinsic SFD is limited to the system in which the magnetic correlations can be neglected. Identifying the SFD from hysteresis loop measurements in the parameter range relevant for applications, requires applying the inverse problem solving techniques such as the $\Delta H(M,\Delta M)$-method.

Table of contents

List of tables

List of figures

I would like to dedicate this thesis to my loving parents …

Acknowledgements

I would like to express my gratitude firstly to Professor Roy Chantrell for his tremendous guidance, support and help as my supervisor and as my mentor. I want to thank him for the fruitful discussion and for the many opportunities he has given me.

I would like to thank Ondrej Hovorka for the discussion, guidance and the productive collaboration over the years. I would like to thank Ganping Ju, Pin-Wei Huang and Kangkang Wang from Seagate Media Research, Fremont for providing experimental measurements, giving me the opportunity to visit them and have productive discussion. I would also like to thank collaborators who have constantly stimulated my work and provided help: Alexandru Stancu, Andreas Berger, James Miles, Chih-Huang Lai, Ming-Da Yang, David Serantes, Dieter Weller, Vlado Lazarov.

I thank my colleagues for the help and support they provided me, Tom, Richard, M. Ellis, Andrea, Mara, Razvan, Oscar, Jung-Wei, Lewis, Jessada, Cristina, Zuwei, Sam, Ewan, Oliver, Sarah, Daniel, Yifan.

Last but not least I would like to thank my family and friends for their friendship and support.

Declaration

I declare that this thesis is a presentation of original work and I am the sole author. This work has not previously been presented for an award at this, or any other, University. All sources are acknowledged as References. The results in Chapter 5 are published in the following article: Ruta, Sergiu, et al. "First order reversal curves and intrinsic parameter determination for magnetic materials; limitations of hysteron-based approaches in correlated systems." Scientific Reports 7 (2017): 45218.

Chapter 1

Introduction

The origin of magnetism comes from the quantum physics, but at a macroscopic level, a magnetic material can be described classically [1, 2]. The characterisation of magnetic materials can be done in a simple way, using the magnetic moment ($\vec{\mu}$) or magnetisation (M) and magnetic field (H). A magnetic field is created either by an electric current, as discovered by Oersted in 1819 [3] or by a magnet. For the first case, a current, i, passing through an elemental length of a conductor, ∂l, creates at distance r, a magnetic field given by the Biot-Savart law [3]:

$$\partial \vec{H} = \frac{1}{4\pi r^3} i \partial \vec{l} \times \vec{r} \tag{1.1}$$

The response of a material to an external magnetic field is described by the magnetic susceptibility:

$$\chi = \frac{dM}{dH} \tag{1.2}$$

M and H are considered to be collinear in the assumption of a small field. Here is worth mentioning that in the magnetism community alongside the SI units system, the CGS (centimetre–gram–second) is also used. In this work, CGS units are considered, with the conversion factors being listed on the IEEE Magnetics Society website [4].

The magnetisation is the average magnetic moment of the material per unit volume. For each atom, the electrons are arranged in orbitals on layers based on the quantum number and Pauli exclusion principle. The magnetic moment arises from the orbital angular momentum and the spin. The spin number is odd multiples of one half having both positive and negative values. If the number of spin with opposite value are compensated then the material is diamagnetic. A diamagnetic material has weak repulsion from the applied field and respectively a small negative susceptibility. The other scenario is of uncompensated spins, which lead to a net magnetic moment quantified in Procopiu-Bohr moment (commonly as Bohr moment). Classically the magnetic moment can be considered as a magnetic dipole, with the mention that there is no magnetic charge.

In any material, the atoms are arranged in a crystallographic lattice and interact via localised and itinerant electrons. For magnetic properties, the two most important interactions are the magnetostatic interaction and the exchange interaction. The latter is a pure quantum effect and does not have any classical analogy. In a simple way, the exchange can be mathematically described as a coupling strength J between spins. If the exchange interaction is positive, all spins are aligned in the same direction giving rise to ferromagnetic ordering. The thermal effects tend to misalign the spins and therefore there is a competition between exchange and temperature. With increasing temperature, the total magnetic moment of a material, known as saturation magnetisation (M_s), decreases to zero at a critical temperature called the Curie temperature (T_c). At this temperature, the material has a phase transition from ferromagnetic, below T_c, to paramagnetic, above T_c. If the magnetic coupling is negative, this leads to antiferromagnetic behaviour.

The magnetic susceptibility is not necessarily the best way of describing the response of a magnetic material as M can have a complex, non-linear dependence on H or even can be a non unique function. This gives rise to magnetic hysteresis, which will be introduced shortly.

An alternative description of the magnetic response is using the energy of the system, which can have multiple contributions. Here we consider 4 of them: applied field, anisotropy, magnetostatic interaction and exchange interaction. The temperature will be considered afterwards. To describe the properties of the four factors a generic magnetic entity is considered as a dipole moment $\vec{\mu}$. The magnetic entity can be either an atom, a large magnet such as a compass needle or a small volume element of a larger material body. If the magnetic dipole is in an external magnetic field, the field will produce a torque on the dipole, which tries to align the moment on the field direction, leading to a applied field energy, Zeeman energy, of:

$$E_z = -\vec{\mu} \cdot \vec{H} \tag{1.3}$$

This effect is the base of the magnetic compass, where the needle free to rotate in a liquid aligns parallel with the Earth magnetic field.

If there is no applied field, the magnetic moment can either be oriented randomly as in a paramagnet or can have one or more preferential directions, labelled easy axes. In the first case (isotropic case) the energy is the same for all orientations of the magnetic dipole. There are multiple types of anisotropy discussed in great details in reference [2], such as magnetocrystalline, shape, surface, magnetoelasticity. The simple case is of uni-axial anisotropy, where the energy depends on even powers of magnetic moment projection on the preferential direction:

$$E_{ani} = -K_0 V - K_1 V cos(\theta)^2 - K_2 V cos(\theta)^4 - ... \tag{1.4}$$

The first term, K_0 is the isotropic term, with the same energy for all orientation of the magnetic moment and in most cases is ignored as it does not influence the magnetic properties. The second term, K_1, is the dominant term, with the higher terms being orders of magnitude smaller and can be ignored [2]. Although the entire expression above is for uniaxial anisotropy, just the first term is extensively used in magnetism. For this case, the anisotropy field is defined as:

$$H_k = \frac{2K_1}{Ms} \tag{1.5}$$

The uni-axial anisotropy, K_1, together with the applied field are the crucial elements in many application of magnetic materials. First, the anisotropy defines the hysteresis behaviour of magnetisation versus field, M(H), in which the magnetic response to a change of an external field depends on the current magnetic moment orientation. For the applied field and easy axis in Z-direction, an example is illustrated in figure 1.1. In zero applied field there are two possible orientation of the magnetic moment, corresponding to the minimum energy: $\theta = 0$ or π (fig/ 1.1). Each of the two states can be accessed depending on the starting conditions. If the moment was initialised in a large positive field ($H_{ap} >> H_k$) and then the field reduced to zero, the $\theta = 0$ state is accessed. If the moment was initialised in a large

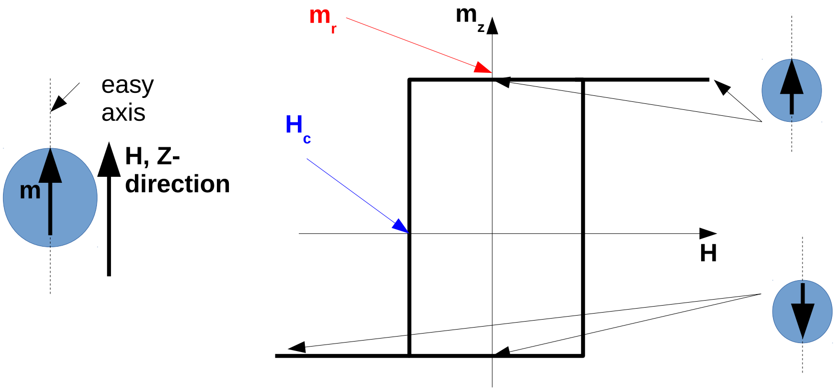

Fig. 1.1 Hysteresis loop for the dependence of magnetisation as a function of applied field strength. The applied field and easy-axis are parallel to each other along the Z-direction.

negative field ($H_{ap} >> H_k$) and reduced to zero, the second state is accessed. Applying an external magnetic field on a magnetic sample, sweeping from a large positive value to a large negative value and then back to a positive, give rise to the hysteresis loop in figure 1.1. The hysteresis loop is defined as the projection of the magnetic moment on the field direction as function of field amplitude ($\vec{m} \cdot \vec{H}$), where m is the unit vector of magnetic moment μ. The hysteresis loop is characterised by the value of magnetisation in zero field, the remanent magnetisation (or remanence), and the coercivity field. The coercivity field is the value of the applied field for which the magnetisation is zero. In this particular example, the remanence is 1 and the coercivity field equals anisotropy field.

The exchange interaction is particularly important at the atomic level and was first described by Heisenberg in 1928 as a quantum mechanical exchange [1, 5]. This is a direct exchange interaction at the atomic lattice sites, caused by overlapping of electronic wave functions. The exchange energy is given by the Heisenberg Hamiltonian:

$$E_{exch} = \sum J_{ij} \vec{S}_i \cdot \vec{S}_j \tag{1.6}$$

where J_{ij} is the exchange coupling and S_i, S_j are the magnetic moment unit vectors of the atom i and j. The exchange interaction is a short range effect with the upper limit at nm scale. To have a correct description of the exchange interaction, first principles calculations are required. The work presented here does not include such calculation, and therefore will not discuss further the calculation of exchange interaction. As mentioned previously, exchange interaction defines a ferromagnet or antiferromagnet based on the sign of exchange and the transition to a paramagnet at the Curie temperature.

In contrast to exchange interaction, the magnetostatic interaction is long ranged and becomes significant for system sizes larger than nm scale. For two magnetic moment (i and j), treated as dipoles, the magnetostatic energy is given by the dipole field:

$$\vec{H}_{ij} = \frac{M_s V}{4\pi r_{ij}^3} \left[\frac{3(\vec{m}_j \cdot \vec{r_{ij}})\vec{r_{ij}}}{r_{ij}^2} - \vec{m}_j \right] \tag{1.7}$$

where r_{ij} is the distance between the centre of the magnetic moment i and j. $M_S V$ is the amplitude of the magnetic moments.

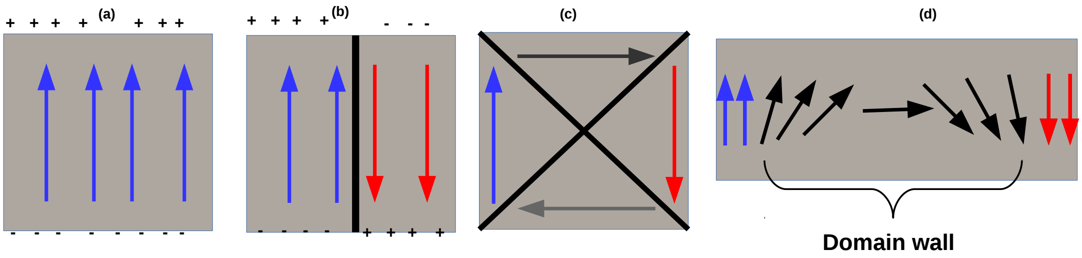

Fig. 1.2 Magnetic moment configuration for a single domain (a), two domains (b) and 4 domains (c). (a) and (b) are characteristic for perpendicular magnetisation and (c) is characteristic for in-plane magnetisation. An example of domain wall for the configuration in (b) is illustrated in (d).

1.1 Mono-domain limit

The system behaviour will be determined by minimisation of the total energy [6]. For a ferromagnetic material, there is a competition between the exchange interaction, which wants to align all moments parallel and the magnetostatic interaction which tends to minimise the formation of "free poles" by creating closed flux structures. A domain is a configuration in which all moments are parallel to each other. In figure 1.2a the system is in a single domain as preferred by the exchange interaction. For explanation purposes the top and bottom surfaces can be described as having respectively a net positive "magnetic charge" and negative "magnetic charge". This configuration produces a large internal magnetostatic field, giving rise to a high energy state since the magnetostatic interaction opposes the net magnetisation of the sample. The magnetostatic field can be reduced by having two domains with opposite orientation (figure 1.2 b). The domains are separated by a transition region called a domain wall in which the magnetic moment gradually changes orientation from one domain to the other (fig. 1.2d), which increases the exchange energy. The magnetostatic interaction is reduced even more in configurations similar to the one figure 1.2c, but the domain walls length and energy increases. The domain wall width is given by:

$$Dw \approx \sqrt{\frac{J}{aK_1}} \tag{1.8}$$

J is the exchange energy and a is the lattice parameter. A narrow domain wall lowers anisotropy energy, but costs exchange energy, whereas large domain walls are preferred by exchange interaction but increase the anisotropy energy. The competition between exchange energy and magnetostatic energy is described by the exchange length:

$$l_{ex} \approx \sqrt{\frac{J}{aM_s^2}} \tag{1.9}$$

If the size of the system is decreasing, the number of domains in the system will decrease as well. There is a critical size, below which just a single domain is possible. The single domain structure is called a mono-domain particle. The combination of two characteristic lengths gives the critical size for a single domain particle. For a spherical particle the critical single-domain radius is [2]:

$$R_{sd} \approx \frac{36\sqrt{JK_1/a}}{Ms^2} \tag{1.10}$$

Calculating the mono-domain particle size is a complicated problem as it depends on the material, saturation magnetisation, anisotropy and other factors such as the shape of the particle. For example, an elongated particle will have a lower magnetostatic energy, which will increase the single domain size.

1.2 Thermal effects

Here a mono-domain particle is considered with volume V and uni-axial anisotropy. In figure 1.1 we defined 2 stable states for the magnetic moment in zero field. The two states are separated by an energy barrier E_b. At 0K the particle is trapped in the state based in the initial orientation. In the presence of temperature, there is a probability of the particle to receives enough energy from the thermal bath, to overcome the energy barrier and the particle to change its state. The process can be expressed by the Arrhenius-Neel relaxation time:

$$\frac{1}{\tau} = f_0 exp(\frac{-E_b}{K_b T}) \tag{1.11}$$

where f_0 is a characteristic frequency, referred to as the attempt frequency and k_b is the Boltzmann constant. The value of f_0 depends on the system properties, but in many cases is used as a constant with the value of 10^{-9} s^-1. Due to the random thermal fluctuations, this is a statistical process, in which the average magnetisation over a large ensemble will exponentially decrease to its equilibrium value. For the case of uniaxial anisotropy with no external field the switching probability as function of time can be written as:

$$P(t) = \frac{1 - exp(t/\tau)}{2} \tag{1.12}$$

The characteristic time of the exponential decrease is the relaxation time and it defines the magnetic stability with respect to the measurement time, e.g. the applied field sweep rate for a hysteresis loop:

- If the measurement time is much shorter than the relaxation time ($t_m << \tau$), the particle at each field value remains in its initial state. The transition between two possible states due to thermal fluctuations is not allowed within the measurement time. In this case, the magnetic behaviour is temperature independent and is referred to as the blocked state. The coercivity field is equal to the 0K value. The same for remanent magnetisation.
- If the measurement time is much larger than the relaxation time ($t_m >> \tau$), the particle is unstable. The thermal energy, k_bT, is sufficiently large that in the measurement time, the particle can overcome the energy barrier and the magnetic moment fluctuates between the two possible states. During a hysteresis measurement, at each field value the magnetic moment, switches from one state to the other multiple times, such that the average magnetic moment over a large ensemble achieves the equilibrium value at that field. The magnetisation curve does not have hysteresis and it can be described in a first approximation by the Langevin function. This effect is similar to the behaviour of a paramagnetic material and is referred as the superparamagnetism. The coercivity field and remanence are 0. For typical VSM measurements with a timescale of 100s, one can define a critical volume for superparamagnetic behaviour such that $KV_{cr} \sim 25kT$.
- For particle sizes $V > V_{cr}$ the measurement timescale is too short for spontaneous switching and are often referred to as 'blocked'. Magnetisation reversal is thermally driven at a field at which the measurement time is equal to the relaxation time. The hysteresis loop shape is between the 0K and equilibrium curve (e.g. the Langevin function) as the system of particles tends towards the equilibrium magnetisation curves but does not have enough time to actually reach it. Both coercivity and remanence have a dependence on the measurement time, varying from the zero at large time scale to the 0K value at short time scale (fig 1.3a).

The 3 conditions are reflected in figure 1.3a, where the coercivity is given as a function of the field sweep rate (R), which is the slope of the field variation in time. Based on equation 1.11, two characteristic properties can be defined considering the energy barrier proportional

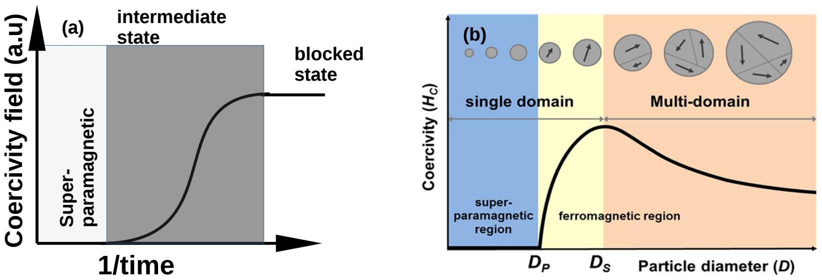

Fig. 1.3 For single domain particle, the coercivity is time independent at short time scale and decreases with increasing time up to the superparamagnetic limit, where the hysteresis behaviour disappears (a). In terms of particle size, there are two limits: upper limit towards multi-domain and a lower limit for superparamagnetism (b). Figure (b) is taken from reference [7].

to the product of anisotropy and volume of the particle, $E_b = KV$. For a given particle, the temperature above which the particle is superparamagnetic is called the blocking temperature:

$$T_B = ln\left(\frac{1}{t_m f_0}\right)\frac{E_b}{k_b} \tag{1.13}$$

Analogously, a critical volume can be calculated, below which the particle is superparamagnetic:

$$V_{cr} = (t_m f_0)\frac{k_b T}{K} \tag{1.14}$$

The relevant physics of ferromagnetic materials in a wide range of applications requires hysteresis behaviour. Therefore, if we consider mono-domain particles there are two limits in term of size (fig. 1.3b): an upper limit so that there are no multi-domains and a lower limit for the superparamagnetic effect, when the hysteresis disappears. Next, we will continue the discussion on information storage in magnetic recording media.

1.3 Magnetic recording media

Magnetic recording consists of a two dimensional system of particles or grains on which the information is stored and a read and write head [8]. The information is stored as a bit, 0 or 1, ideally on a single grain which has two well defined states. In reality, the information is stored in a number of grains (10-20 grains). The required criteria for a magnetic storage system are:

1. large magnetisation saturation to produce a clear signal in the read head.
2. Coercivity field that allows writing the information by switching the magnetic moment from one state to the second.
3. large thermal stability for the stored information to be preserved for years.

The last two are currently been study for storage improvements. Based on this criteria IBM introduced in 1956 the IBM 350 Disk Storage, which had a 5Mb capacity and had the size of a human. From that point, the magnetic hard disk drives (HDD) industry, requires a continuous improvement in the area density ($bits/in^2$), which pushes the technology to its limits [8]. The density increased from $0.01Gb/in^2$ in 1980 to over $100.0Gb/in^2$ in 2006 when the perpendicular recording was introduced. The storage capacity increased exponentially during this period, with the device size decreased to the current size. To reach such limits, the grain size was reduced and nowadays the superparamagnetic effects pose a challenge.

The current technology is based on the perpendicular magnetic recording (PMR) in thin films. The magnetic moment is aligned perpendicular to the thin film. The structure of PMR consists of 4 layers, a soft magnetic underlayer, a seed or intermediary layer, the recording layer and a protection layer. The latter protects the recording layer from mechanical damage. The soft magnetic layer has the role of mirroring magnetic pole from the write head, which enhances and confines the write field perpendicular to the thin film in a single bit region, with minimum effect on neighbouring grains [9]. The soft magnetic underlayer helps to increase the writing field, which allows writing on a media with a larger coercivity field. In this way, the areal density can be increased by decreasing the grain size and increasing the anisotropy so that the thermal stability factor KV/k_bT remains large. The seed layer has two important roles: it decouples the underlayer from the recording layer and promotes the growth of recording layer with a perpendicular easy axis. The recording layer consists of CoCr alloys such as CoCrPt, CoCrTa, CoCrPtNb [10, 9, 11, 12]. The big challenge in developing media for products of increasing areal density is the so-called ’trilemma’, which we now consider. [13].

Any design of new HHD aims at reducing the area per bit but maintaining the signal to noise ratio (SNR). The SNR dependent on the numbers of grains per bit and also dependent on the switching field distribution. The intrinsic switching field distribution (SFD) is a fundamental characteristic of granular magnetic materials and it determines the quality of recording media used in hard disk drives. The switching field is the field required to switch the grain from one state to the other one. It is not the macroscopic coercivity that defined the quality of recording media, but the microscopic local switching field in the geometry characterising a single bit. The tails of the distribution constitute a source of errors. The grains with large switching field, above the maximum writing field, will not switch in the field direction and contribute to errors. Also, the grain with small switching field are thermally unstable and will lead to information loss. The SNR depends on the ratio between the grains contributing to information storage (centre part of SFD) and the grains leading to errors (the tails of SFD) for every single bit. A large SFD width implies a larger contribution to the tails of SFD and therefore a decrease in the ratio between storage grains and the error grains. To keep the SNR to the desired level it is required to increase the number of grains per bit, which will improve the mentioned ratio.

One way of increasing the area density is reducing the number of grains per bit until a bit corresponds to a single grain (BPM-bit pattern media). The technology required to achieve BPM at the current cost of HDD is not accessible yet. Assuming that the number of grain per bit remains constant, the alternative is reducing the grain diameter. However, a smaller grain leads to lower energy barrier KV/k_bT. The Arrhenius-Neel law requires an energy barrier of 40 k_bT for information storage up to 10 years at room temperature (300K). In practice, a larger value is considered to take into account the effect of interactions with neighbouring grains [14]. To keep the energy barrier fixed the anisotropy requires to increase inverse proportionally to the grain volume (for cylindrical grains $K_{new}/K_{old} = (D_{old}/D_{new})^2$, assuming constant height). If the size decrease to half, the anisotropy need to increase by a factor of 4. These considerations are for a single-domain grain with uni-axial anisotropy perpendicular to the thin film. To write the bits, the writing field needs to increase as well because of the increased coercivity. The writing field is limited to a maximum of 20-30kOe, although around 10kOe are the practical value considered. [8, 13]. Any new recording media design needs to compromise between the writability, SNR and thermal stability. Any new technology needs to find a way around the trillema [13].

Based on the ASTC (Advanced Storage Technology Consortium) road map, there are two future technologies: BPM and heat assisted magnetic recording (HAMR) [15]. Also for the PMR, there are ways, already used to get around the recording trillema: CGC (Coupled Granular Continuous) recording media, ECC (Exchange Coupled Composite) media or a combination of both ECC/CGC media.

In theory, the easiest way to increase the area density is to decrease the number of grain per bit up to 1 grain per bit in BPM [16]. The main problem consists of the randomness of grains position and properties. In conventional PMR, the problem is solved by considering a number of grains per bit, so that the non-uniformities are averaged out. BPM requires lithographic patterning of discrete magnetic dots with uniform properties. In the ideal case, it can reach up to $300Tb/in^2$. The main limitation is in the systematic and consistent production of the dots [17].

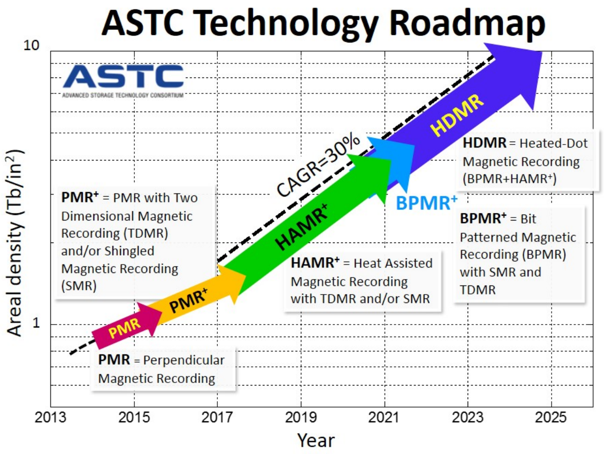

Fig. 1.4 Road map of recording media provided by ASTC in 2014 [15].

HAMR media is a technology initiated by Seagate in the 1990s [18]. High areal density above $1Tb/in^2$ is achieved by using high anisotropy material such as FePt [19]. To overcome the writability problem, during the writing process, a laser is used to heat up the grains. With temperature increase both the magnetisation and anisotropy are decreased, reducing the coercivity of the grains below the writing field. After the writing process, the heat is dissipated in a heat sink underlayer and the initial anisotropy value is recovered, preserving in this way the thermal stability. Although Seagate has presented a fully working HAMR HDD [20], the devices are not yet available on the market indicating that there is still significant area density progress in PMR.

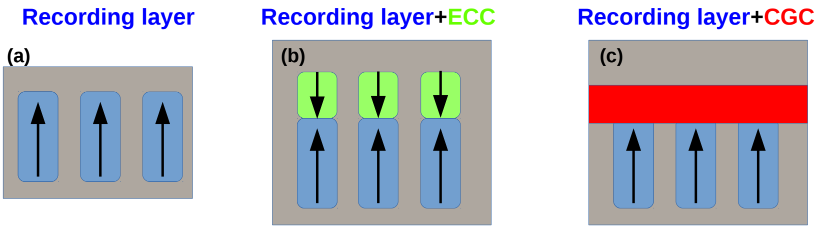

Fig. 1.5 Schematic representation of perpendicular recording media -PMR (a), coupled granular/continuous PMR (b) and exchange coupled composited PMR (c).

1.3.1 Multilayer recording media

To postpone the trilemma in the PMR, several works suggested using multilayer films to overcome writability and thermal stability issues using interlayer exchange coupling effects (fig. 1.5). Sonobe et al. proposed coupled granular/continuous (CGC) perpendicular media consisting of a continuous multilayer and a granular host layer ((fig. 1.5c) [21]. A single granular layer of PMR (fig. 1.5a) has the problem of a large magnetostatic field, perpendicular to the film. If the grains are well separated there is no exchange coupling. In the uniform magnetised layer, in zero applied field, there will be a net effective field from the demagnetisation of $4\pi M_s$. Due to this field, the hysteresis loop inclination is changed from the rectangular shape. This effect is called shearing. Importantly the demagnetisation field reduces the thermal stability of recording media. The continuous layer is exchanged coupled and also induces an indirect lateral exchange coupling of the granular layer. The effect of magnetostatic is compensated with exchange interaction induced by the continuous layer, restoring the rectangular shape of the loop and the thermal stability. After multiple iterations of CGC structure, it was proven experimentally that PMR with CGC has an overall better thermal stability increasing the KV/k_bT ratio and improved SNR [22, 23, 10, 24, 21]. Smaller grains and larger anisotropy were possible up to the limit of the writing field.

To overcome the writability problem the exchange coupled composited (ECC) media was proposed [25–28]. The work of [28, 29] suggest that an ECC structure will have a reduced coercivity. Also, the SFD and thermal stability factor (KV/k_bT) is increased, solving two of trilemma criteria: the writability and the thermal stability [29]. The structure of the recording media is made of two granular layers one on top of each other with decoupling lateral exchange, and with vertical exchange coupling between the two layers ((fig. 1.5b). The recording layer has a large anisotropy for thermal stability and the other is a soft layer which assists the reversal of the recording layer. Having both CGC and ECC effects are desired and recording media with these type of layer are considered [30]. This allows controlling the lateral exchange, which helps the stability of data and vertical exchange which controls the switching field. Optimising both effects are important not just in term of two previously mentioned effects but also in terms of SFD. The SFD and methods of extracting the SFD are studied in this work considering just the recording layer, with CGC and ECC effects included in the model parameters. The new structure based on CGC and ECC allows to tune the interaction strength and especially the balance between magnetostatic interaction and exchange interaction. This new option requires the study of correlation induced in the system by the interactions. The ideal SFD, bit size, saturation magnetisation will depend on the correlation length [31–37].

Chapter 2

Theoretical models of mono-domain particles

The magnetic behaviour of materials is complex and can not be described by a single theory/model on all time and length scales. There are different levels of approximation going from a continuous description at the macroscopic level to a discrete description at the atomic level. At the atomic scale, the magnetic properties can be calculated from the electronic structure provided by quantum physics using first principles techniques. There are a large number of electronic structure codes, but all of them are limited to thousands of atoms [38]. The are also limitations in describing thermal effects and dynamical properties. Nevertheless, they provide crucial information for higher order models: the atomic structures of a material, the inter-atomic interaction, on-site anisotropy and magnetic moment. On the other extreme at relatively large scale (μm to mm) the atomic structure can be ignored and continuous models can be used. There are also models to link the two extremes such as atomistic modelling, which links the quantum physics with the classical interpretation. In ferromagnets, the continuous model was introduced by Brown in 1963, and is know now as micromagnetics. Micromagnetics can describe static properties by energy minimisation techniques, or dynamic behaviour using the Landau-Lifshitz-Gilbert equation. There are limitations, when the continuous assumption is not valid such as when considering interfaces, defects, high temperature. The numerical implementation of micromagnetism (such as OOMMF, magpar, FEMME, mumax, Nmag) has a upper limit both in time and length scale due to computational cost [39–44]. To reach large time scale up to thousand of year and more, Kinetic Monte-Carlo (kMC) techniques can be used. The method requires information about possible states and the energy barrier between the states. For a two state system such as recording media, the kMC is ideal to study long time scale properties and will be the model used in this work. To describe the kMC model, first the Stoner-Wohlfarth model is introduced.

2.1 Stoner-Wohlfarth model

Stoner and Wohlfarth described the behaviour of a mono-domain particle of volume V, and saturation magnetisation M_s,considering just two elements in the energy: applied field and uni-axial anisotropy [45]. The is no temperature, and basically, the magnetic behaviour of the particle is described by energy minimisation.

If we consider the easy axis to be on the Z-direction and the field at an angle θ_0, the magnetic moment orientation will correspond to the minimum energy of that configuration.

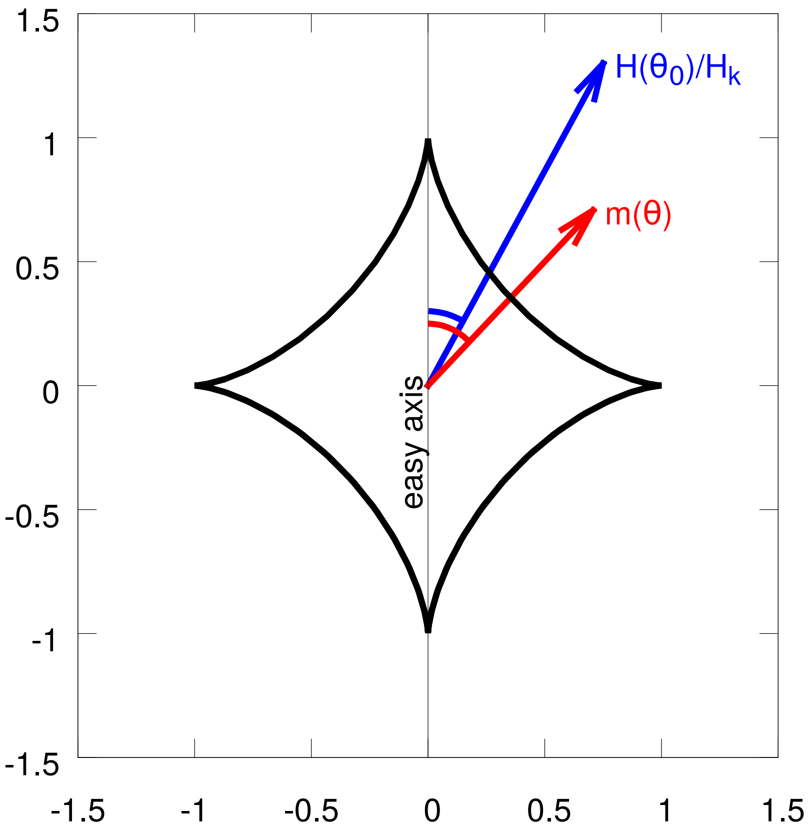

Fig. 2.1 Schematic representation of Stoner-Wohlfarth particle, applied field, magnetisation and easy axis. The black contour corresponds to the Stoner-Wohlfarth astroid. For applied field inside the astroid there two possible orientations of the moment and just one for field outside the astroid.

Mathematically it can be proved that the magnetic moment will be in the plane defined by easy axis and applied field, reducing the problem to a 2D geometry. Therefore we will consider the magnetic moment vector having an angle θ with respect to the easy axis. The energy of the particle is:

$$E = -KV\cos^2\theta - M_s H_{ap} V \cos(\theta_0 - \theta) \tag{2.1}$$

By rearranging the terms, the equation becomes:

$$W = \frac{E}{V} = -\frac{M_s}{2}\left[H_K \cos^2\theta + 2H_{ap}\cos(\theta_0 - \theta)\right] \tag{2.2}$$

where $H_K = \frac{2K}{M_s}$ is the anisotropy field. If the field is zero, there are 2 two possible states with same energy for $\theta = 0$ and π and a maximum at $\theta = \pi/2$. The particle can switch from one state to the other, just when the two energy minima merge or one of them disappears becoming an inflexion points in the energy landscape: both the first and second order derivative of energy needs to cancel out: $\partial W/\partial\theta = \partial^2 W/\partial\theta^2 = 0$. The field at which this happens is called the critical field:

$$H_{cr} = \frac{H_K}{g(\theta_0)} \tag{2.3}$$

$$g(\theta_0) = \left[\sin^{2/3}(\theta_0) + \cos^{2/3}(\theta_0)\right]^{3/2} \tag{2.4}$$

If the modulus of the applied field is larger then the critical field, there is just one state corresponding to an energy minimum, otherwise there are two states separated by an energy barrier.

The hysteresis loop as a function of field orientation with respect to the easy axis is illustrated in figure 2.2a. For the parallel case the loop is rectangular, with the magnetisation remaining saturated until reaching the critical field, which coincides with coercivity. For increasing angle θ_0, the magnetisation changes the orientation to balance the torque from the anisotropy and from the field which now want to align the particle in different directions. The critical field and coercivity coincide for θ_0 between 0 and $\pi/4$. For larger angles, the critical field is symmetric, but the coercivity decreases towards zero. Both the coercivity and remanence can be calculated:

$$H_c(\theta) = \begin{cases} \frac{H_k}{g(\theta)} & \text{if } \theta \in [0, \frac{\pi}{4}] \\ \frac{H_k sin(2\theta)}{2} & \text{if } \theta \in (\frac{\pi}{4}, \frac{\pi}{2}] \end{cases} \tag{2.5}$$

$$M_r(\theta) = \begin{cases} \sqrt{\frac{1+\frac{1}{\sqrt{1+tg(2\theta)^2}}}{2}} & \text{if } \theta \in [0, \frac{\pi}{4}] \\ \sqrt{\frac{1-\frac{1}{\sqrt{1+tg(2\theta)^2}}}{2}} & \text{if } \theta \in (\frac{\pi}{4}, \frac{\pi}{2}] \end{cases} \tag{2.6}$$

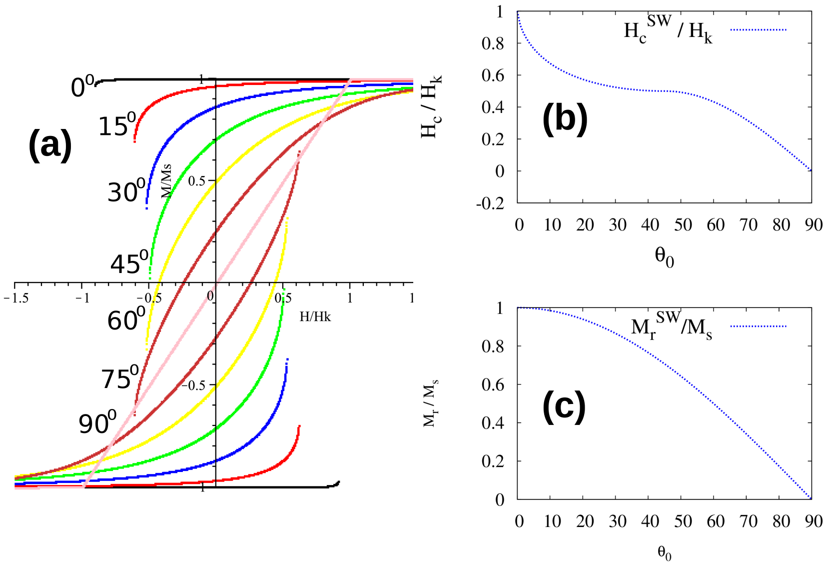

Fig. 2.2 Hysteresis of SW particle for different orientation of applied field with respect to the easy axis (a). Coercivity (b) and remanence (c) as function of the angle between easy axis and applied field.

For the easy axis parallel with the applied field the energy barrier between the states is:

$$\Delta E_1 = KV \left[1 \pm \frac{H_{ap}}{H_K}\right]^2 \tag{2.7}$$

where the "+" and "-" corresponds to the asymmetry between the two energy minimum. For a generic orientation of easy axis the energy barriers are given by Pfeiffer approximation [46]:

$$\Delta E_1(H,\theta_0) = KV\left[1-\frac{H_{ap}}{H_{cr}(\theta_0)}\right]^{0.86+1.14g(\theta_0)} \tag{2.8}$$

$$\Delta E_2(H,\theta_0) = KV\left[1+\frac{H_{ap}}{H_{cr}(\theta_0)}\right]^{0.86+1.14g(\theta_0)} \tag{2.9}$$

Where H_{cr} and $g(\theta_0)$ are given in equations 2.3 and 2.4.

The reduction of coercivity, as function of misalignment of easy axis and field is large. For an angle of 5°and 20°the coercivity is reduced to 0.77 and 0.57 respectively. In recording media the alignment of the easy axis is controlled to be below 5°. This has implication on the energy barrier as given by equations 2.7- 2.9.

2.2 Thermally activated magnetisation reversal

The SW model, describes the equilibrium behaviour neglecting the dynamical process and temperature. First Landau and Lifshitz developed a dynamical approach and later Gilbert derived a modified version which is used nowadays and referred to as LLG (Landau-Lifshitz-Gilbert) equation [47, 48]:

$$\frac{d\vec{M}}{dt} = -\frac{\gamma}{(1+\alpha^2)}\left[]\vec{M}\times\vec{H_{eff}} - \alpha\vec{M}\times\left(\vec{M}\times\vec{H_{eff}}\right)\right] \tag{2.10}$$

where the effective field is the summation of all contributions and can be written as $H_{eff} = \frac{\partial E}{\partial \vec{M}}$. γ is the gyromagnetic ratio and α is the damping constant. The first term is a precession around the effective field and the second is a viscous damping aligning the moment towards the effective field. The dynamical switching is described by a precession around equilibrium, with a damping effect which brings the magnetisation in the minimum energy state. Once the equilibrium is reached the dynamics is stopped. Under the presence of a thermal bath, there are random forces acting on the moment and the process becomes stochastic, requiring statistical description. Also, if the thermal energy is large enough, the particle can change the current state to a different one without the presence of an external field. This is called thermal switching or thermally activated switching. Brown initiated the work, for a SW particle undergoing thermally activated magnetisation switching, using the Fokker-Planck equation [49]. The work led to the conclusion that the dynamical behaviour is characterised by short time scales (around ns) and the long time behaviour can be described by an Arrhenius-Neel escape rate or relaxation time given in eq. 1.11. The attempt frequency f_0, has a complex dependence on the reversal mechanism, particle size, anisotropy type, field, etc. For the moment we will consider f_0 a constant [49].

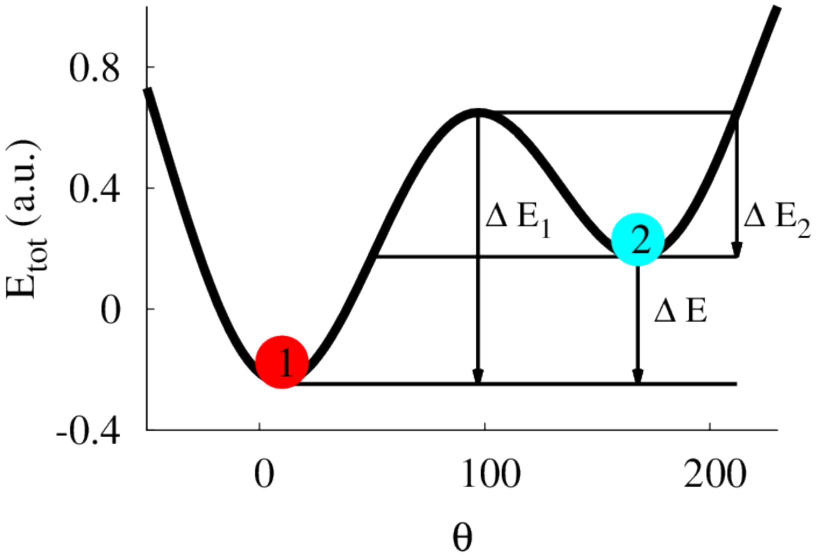

Fig. 2.3 Energy landscape for SW-particle with two mimima.

Using the SW particle and the Arrhenius-Neel relaxation time, the long time scale behaviour can be described as a probability flow from one state to the other. Considering an energy landscape with two energy minima separated by an energy maximum (fig. 2.3) in the presence of thermal bath the particle state is statistically defined as a probability of being in that state (P_1, P_2). Arrhenius-Neel relaxation rate can be seen as a probability flow over the energy barrier from one state to the other [50]. In this formalism, the change in probability of state "1" is given by the difference between the probability flow from state "2" to "1" and probability from from state "1" to "2":

$$\frac{dP_1}{dt} = -w_{12}P_1 + w_{21}P_2 \tag{2.11}$$

$$\frac{dP_2}{dt} = -w_{21}P_2 + w_{12}P_1 \tag{2.12}$$

where w_{12} and 2_{21} are the escape rates from state 1 and 2 respectively. Assuming the initial condition, that $P_1 = 1$ and $P_2 = 0$, the probability of magnetic moment to be in state "2" as function of time is given by [51, 46]:

$$P_2 = \left(1 - e^{-\frac{t}{\tau}}\right)\left(1 + e^{-\frac{\Delta E}{k_B T}}\right)^{-1} \tag{2.13}$$

where

$$\Delta E = \Delta E_1 - \Delta E_2 = E_2 - E_1 \tag{2.14}$$

and

$$\begin{aligned}\tau &= \frac{1}{f_0\left(e^{\frac{-\Delta E_1}{k_B T}} + e^{-\frac{\Delta E_2}{k_B T}}\right)} \\ &= {f_0}^{-1} e^{\frac{\Delta E_2}{k_B T}} \left(\frac{1}{1 + e^{-\frac{\Delta E}{k_B T}}}\right)\end{aligned} \tag{2.15}$$

Equation 2.13 allows to investigate the magnetic behaviour at any time larger then the attempt frequency ($\approx 10^-9s$) time where the LLG dynamics is not important. In recording media the information is written below the ns time region and the LLG dynamics is required to correctly describe the magnetic behaviour. Due to computational cost LLG simulations are limited to 10-100 of ns. The characterisation process based on hysteresis loop, magnetisation decay in time, field cooling are in the order of ms to hours or to years in the case of stability of recording information. This process can not be done with the LLG formalism and methods based on the master equation described above are required. The method used in this thesis is the kinetic Monte-Carlo method (kMC). The method is described in detail for an ensemble of spherical particles in reference [52].

The kMC method, requires as input

1. Material property: anisotropy value, easy axis orientation, saturation magnetisation, distribution properties as appropriate.
2. Geometry of the system: particle, position, shape, volume and distribution of volume as appropriate.
3. Interaction type and expression.
4. External factors such as the time dependence of field for hysteresis loop (field rate) or temperature variation in time.

Based on the above information the kMC method implemented here can simulate, hysteresis loop, reversal curves, minor hysteresis loops, ZFC-FC (zero field cooling-field cooling) and magnetisation relaxation experiments. The kMC method has the following steps:

1. The system is initialised.
2. The time step and the corresponding external factors are considered.
3. A particle "i" is selected.
4. The effective field acting on particle "i" is calculated as summation of applied field and the interaction field.
5. The magnetic moment orientation corresponding to the two or one minima is calculated using the SW particle energy landscape.
6. If there is just one minimum the magnetic moment will automatic updated to the corresponding state and the process continue with step 11.
7. The energy barrier is calculated using eq. 2.8, 2.9.
8. The probability of particle switching to the new state is calculated based on equation 2.13.
9. A random number between 0 and 1 is generated;
10. If the random number is smaller than the probability at 8 then the particle switches to the new state, else it remains in the previous state.
11. A new particle is selected and the steps 3-10 are repeated for all particles.
12. The time is adjusted and the steps 2-12 for all time steps.

Before presenting the details of the kMC model for recording media, a discussion about the use of a constant attempt frequency ,f_0, is required. Brown derived f_0 as:

$$f_0 = \frac{\alpha\gamma}{1+\alpha^2}\sqrt{\frac{H_K^3 M_s V}{2\pi k_b T}}\left(1-\frac{H}{H_K}\right)\left(1-(\frac{H}{H_K})^2\right) \tag{2.16}$$

Breth and co-workers [53] study the importance of the above expression as function of field rate, showing that the exact expression is crucial at large field rates ($10^8 - 10^9$ Oe/s), but not important for smaller field rates such as those experimentally accessible via VSM (Vibrating Sample Magnetometer) SQUID (Superconducting Quantum Interference Device) or MOKE

(Magneto Optic Kerr Effect) (field rate <10^5 Oe/s). The results are experimentally confirmed using the SQUID device by measuring hysteresis loops and transition probability in different fields and temperatures [54]. The work done in this thesis are below the limits where the details of eq. 2.16 are important and for this reason a constant value of $f_0 = 10^9 s^{-1}$ is used.

2.3 Kinetic Monte-Carlo model of recording media

To model the magnetic properties of recording media, just the recording layer is considered as a system of mono-domain particles with uni-axial anisotropy. In literature the grains geometry is descried using a Voronoi tessellation [31, 55–59]. In figure 2.4a there is an example of PMR media from TEM image (top view) [9] and the Voronoi structure to reproduce the experimental geometry in figure 2.4. Here the structure is generated using voro++ software package [60, 61] considering periodic boundary conditions. This package computes the grains position and geometry The structure is modified to include intergranular spacing. This is done by shrinking the grains towards the centre of each grain with a certain amount. The grain to spacing area is quantified by the packing density: $pkdst = (total\ grain\ area)/(system\ area)$. The interaction will be strongly dependent on grain geometry, but this aspect will be discussed at the end of the section.

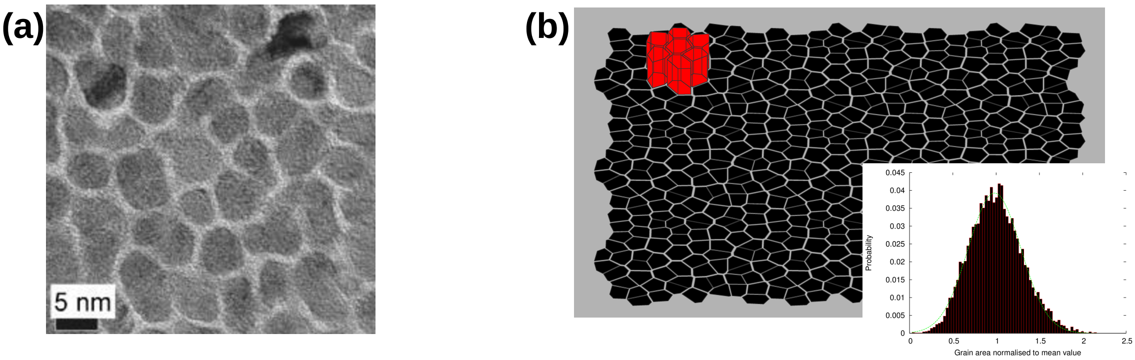

Fig. 2.4 Example of granular structure from TEM imaging (a) [9] and simulated structure using voronoi construction (b). The grain size distribution is in the inset.

The anisotropy value will be described by a Gaussian or Log-normal distribution:

$$G(A,\sigma_A,\mu_A) = \frac{1}{\sqrt{2\pi\sigma_A^2}} exp\left[\frac{(x-\mu_A)^2}{2\sigma_A^2}\right] \tag{2.17}$$

$$L(A,\sigma_A,\mu_A) = \frac{1}{A}\frac{1}{\sqrt{2\pi\sigma_A^2}} exp\left[\frac{(ln(x)-\mu_A)^2}{2\sigma_A^2}\right] \tag{2.18}$$

where μ_A is the mean of the distribution and σ_A is the standard deviation of the distribution. In a random system of particles the easy axis will follow a spherical random distribution given by:

$$dP = \sin(\psi)d\psi d\varphi \quad \text{for} \quad \psi \in [0,\pi] \text{ and } \varphi \in [0,2\pi] \tag{2.19}$$

where θ and ϕ are the angles corresponding to the spherical coordinate system and θ is the angle between the Z direction and easy axis.

For PMR the easy axis orientation has a important role as discussed in previous section and a narrow distribution around the perpendicular direction to the thin film is required. In the model the easy axis will follow a Gaussian distribution of angle ψ with respect to the Z-direction with average value of 0 and a dispersion of σ_ψ. The description so far allows to describe a non-interacting granular recording media. Close to 0K ($KV/k_bT \to \infty$) this version of the model reproduces all the features from the SW theory or derived from SW theory. In presence of thermal effects (finite value of KV/k_bT), the coercivity depends on the applied field sweep rate (R). The coercivity field as function of the sweep rate of the applied field. This was first found empirically by Sharrock [62] and derived theoretically by Chantrell [63] under the assumption of constant attempt frequency and easy axis parallel with the external field:

$$H_C = H_K\left(1-\sqrt{\frac{ln(tf_o)}{\beta}}\right) \tag{2.20}$$

where

$$t = R^{-1}\frac{H_K}{2\beta}(1-\frac{H_C}{H_K})^{-1} \tag{2.21}$$

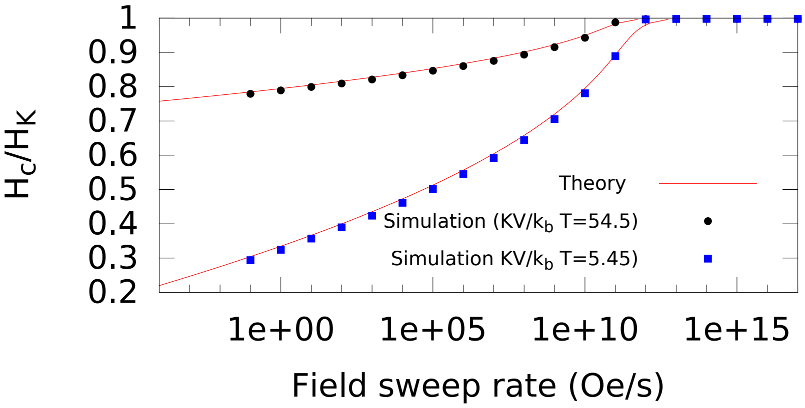

Fig. 2.5 Coercivity as function of applied field sweep rate for the easy axis aligned with the field for two thermal stability factors: KV/k_bT =54.5 (black circle) and 5.45 (blue square). The simulation results agree very well with the theoretical prediction (red line).

$$R = \frac{\Delta H}{\Delta t} \tag{2.22}$$

and

$$\beta = \frac{KV}{k_bT}$$

Equation 2.20 is valid for $ln(tf_0) < \beta$. β is a measure of the thermal stability and depends on the ratio between the anisotropy energy (KV) and thermal energy (k_bT).

In figure 2.5, the simulation results are in good agreement with theoretical prediction based on eq. 2.20. At high sweep rate the system is not influenced by temperature. As the sweep rate decreases the role of temperature is important, with lower thermal stability factor KV/k_bT leading to a larger reduction in coercivity.

The nature of intergranular exchange interaction is not well understood and there is not a well defined inter-granular exchange. Here the exchange is defined based on the work done by Peng et al. [64]. The exchange interaction between grain i and j can be written as a product between the average exchange interaction at saturation (H_{exch}) and the distribution functions [64]:

$$H_{ex}^{ij} = H_{exch}\left(\frac{J_{ij}}{<J>}\right)\left(\frac{L_{ij}}{<L>}\right)\left(\frac{<A>}{A_i}\right) \tag{2.23}$$

Where J is the exchange constant. L is the length of the common grain boundary. A is the area of the grain. "$< O >$", refers to average value of the property "O". The distribution of exchange is given by a distribution of exchange coupling J and grain geometry (L and A). Due to the nature of exchange interaction, just the nearest neighbours are considered. The other important interaction, the magnetostatic interactions, is long range. For computational efficiency reason the magnetostatic field can be written as multiplication between a W matrix and one dimension matrix containing the magnetic moment:

$$H_{i,j}^{\beta} = W_{i,j}^{\alpha\beta} M_{i,\alpha} \tag{2.24}$$

β and α are the Cartesian coordinate x,y and z. $W_{i,j}$ is a 3 by 3 matrix depending only on the geometry of grain i and j. The simplest approach to compute the W matrix is the dipole approximation.

Quantity	Symbol	Value	Units
Anisotropy value	K	7×10^6	erg/cm^3
Saturation magnetisation	M_s	700	emu/cm^3
Grain size	D	8.5	nm
Grain height	h	10	nm
packing density	pkdst	0.8	
Log-normal distribution of K	σ_K	0.05	
Gaussian distribution of easy axis around Z direction	σ_ψ	3.0	
Number of grains	N	10000	
External field sweep rate	R	10	kOe/s
Anisotropy field	H_K	20	kOe
Coercivity field at 300K	H_c	10.4	kOe
Average magnetostatic field at saturation	H_{mag}	4.6	kOe
Average exchange field at saturation	H_{exch}	$\in [0-6]$	kOe

Table 2.1 List of parameters for the granular media model [65].

The results presented in this thesis on granular media are done for the parameters given in table 2.1, unless is otherwise specified. The magnetic grains are obtain by Voronoi tessellation with an average diameter of 8.5nm and 10nm height. The anisotropy field is 20kOe, with a coercivity of 10.4kOe corresponding to room temperature (300K) hysteresis experiments at 10kOe/s external field sweep rate. The average magnetostatic field is approximately half of the coercivity and depends on the grains aspect ratio and shape. The value given in the table 2.1 is based on exact calculation on the magnetostatic interaction for this system (chapter 3). In chapters 5, 6 and 4 the magnetostatic interaction is varied between 0 and 4.6kOe, corresponding to lower packing fraction. Numerically this is done by maintaining the the grain shape, size and relative orientation of the grain and increase just the inter-granular spacing by a constant factor.

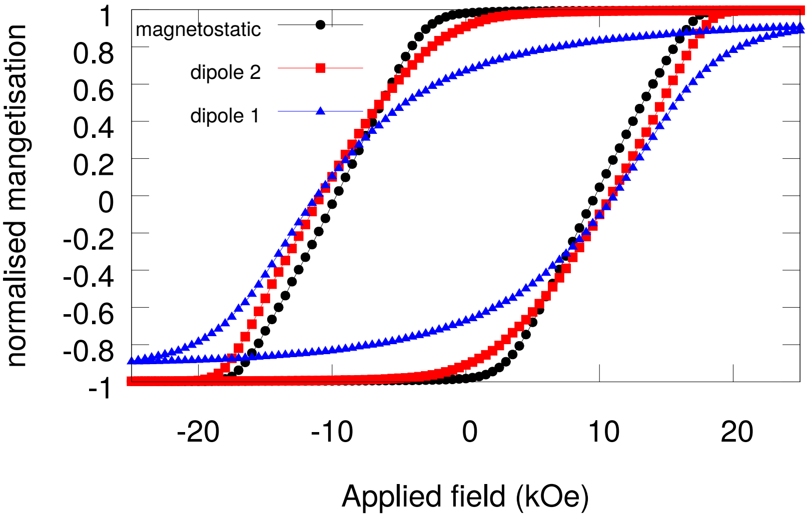

Fig. 2.6 Example of hysteresis loop generated using magnetostatic interaction based on grain shape (black circle) and using dipole approximation. The dipole approximation is strongly dependent on the grain coordinates as a single point. Here two examples are shown where the grain position is given by the Voronoi points to generate the grains (blue triangle) and secondly when the grain position is the geometric centre of the grain (red square).

For granular media, as the one considered here, the dipole approximation is incorrect for nearest neighbours as it does not take into account the grain geometry (shape and aspect ratio). The errors are strongly dependent on how the centre of the dipoles (in this case grain) are defined. One possible definition is based on seed points of the voronoi tessellation. The seed points for the voronoi structure are defined so that each two neighbour grains have the segment connecting the seed points perpendicular to the common grain boundary. A second possibility is considering the geometric centre of the grain, which is the average value the grain corners. In figure 2.6 a hysteresis loop is generated using both consideration and also with the correct magnetostatic field (labelled as magnetostatic). It can be seen that the dipole approximation leads to a smaller remanence, and overall with the incorrect behaviour of the granular system. In the next chapter we will present different approaches to calculate the correct magnetostatic field for a granular system.

2.4 Conclusion

In this chapter a model of PMR media was introduced based on the kMC model. The first part describe the single-domain particle properties at 0K using the Stoner-Wohlfarth model. The magnetic moment switching without an external field due to thermally activate magnetisation reversal is discussed. At time scales larger than ns, the full dynamics of the magnetic moment can be replaced by quasi-static process, in which the magnetic moment of the particle is described by the energy minima and the transition between the energy minima. The model is tested by reproducing the coercivity dependence of the external field sweep rate as derived by Chantrell [63].

Exchange and magnetostatic interaction are described. For granular system as the one considered here for PMR, the dipole approximation is inaccurate. Alternative approach to compute the correct magnetostatic interaction are presented in chapter 3.

Chapter 3

Magnetostatic interaction

Magnetostatic interactions have an important role in the behaviour of magnetic systems. If exchange interaction forms large domains, magnetostatic interaction favours the formation of narrow domains via the closed flux configuration.

In contrast to the exchange interaction which is short range (has contribution only from the neighbouring environment), the magnetostatic interaction is a long range interaction from the entire system. For strongly coupled magnetic nano-structures, the accuracy of the interaction field is important for the domain formation and grain-grain correlation. In this chapter, different methods for computing the magnetostatic interaction are considered: mean-field, dipole approximation and surface charges(surface integrals). In the first part, the main equations and concepts are introduced. Then the naive implementation of surface charges (5-fold integral) is tested for a generic system. Afterwards a more sophisticated approach (4-fold integral) is considered for the particular case of 2D granular system.

3.1 Introduction

The magnetostatic field can be calculated using Maxwell's equations assuming no electric current is present in the sample:

$$\nabla \cdot \vec{B} = 0 \tag{3.1}$$

$$\nabla \times \vec{H} = 0 \tag{3.2}$$

The magnetostatic field can be express in terms of an scalar potential, U:

$$\vec{H} = \nabla U \tag{3.3}$$

with U calculated at a position vector, $\vec{r}$, as follows:

$$U(\vec{r}) = \frac{1}{4\pi}\left(-\int_{V'}\frac{\nabla M(\vec{r'})}{|\vec{r}-\vec{r'}|}dV' + \int_{S'}\frac{\vec{n}\cdot\vec{M}(\vec{r'})}{|\vec{r}-\vec{r'}|}dS'\right) \tag{3.4}$$

The first integral is on the volume of the magnetic sample, and the second one is on the surface or surfaces of the magnetic bodies/entities. Equation 3.4 can be described as the sum of two potentials: one of a volumetric charge distribution, with the density, $\rho_m = -\nabla M$, and the second as a surface charge distribution, $\sigma_m = \vec{n}\cdot\vec{M}$. Although, in reality, for a magnetic system these charges do not exist, the mathematical description is similar to the one in electrostatics. The main difference is that for a magnetic body, the surface over which the integral is performed needs to enclose a volume, where as for charges (electrostatics) this is not the case. From equations 3.3 and 3.4, the magnetostatic field can be calculated as:

$$H(\vec{r}) = \frac{1}{4\pi}\left(-\int_{V'}\rho_m(\vec{r'})\frac{\vec{r}-\vec{r'}}{|\vec{r}-\vec{r'}|^3}dV' + \int_{S'}\sigma_m(\vec{r'})\frac{\vec{r}-\vec{r'}}{|\vec{r}-\vec{r'}|^3}dS'\right) \tag{3.5}$$

The above equation can be analytically solved just in some particular cases and also it is computationally expensive for direct numerical calculation. Therefore, there are different levels of approximations. The simplest approximations, which are discussed next, are mean field of uniform magnetised body and dipole interaction approximation. The latter can be extended for specific cases to multi-pole approximation, depending on the symmetry in the system. In micro-magnetic simulation based on finite difference method (OOMMF, LLG Micromagnetics Simulator, Micromagus, Mumax, Micromagnum), the system is divided into a regular array of cubes. In this case the demagnetisation tensor can be calculated analytically based on the work by Newell [66].

3.2 Mean field approximation for uniform magnetised sample

Mean field is a basic approximation for the magnetostatic interaction, assuming a magnetostatic field proportional with the mean magnetisation of the system:

$$\vec{H}_{meanfield} = N_d < \vec{m} > \tag{3.6}$$

where N_d is the demagnetisation tensor, with the generic form:

$$N_d = \begin{bmatrix} N_d^{xx} & N_d^{xy} & N_d^{xz} \\ N_d^{yx} & N_d^{yy} & N_d^{yz} \\ N_d^{zx} & N_d^{zy} & N_d^{zz} \end{bmatrix} \tag{3.7}$$

The elements of the tensor depend on the geometric shape of the magnetic sample and can be non-uniform inside the sample. For an ellipsoid of revolution the demagnetization field is uniform inside the sample, the analytical equations being derived by Osborn. Considering an ellipsoid of revolution with two semi-axis equal to a and the third semi-axis with c, the off diagonal terms of the N_d tensor become 0. The variation of the N_d with the aspect ratio c/a is shown in figure 3.1. For the semi-axis c in the Z direction of a Cartesian system, and

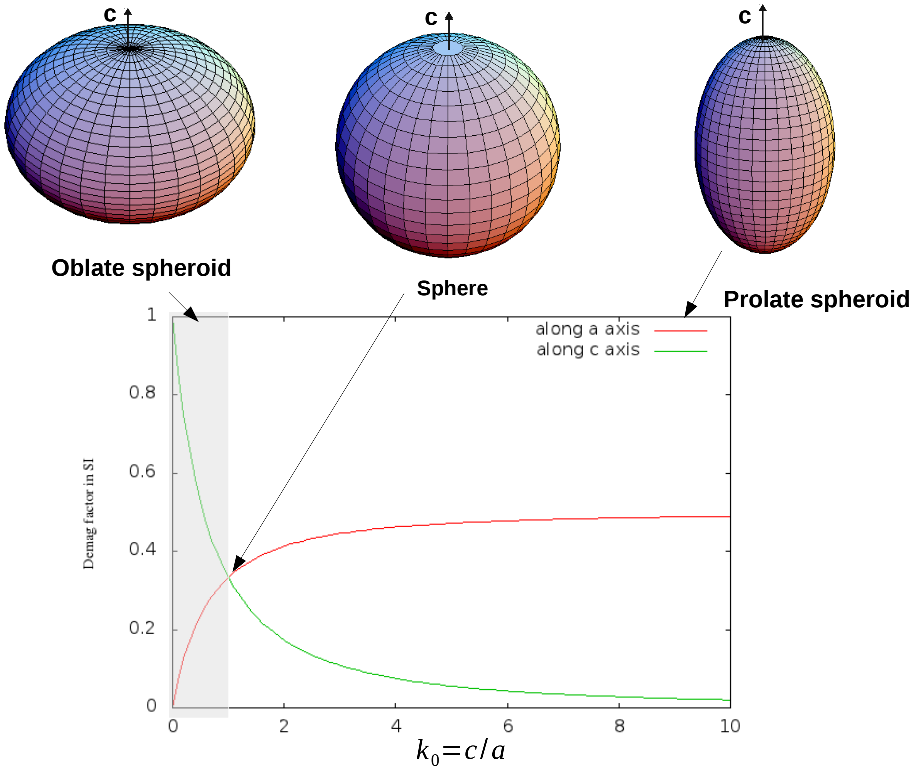

Fig. 3.1 Demagnetisation tensor as function of aspect ratio for ellipsoid of revolution. Semi-axis c corresponding to the polar direction as illustrated.

aspect ratio, $k_0 = \frac{c}{a}$ the N_d^{zz} component can be calculated from the following equations:

$$N_d^{zz} = \frac{4\pi}{1-k_0^2}\left[1 - \frac{k_0}{\sqrt{1-k_0^2}} arccos(k_0)\right] \qquad \text{for } k_0 < 1 \tag{3.8}$$

$$N_d^{zz} = \frac{4\pi}{3} = N_x = N_y \qquad \text{for } k_0 = 1 \tag{3.9}$$

$$N_d^{zz} = \frac{4\pi}{k_0^2 - 1}\left[\frac{k_0}{\sqrt{k_0^2-1}} arcosh(k_0) - 1\right] \qquad \text{for } k_0 > 1 \tag{3.10}$$

The other two demagnetisation factors ($N_d^{xx} = N_d^{yy}$) can be calculated using the fact that $N_d^{xx} + N_d^{yy} + N_d^{zz} = 4\pi$ in CGS units (1 in SI).

The approach can be applied approximately when the magnetisation is uniform as in diluted magnetic nanoparticles systems (low packing fraction) for weak magnetostatic strength. Also it is used in the following chapters for the determination of the SFD.

As the packing fraction increases, the magnetostatic field from neighbours grains start to dominate and will lead to correlated behaviour such as magnetic cluster formation. This can not be described in the mean field approach and equation 3.5 must be used.

3.3 Dipole interaction approximation

The widely used approach for calculating the magnetostatic field is based on the dipole approximation, where each spin or macro-spin is approximated with a magnetic dipole. The origin of this can be seen if we consider a uniform magnetised cuboid and the field created at a point P, corresponding to a vector $\vec{r}$. In this case, the first term of equation 3.5 is zero. We can consider the magnetisation along the Z direction and the cuboid in centre of the Cartesian coordinate system, therefore just the top and bottom surfaces contribute to the magnetic field. This is similar to the electrostatic case with two surface with opposite polarisation separated by a distance h. For simplicity we consider the top and bottom surfaces much smaller than the distance from the cuboid to the point P. In this case the integral becomes:

$$H(\vec{r}) = \frac{1}{4\pi}\sigma_m S_{top}\frac{\vec{r} - h/2\vec{e}_z}{|\vec{r} - h/2\vec{e}_z|^3} - \frac{1}{4\pi}\sigma_m S_{bottom}\frac{\vec{r} + h/2\vec{e}_z}{|\vec{r} + h/2\vec{e}_z|^3} \tag{3.11}$$

$$H(\vec{r}) = \frac{1}{4\pi}\sigma_m S_{top}\left(\frac{\vec{r} - h/2\vec{e}_z}{|\vec{r} - h/2\vec{e}_z|^3} - \frac{\vec{r} + h/2\vec{e}_z}{|\vec{r} + h/2\vec{e}_z|^3}\right) \tag{3.12}$$

where $+h/2$ and $-h/2$ corresponds to the position of the top and bottom surface with respect to the Z-direction and $\vec{e}_z$ is the versor of the Z-direction. We can write $|(\vec{r} \pm h/2\vec{e}_z)|$ as:

$$|(\vec{r} \pm h/2\vec{e}_z)| = \sqrt{r^2 \pm r_z h + (h/2)^2} \tag{3.13}$$

$$|(\vec{r} \pm h/2\vec{e}_z)| = \frac{1}{r}\sqrt{1 \pm \frac{r_z h}{r^2} + (\frac{h}{2r})^2} \tag{3.14}$$

$$\tag{3.15}$$

Then we can write as a series expansion:

$$\left(1 \pm \frac{r_z h}{r^2} + 1/4\frac{h^2}{r^2}\right)^{-3/2} = 1 \pm 3/2\frac{r_z h}{r^2} + \left(-3/8\, r^{-2} + \frac{15\, r_z{}^2}{8\, r^4}\right) h^2 \pm \left(\frac{15\, r_z}{16\, r^4} - \frac{35\, r_z{}^3}{16\, r^6}\right) h^3 + O\left(h^4\right) \tag{3.16}$$

This is the expression for multi-pole expansion in electrostatics, where the first term is from the monopole, the second from the dipole, and higher order terms. In magnetostatics the monopole contribution cancels and just dipole and the higher order terms remain. Using the fact that $\sigma_m * S_{top} h$ is $M_s V$ and substituting equation 3.16 in 3.12 we obtain the following terms:

$$H_z(r) = \frac{MsV}{4\pi r^3}\left[\left(3\frac{r_z{}^2}{r^2} - 1\right) + \left(\frac{3}{8} - \frac{15\, r_z{}^2}{4\, r^2} + \frac{35\, r_z{}^4}{8\, r^4}\right)\left(\frac{h}{r}\right)^2 + O\left(h^4\right)\right] \tag{3.17}$$

$$H_x(r) = \frac{MsV}{4\pi r^3}\left[3\frac{r_x r_z}{r^2} + \frac{r_x r_z}{r^2}\left(-\frac{15}{8} + \frac{35}{8}\frac{r_z^2}{r^2}\right)\left(\frac{h}{r}\right)^2 + O\left(h^4\right)\right] \tag{3.18}$$

The $H_y(r)$ component can be obtained from the $H_x(r)$ replacing the subscript 'x' with 'y' in the entire equation. It can be observed that the expansion contains just even powers of h/r. The first term in the above equation corresponds to the known dipole field expression when the dipole moment points in the Z direction. For the general case the dipole field is given by:

$$\vec{H}_{dipole}(\vec{r}) = \frac{M_s V}{4\pi r^3}\left[\frac{3}{r^2}(\vec{m} \cdot \vec{r})\vec{r} - \vec{m}\right] \tag{3.19}$$

The equation 3.19 can be written using the tensor formulation:

$$\vec{H} = W_{dip} m \tag{3.20}$$

with

$$W_{dip} = \frac{V}{4\pi r^3} \begin{bmatrix} \frac{3r_x^2}{r^2} - 1 & \frac{3r_x r_y}{r^2} & \frac{3r_x r_z}{r^2} \\ \frac{3r_y r_x}{r^2} & \frac{3r_y^2}{r^2} - 1 & \frac{3r_x r_z}{r^2} \\ \frac{3r_z r_x}{r^2} & \frac{3r_z r_y}{r^2} & \frac{3r_z^2}{r^2} - 1 \end{bmatrix} \qquad (3.21)$$

$$m = \begin{bmatrix} m_x \\ m_y \\ m_z \end{bmatrix} \qquad (3.22)$$

Equation 3.17 and 3.18 show that the behaviour is dominated by the ratio of r_x,r_y,r_z and h to r. For example the Z component of the field can be described using r_z/r and h/r. In figure 3.2 is illustrated the dipole approximation in comparison with the exact solution and higher order term in the expansion of equation 3.17. The corresponding errors are shown in figure 3.3. The dipole approximation can over or under estimate depending on the r_z/r ratio. At h/r=1 the error is up to 40% (figure 3.3)and decreases as h/r ratio decreases. If the 2nd order approximation is used the error decreases by a factor of 2 at h/r=1, and by a factor of 10 for the 4th order approximation.

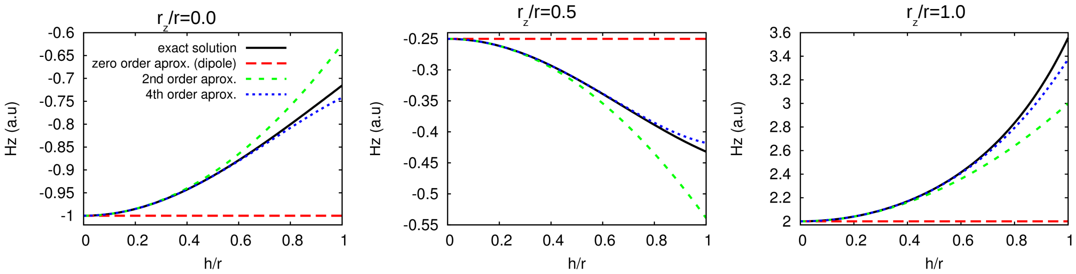

Fig. 3.2 The Z component of the magnetostatic field at a point P, from the expansion as function of dipole separation normalized to the distance to point P. The exact solution is given by eq. 3.12.

3.4 Surface charges integration method

The dipole expression 3.19 gives the correct field created by a uniformly magnetised sphere. For any other shape the expression is the first order approximation in an expansion series of the form of equations 3.17, 3.18. Next we will consider the case of granular recording media,

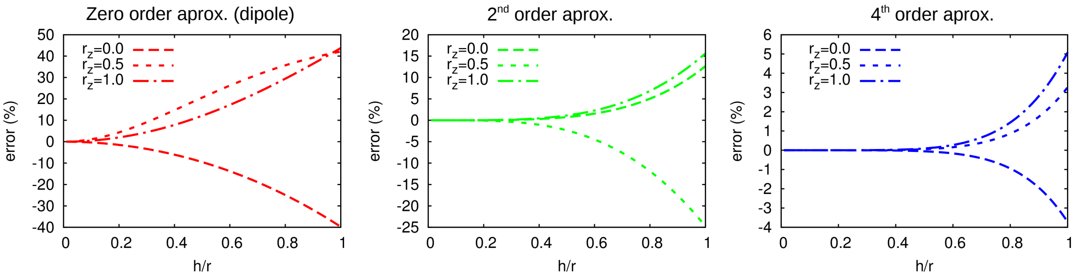

Fig. 3.3 The errors in truncating the expansion to zero order approximation (dipole), 2nd order approximation and 4th order approximation. The exact solution is given by eq. 3.12.

although the conclusion can be extended to any system of non-spherical magnetic structure with uniform magnetisation. The grain that produces the field will be labelled 'source' grain and the grain on which the field acting the 'field' grain (fig. 3.4). For the magnetostatic field of two coupled magnetic grains we need to consider the shape of the 'source' and 'field' grains. The magnetostatic field inside the field grain is non-uniform. For this reason in the literature it is established that a good description of the field acting on the grain is the average

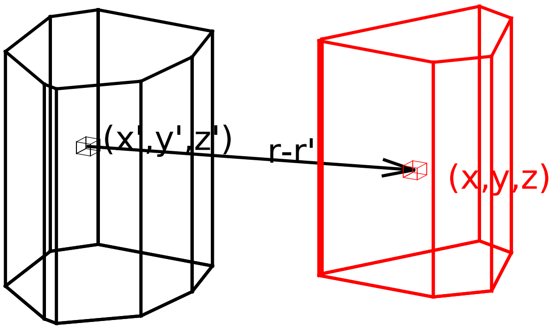

Fig. 3.4 3D geometry for magnetostatic calculation. The field at a point (x,y,z) inside a magnetic grain (field grain) created by a second magnetic grain (source grain) at (x',y',z').

value over the grain volume. Under the above consideration the equation 3.5 becomes:

$$H(\vec{r}) = \frac{1}{4\pi}\left(\frac{1}{V_f}\int_{V_f}\int_{S_s}\sigma_m(\vec{r}_s)\frac{\vec{r}_f-\vec{r}_s}{|\vec{r}_f-\vec{r}_s|^3}dS_s dV_f\right) \tag{3.23}$$

$$H^\alpha = W^{\alpha\beta}M_\beta \quad with \quad \alpha,\beta = x,y,z \tag{3.24}$$

$$W^{\alpha\beta} = \frac{1}{4\pi}\left(\frac{1}{V_f}\int_{V_f}\int_{S_s} n^\beta(\vec{r}_s)\frac{r_f^\alpha - r_s^\alpha}{|\vec{r}_f-\vec{r}_s|^3}dS_s dV_f\right) \tag{3.25}$$

The last equation is the generic magnetostatic tensor expression of the tensor used for the dipole approximation (equation 3.21) and has two important properties:

- $W^{\alpha\beta} = W^{\beta\alpha}$, with α,β=x, y, z. The W matrix is symmetric.
- Tr(W)=1 or 0. The sum of the main diagonal, called trace ($Tr(W) = W^{xx} + W^{yy} + W^{zz}$), is 1 or 0. If the volume of source and field grains coincide then the trace is 1, this corresponds to the self demagnetisation term or shape anisotropy. If the two grains do not overlap then the trace is 0.

The numerical implementation consists in the discretisation of the surface of the source grain and the volume of the field grain in ix,iy,iz elements on X, Y and Z direction. The integral in equation 3.25 is computed by summation over all discretisations. This is the naive approach, but nevertheless a useful tool for arbitrary shapes. An improved approach is derived in the optimisation section, which is specifically constructed for two dimensional granular structures.

The accuracy of the methods will depend on the relative position of the two grains and the grain shape. If the two grains are far away, the result will converge to the point dipole case (eq. 3.21. The other extreme is when the source and the field grain coincide (the self-demagnetisation tensor). This is the case where the shape of the grain will have the largest influence. To test the accuracy of the methods we will consider cuboid shape. First the self-demagnetisation tensor is investigated and compared with the existing literature[67]. Then the inter-granular magnetostatic tensor is tested in comparison with the analytical solution [66].

3.4.1 Cuboid shape

For cuboid shape, due to symmetry, the self-demagnetisation tensor (W) is non-zero just on the first diagonal. Considering a cuboid of dimension $2a$, $2b$, and $2c$ in x,y and z direction, then the z component of the self-demagnetisation tensor is [67]:

$$\begin{aligned} W_{zz}(a,b,c) = & \frac{1}{\pi}\frac{b^2-c^2}{2bc} ln(\frac{l_{abc}-a}{l_{abc}+a}) + \frac{a^2-c^2}{2ac} ln(\frac{l_{abc}-b}{l_{abc}+b}) + \frac{b}{2c} ln(\frac{l_{ab}+a}{l_{ab}-a}) + \\ & \frac{a}{2c} ln(\frac{l_{ab}+b}{l_{ab}-b}) + \frac{c}{2a} ln(\frac{l_{bc}-b}{l_{bc}+b}) + \frac{c}{2b} ln(\frac{l_{ac}-a}{l_{ac}+c}) + 2arctan(\frac{ab}{cl_{abc}}) + \\ & \frac{a^3+b^3-2c^3}{3abc} + \frac{l_{ab}^2-2c^2}{3abc} l_{abc} + \frac{c}{ab}(l_{ac}+l_{bc}) - \frac{l_{ab}^3+l_{bc}^3+l_{ca}^3}{3abc} \end{aligned} \tag{3.26}$$

where $l_{abc} = \sqrt{a^2+b^2+c^2}$ and $l_{ab} = \sqrt{a^2+b^2}$. The x and y components are obtained from permutation in the W_{zz} as following: $W_{xx} = W_{zz}(c,a,b)$ and $W_{xx} = W_{zz}(b,c,a)$.

First we consider the role of discretisation of the two grains. The natural way will be in cubes of equal size, which corresponds to equal discretisation ix=iy=iz for $a = b = c$. For an arbitrary shape this will be more complicated to consider, so it is important to study the role of non-uniform discretisation. For simplicity $a = b$ and ix=iy is considered and both the aspect ratio c/a and iz are systematically varied (figure 3.5). The error is expressed as percentage of the analytical solution: $error(A) = 100(numerical(A)/analytical(A) - 1)$. In figure 3.5, the errors of $W_{xx} = W_{yy}$, W_{zz} and the trace of W is illustrated for 3 aspect ratio c/a=0.5 (top),1 (centre) and 2(bottom). For all aspect ratios, with increasing iz, the accuracy of the W_{xx} component is improved, while the accuracy of the W_{zz} component is decreased. This suggests that there is a trade-off of the accuracy between the two components, which can be determined using the trace of the W tensor (right panel in figure 3.5). The trace gives an indication of the balance between the discretisation and the accuracy of the W tensor. For aspect ratio c/a=1, the equal discretisation (ix=iy=iz) produces the minimum error in all components and has the lowest error in the trace of W. For elongated cuboids (c/a=2) the ideal case is for iz slightly larger than twice ix. For c/a=0.5, the error in W_{xx} is small even for ix=iy=10, but for W_{zz} is much larger leading to a increase of error in the trace for increasing iz. Nevertheless increasing the discretisation in all 3 direction leads to a lower error. Furthermore the results suggest that the trace of the W tensor can be used as a measure of errors in the calculations. This is important for grains with an arbitrary shape, such as those generated using the Voronoi tessellation, where there are no analytical expressions to validate the results. In this case the trace will be used as a measure of errors.

For all the following results, the discretisation is based on uniform cubes. To investigate the errors as a function of aspect ratio, a discretisation of ix=iy=50 is considered, with iz varying with the aspect ratio c/a from 5 for c/a=0.1 and 150 for c/a=3.0. The demagnetisation values are given in figure 3.6. The numerical results are compared with the analytical prediction from cuboid shape (3.26) and from the ellipsoid with the same aspect ratio (eq.

3.8-3.10). Ellipsoids, cuboids or cylindrical shapes are generally used to approximate more complex structures such as the Voronoi grains generated in this work, due to the fact that the demagnetisation factor can be determined analytically. Nevertheless it is important to show that the shapes have a critical role in the magnetostatic interaction. To illustrate this, here we use the cuboid and ellipsoid shape as an example. There is a significant difference between the demagnetisation value of cuboid and ellipsoid shapes. First the W tensor is not uniform in a cuboid shape, whereas for ellipsoids it is uniform with the exact value given by Osborn (eq. 3.8-3.10) [68]. Secondly, the value for cuboid shape and ellipsoid coincide just for the symmetric case a=b=c. In real system, both shapes are an approximation, leading to a inaccurate approximation of the shape effects [67]. The expressions can be used for test of numerical method or approximation. For the naive implementation discussed in this chapter, the errors from the numerical results, are large at small c/a ratio and decrease with

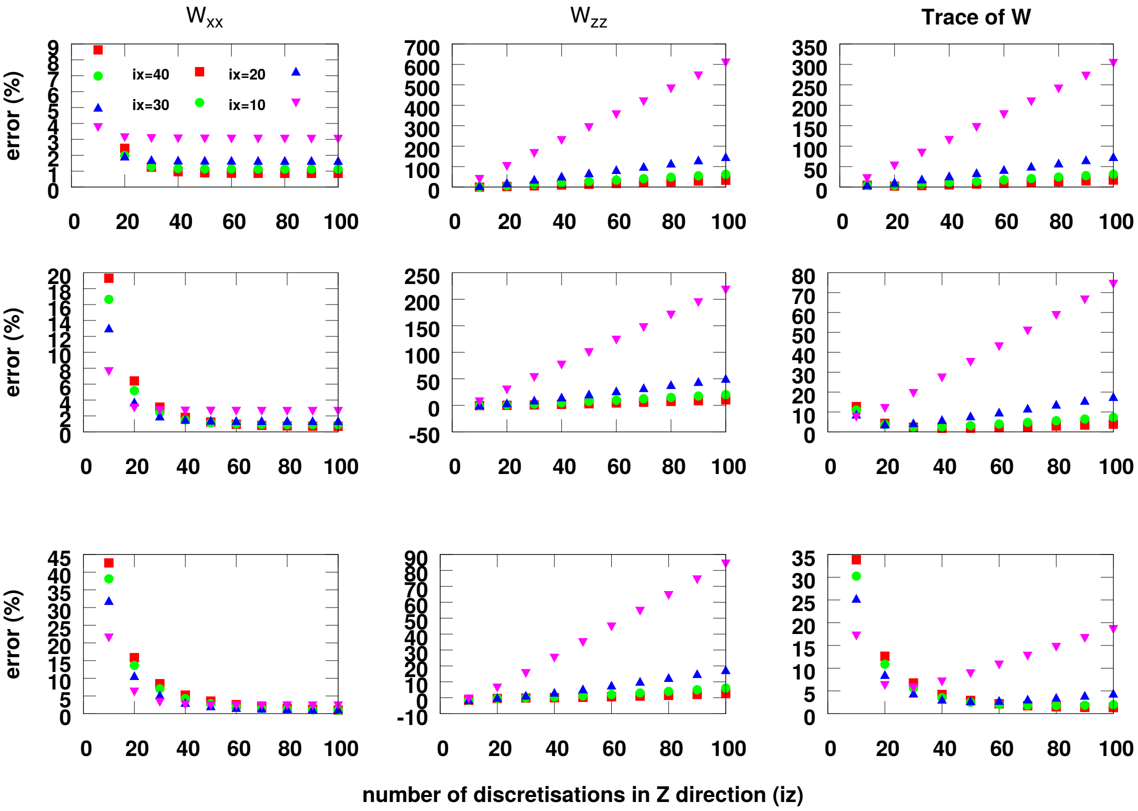

Fig. 3.5 The errors of the numerical method for computing the $W_{xx} = W_{yy}$ (left graph), W_{zz} (centre graphs) and the trace of W (right graph) as function of discretisation in the Z direction (iz). The results are for aspect ratio of c/a=0.5 (top), 1.0 (centre), 2.0 (bottom) and aspect ratio of b/a=1. The discretisation in XY plane (ix=iy) is :10, 20, 30 and 40.

increasing c/a value. The larger error is for c/a=1, approximately 6%, with the mention that all component of the W tensor and the trace have similar errors. The self demagnetisation tensor, being at 0 distance between the source and field grain will produce the largest errors. Therefore, for two different grains, the error of the numerical method is expected to decrease with the distance between grains.

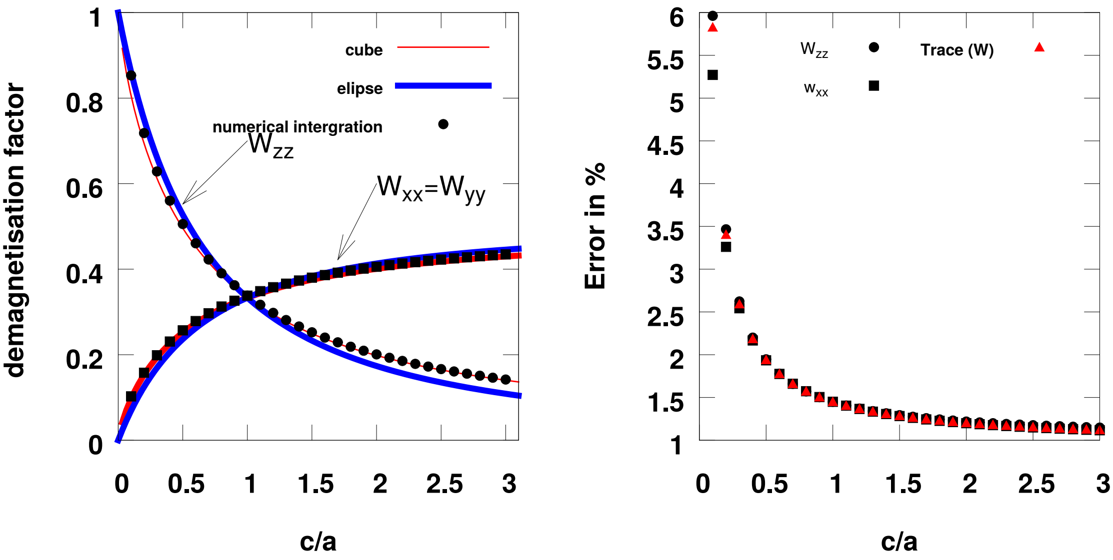

Fig. 3.6 Left:Demagnetisation factor as function of aspect ratio c/a for cuboid shape from numerical calculation (dots) and analytical (red line). Blue line corresponds to the demagnetisation factor for ellipsoid with the same aspect ratio. Right: The error in determination the W tensor component and trace.

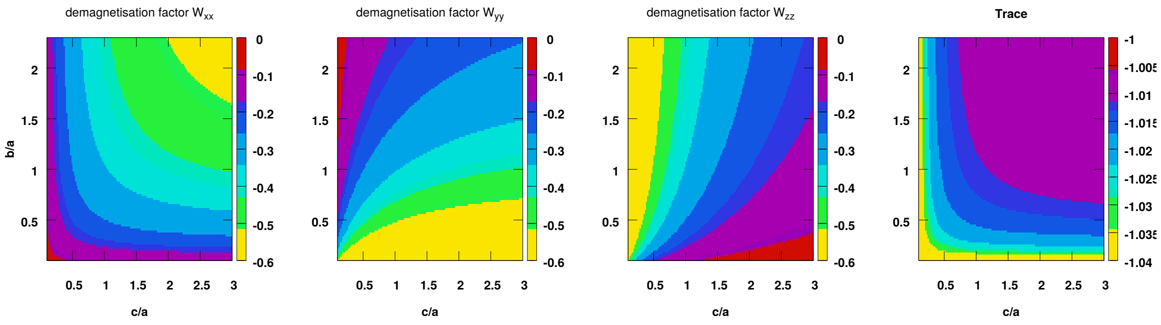

Fig. 3.7 Self-demagnetisation factor, W_{xx}, W_{yy}, W_{zz} and the trace of W, as function of aspect ratio c/a and b/a for cuboid shape.

Until now, we consider, symmetry in XY plane (a=b), which will not be the case in general for the Voronoi structure. To have a complete picture of the accuracy of the method, variation of both c/a and b/a ratio is considered. The numerical values of the demagnetisation tensor W_{xx}, W_{yy}, W_{zz} and the trace of W are computed in figure 3.7. The results are in good agreement with the analytical expression given in 3.26. The errors are in agreement with the trace of W tensor. All 3 components (W_{xx}, W_{yy}, W_{zz}) have the same relative error as the trace illustrated in figure 3.7. The trace value for any shape is exact -1.0 for the self-demagnetisation W tensor. Large errors up to 4% are for aspect ratio c/a or b/a equal to 0.1. As the aspect ratio increases the errors decrease. This indicates the accuracy of the numerical implementation.

Here, the numerical implementation for computing the magnetostatic interaction has been tested for cuboid grains. For such shapes, just the diagonal terms of the W tensor are non-zero. All the results in this section have the non-diagonal terms at least 10 orders of magnitude smaller than the diagonal terms, which can be considered negligible. Having an uniform discretisation of the grains leads to errors of the W tensor proportional to the error in the trace. The overall error was less than 4% for aspect ratio c/a and b/a equal to 1, with the mention that the error in the numerical calculation is inversely proportional with the distance between grain. The overlapping grains (self-demagnetisation case), has the largest possible error. The cost of the high accuracy is the computational time.

3.4.2 Optimisation

One aspect, neglected so far is the computational speed of the naive method. For reference we will consider the discretisation of grains to be uniform with ix=iy=iz. For a single pair of source and field grains, the number of computations is ix^5 for each of the W tensor element and surface of source grain ; in total $54ix^5$ elements (fig. 3.9). The accuracy of the method increases with increasing number of discretisation in all 3 directions, as shown in the previous section, leading to huge increase of computation time. The surface-volume integral 3.25 can be reduced to surface-surface integral [66], which will reduce the computation time to $9ix^4$ multiplied by the number of surfaces for source and field grain. For cubic grains this lead to $324 * ix^4$ (fig. 3.9). To further optimize the calculation, the symmetry of the W matrix, the trace property of the W tensor and the symmetry properties of the 2D thin film geometry can be taken advantage of:

1. $W_{zz} + W_{yy} + W_{xx} = 0$; Just W_{zz} and W_{xx} is needed;
2. Symmetry of W tensor W. $W_{\alpha\beta} = W_{\beta\alpha}$;

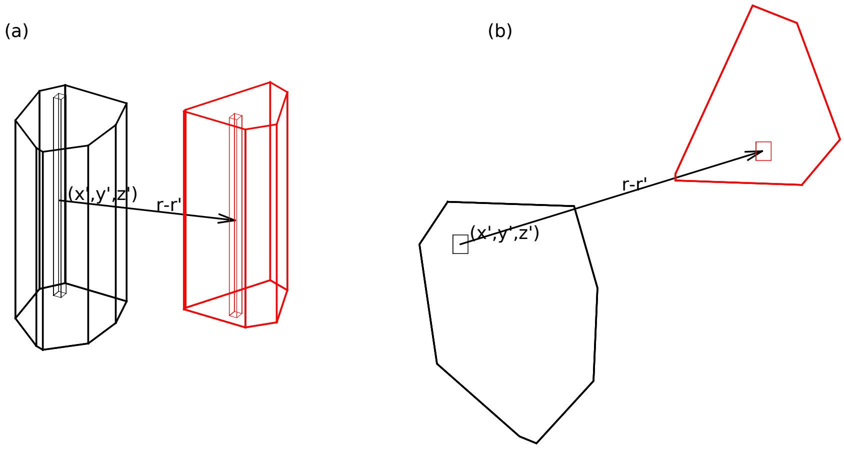

Fig. 3.8 3D and 2D geometry for magnetostatic calculation. The field at a point (x,y,z) inside a magnetic grain created by a second magnetic grain at (x',y',z').

3. Wzx and Wzy are zero;
4. Due to the fact that all grain have the same height and are in the same plane the double integral over z component of source and field grains can be done analytically.
5. The field created by the source on the field grain is equivalent with the reciprocal field. $W^{sf} = W^{fs}$ [5]. For a N by N granular system, it reduces the calculations from N^2 to $N^2/2$.

To calculate the double integral analytically, infinitesimal sections of the source and field grains are consider with h being the height of the grain (fig. 3.8). In this way the problem reduces from a 3D geometry (fig. 3.8a) to a 2D geometry (fig. 3.8b). For mathematical simplification, it can be represented as two lines of dipoles, expended in Z direction from 0 to h. Now, if the source and field line are connected by $r_{xy} = \sqrt{r_x^2 + r_y^2}$ each pair of points of the elements can be described by dipole matrix as follows:

$$W = \frac{1}{4\pi}\begin{bmatrix} 3r_x^2 \cdot f_5(z_s,z_f) - f_3(z_s,z_f) & 3r_x r_y \cdot f_5(z_s,z_f) & 3r_x(z_s - z_f) \cdot f_5(z_s,z_f) \\ 3r_y r_x \cdot f_5(z_s,z_f) & 3r_y^2 \cdot f_5(z_s,z_f) - f_3(z_s,z_f) & 3r_x(z_s - z_f) \cdot f_5(z_s,z_f) \\ 3(z_s - z_f) r_x \cdot f_5(z_s,z_f) & 3(z_s - z_f) r_y \cdot f_5(z_s,z_f) & 3(z_s - z_f)^2 \cdot f_5(z_s,z_f) - f_3(z_s,z_f) \end{bmatrix} \tag{3.27}$$

with $f_3(z_s,z_f) = \left[r_{xy}^2 + (z_s - z_f)^2\right]^{-3/2}$ and $f_5(z_s,z_f) = \left[r_{xy}^2 + (z_s - z_f)^2\right]^{-5/2}$. To obtain

$\int_0^h \int_0^h W dz_s dz_f$, four integrals must be calculated:

$$\int_0^h \int_0^h f_3(z_s, z_f) dz_s dz_f = -2\, {r_{xy}}^{-1} + 2\, \frac{\sqrt{{r_{xy}}^2 + h^2}}{{r_{xy}}^2} \tag{3.28}$$

$$\int_0^h \int_0^h f_5(z_s, z_f) dz_s dz_f = 2\, \frac{1}{\sqrt{{r_{xy}}^2 + h^2}\,{r_{xy}}^2} - 2\, \frac{1}{{r_{xy}}^3} + 4\, \frac{h^2}{\sqrt{{r_{xy}}^2 + h^2}\,{r_{xy}}^4} \tag{3.29}$$

$$\int_0^h \int_0^h (z_s - z_f) f_5(z_s, z_f) dz_s dz_f = 0 \tag{3.30}$$

$$\int_0^h \int_0^h (z_s - z_f)^2 f_5(z_s, z_f) dz_s dz_f = 4\, \frac{1}{\sqrt{{r_{xy}}^2 + h^2}} - 4\, {r_{xy}}^{-1} + 2\, \frac{h^2}{\sqrt{{r_{xy}}^2 + h^2}\,{r_{xy}}^2} \tag{3.31}$$

$$\tag{3.32}$$

The above equations are valid for non-zero values of r_{xy}, which means, they can not be used to calculated the self-demagnetisation tensor. This not a problem, as the main aim is to replace inter-grain dipole interaction approximation. Based on equations 3.28-3.31, each component of the W matrix can be determined:

$$W_{xx} = \frac{r_x^2}{r_{xy}^3} \left[\frac{1}{\sqrt{1 + (h/d_{xy})^2}} - 1 + 2 \frac{(h/d_{xy})^2}{\sqrt{1 + (h/d_{xy})^2}} \right] + \frac{1}{r_{xy}} \left[- \frac{1}{\sqrt{1 + (h/d_{xy})^2}} + 1 - \frac{(h/d_{xy})^2}{\sqrt{1 + (h/d_{xy})^2}} \right] \tag{3.33}$$

$$W_{yy} = \frac{r_y^2}{r_{xy}^3} \left[\frac{1}{\sqrt{1 + (h/d_{xy})^2}} - 1 + 2 \frac{(h/d_{xy})^2}{\sqrt{1 + (h/d_{xy})^2}} \right] + \frac{1}{r_{xy}} \left[- \frac{1}{\sqrt{1 + (h/d_{xy})^2}} + 1 - \frac{(h/d_{xy})^2}{\sqrt{1 + (h/d_{xy})^2}} \right] \tag{3.34}$$

$$W_{zz} = \frac{2}{r_{xy}} \left[\frac{1}{\sqrt{1 + (h/d_{xy})^2}} - 1 \right] \tag{3.35}$$

$$W_{xy} = W_{yx} = \frac{r_x r_y}{r_{xy}^3} \left[\frac{1}{\sqrt{1 + (h/d_{xy})^2}} - 1 + 2 \frac{(h/d_{xy})^2}{\sqrt{1 + (h/d_{xy})^2}} \right] \tag{3.36}$$

$$W_{xz} = W_{yz} = W_{zx} = W_{zy} = 0 \tag{3.37}$$

Using equations 3.33-3.37 in the numerical implementation instead of the surface-volume integrals, has a series of advantages:

1. The calculation cost is reduced to $3ix^4$ (fig. 3.9), which speed up the calculations by 2 orders comparison with the naive approach.

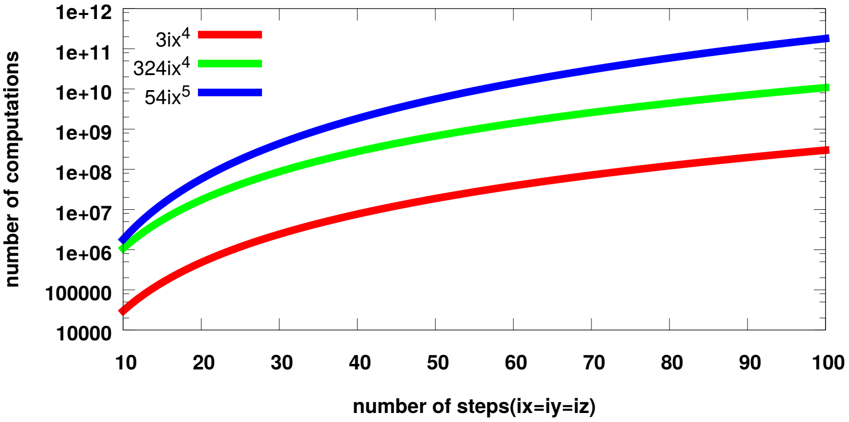

Fig. 3.9 The computational cost of magnetostatic using the surface-volume method, $54ix^5$ (blue), surface-surface method, $324ix^4$ (green) and the new surface-surface method based on 3.33-3.37, $3ix^4$ (red).

2. The matrix properties (trace and symmetry) are always retained, by the fact that this properties are directly present in the equations 3.33-3.37, instead of being a result of the surface-volume integration.
3. The same accuracy as surface-volume is obtained with a smaller ix value, leading to a much higher speed up in the actual calculations (fig. 3.8).

Now a last test for cubic shape grain is performed. The magnetostatic interaction is calculated for a grain at the centre of the coordinate system and the second at z=0, x=y. Both grains have identical shape. The numerical results using both the surface-volume integration (eq. 3.25) and surface-surface integration (using the analytical double integration on Z .eq 3.33-3.37) are compared with the analytical results (figure 3.10). The latter one is labelled as h-h integral. To investigate the accuracy of the results, the exact solution provided by Newell

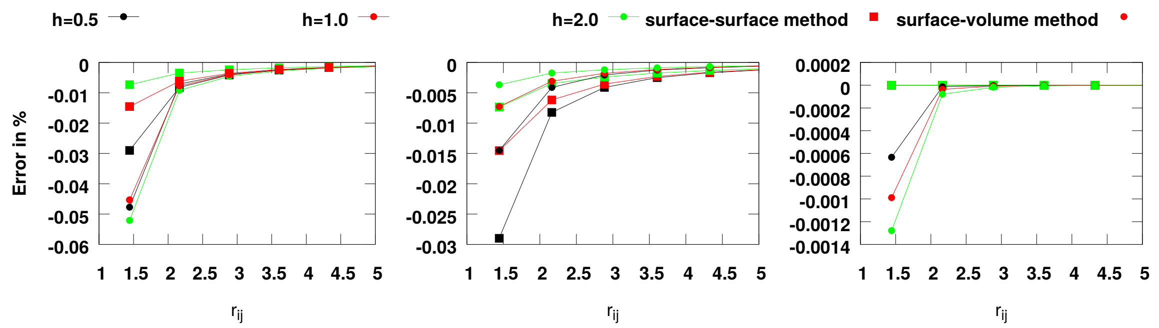

Fig. 3.10 Demagnetisation factor, $W_{xx} = W_{yy}$ (left), W_{zz} (centre) and the trace of W (right), as function of distance between grains. The surface-volume method (circle) and the optimized surface-surface method (square) are compared. The lines are to guide the eye.

[66] is used:

$$W_{xx} = \frac{1}{4\pi}\frac{2F(x,y,z) - F(x+a,y,z) - F(x-a,y,z)}{abc} \tag{3.38}$$

$$F(x,y,z) = F1(x,y,z) + F1(x,y+b,z+c) - F1(x,y,z+c) - F1(x,y+b,z) \tag{3.39}$$

$$F1(x,y,z) = F2(x,y,z) - F2(x,y-b,z) - F2(x,y,z-c) + F2(x,y-b,z-c) \tag{3.40}$$

$$F2(x,y,z) = f(x,y,z) - f(x,0,z) - f(x,y,0) + f(x,0,0) \tag{3.41}$$

$$f(x,y,z) = \frac{y}{2}\left(-x^2+z^2\right)\phi\left(\frac{y}{\sqrt{x^2+z^2}}\right) + \frac{z}{2}\left(-x^2+y^2\right)\phi\left(\frac{z}{\sqrt{x^2+y^2}}\right) - \tag{3.42}$$

$$xyz \arctan\left(\frac{yz}{x\sqrt{x^2+y^2+z^2}}\right) + \left(\frac{1}{3}x^2 - \frac{1}{6}y^2 - \frac{1}{6}z^2\right)\sqrt{x^2+y^2+z^2} \tag{3.43}$$

with $\phi(x) = arcsinh(x)$. The other two components, W_{yy} and W_{zz} are obtained by permutation of coordinates. A similar equation is given for the off-diagonal components [66]. The self-demagnetisation term used in 3.26 can be also obtained from the above equation using the limit of x,y,z tending to zero.

A systematic study of errors was performed and in figure 3.10 just 3 aspect ratios are selected c/a=0.5,1.0 and 2.0 are selected for illustration. For numerical method the in-plane discretisation (ix=iy) is 50. For all cases the errors for $W_{xx} = W_{yy}$ (fig. 3.10-left) and W_{zz} (fig. 3.10-centre) are less than 0.1%. Analysing the trace (fig. 3.10, the surface-surface method has overall smaller errors than the surface-volume method.

To put in context the numerical calculation of the magnetostatic interaction, different levels of approximation are investigated. For the same position of grains as in the previous section (z=0,x=y), 4 methods are compared. The first three are the expansion in eq. 3.16. The last one is the h-h integral. For simplicity, just the W_{zz} component is analysed, as this is the most relevant component for a 2-dimensional system. The errors of the above mentioned methods for a particularly significant case, where the two grains are identical cubes (aspect ratio c/a=1), are shown in figure 3.11. The methods do not take into consideration the shape of the grains, just the height. Nevertheless the dipole approximation has the lowest errors from all the approximation considered here. The errors are less than 3% for close grains. The other expressions have significant larger errors for grains at a distance smaller than 5 grain size: errors large up to 25% for h-h integral equation and up to 15% for the 2nd and 4th order approximation. For all four method, the errors decrease with increasing distance between grains. The results, suggest that dipole approximation is the most accurate from the four considered here. These is valid just for cuboid shape and aspect ratio 1, but it not true for for different aspect ratio or different shapes (fig. 3.11).

The dipole approximation, for any aspect ratio different than c/a=1, has huge errors (fig. 3.12). The errors as function of distance and aspect ratio for the same conditions (z=0,x=y) as before are given in figure 3.12 for dipole approximation (top left), 2nd order approximation (top right), 4th order approximation (bottom left) and the height integral (bottom right). For aspect ratio c/a larger than 1, dipole overestimates the magnetostatic interaction and for c/a smaller than 1 is underestimating the interaction strength. Considering the 2nd and 4th order approximation, the error decrease, in particular for distance larger than 2 grain size. The h-h

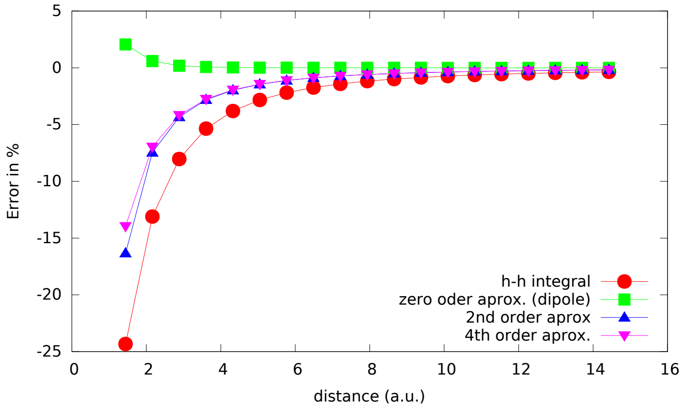

Fig. 3.11 Error of different approximations for magnetostatic interaction of cubic shape($a = b = c$): dipole approximation (green square), 2nd order approximation (blue triangle), 4th order approximation (violet triangle) and the height integral (red circle). Dipole approximation has an error up to 3%, far better then the other 3 methods.

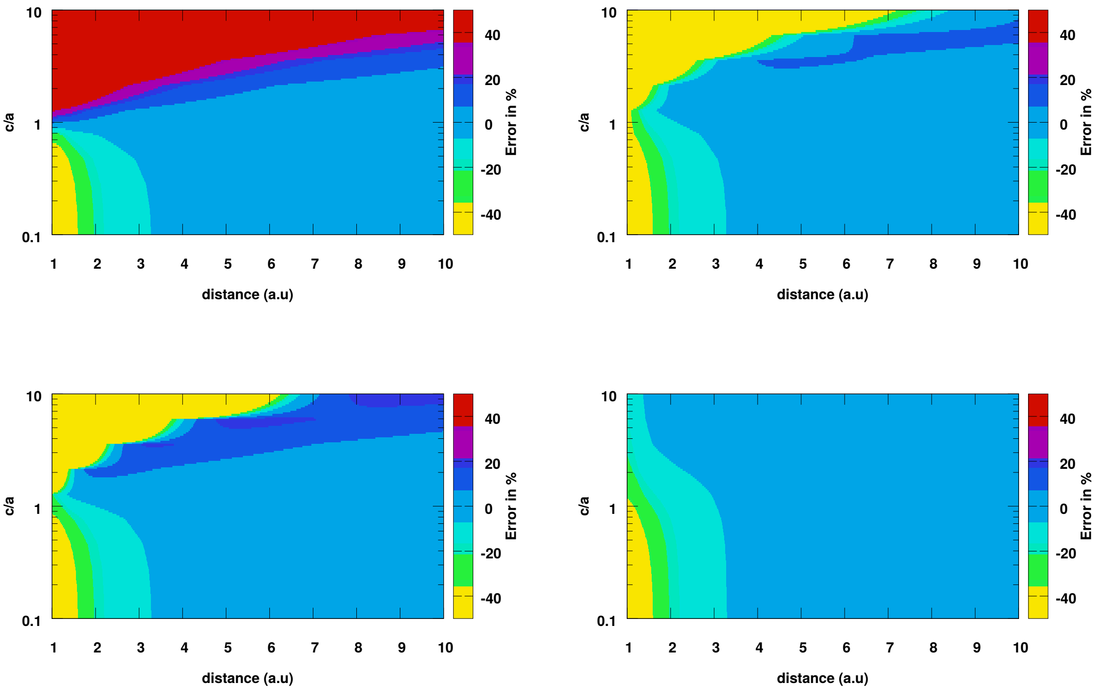

Fig. 3.12 Error in determination of magnetostatic interaction using different level of analytical approximations: dipole approximation (top left), 2nd order approximation (top right), 4th order approximation (bottom left) and the height integral (bottom right).

integral method has similar errors with the other 3 for aspect ratio smaller than 1, but smaller errors for tall grains(c/a>1).

3.5 Voronoi structure

For a voronoi structure, the are no analytical solutions to calculate the magnetostatic interactions. To test the numerical implementation, the surface-surface method based on h-h integral approach, and the naive surface-volume method are compared and also compared with an independent numerical implementation provided by J. J. Miles [69]. The tests are done for different pairs of source and field grains with different aspect ratios, and in figure 3.13 one example is selected. The difference is calculated with respect to the surface-surface implementation as $diff(A) = 100(numerical1(A)/numerical0(A) - 1)$, where $numerical0$ is the result of the surface-surface implementation. A discretisation of ix=iy=10 is used here as a balance between accuracy and calculation time. One of the grain is centred in the origin

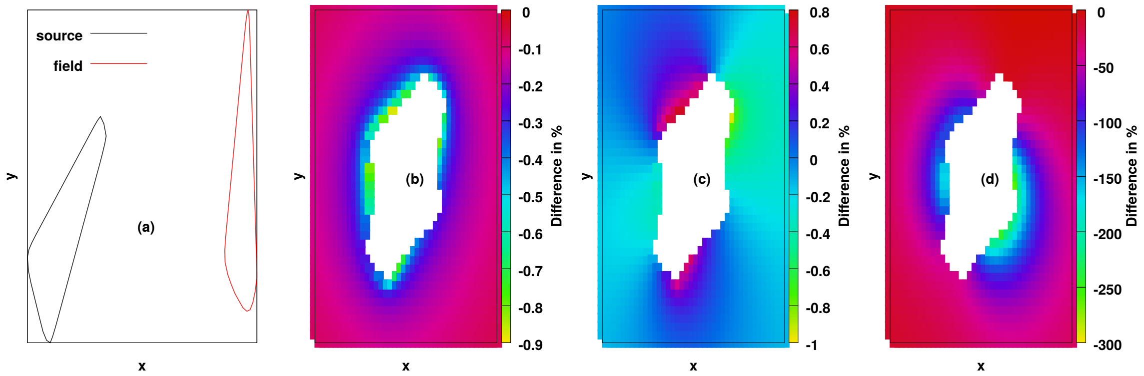

Fig. 3.13 Comparing the magnetostatic tensor (W_{zz} component) for two particular source and field grains illustrated in (a) as a top view. The error is calculated with respect to the surface-surface implementation. the two numerical method used here (surface-surface and surface-volume) (b) and the numerical calculation provided by J. J. Miles (c) are within 1% difference. The dipole approximation (d) is underestimates the value. The colour corresponding to the difference are centred at the grain centre position, with the latter varied in a small region around the second particle such that they do not overlap. The white region corresponds to the centre of the grain for which the two grains overlap.

of Cartesian coordinates, and the second grains centre is placed at different position around the first, with the condition to not overlap. The white region in figure 3.13b-d corresponds to the centre position in which the grains overlap and the magnetostatic tensor in not calculated as it is not a physical scenario. The differences are plotted at the centre of the second grain. Both the naive surface-volume integral and results from J.J. Miles are in agreement with differences smaller than 1%. On the other hand, the dipole approximation has larger differences of the order of 100%. Using the numerical method discussed here, the magnetostatic interaction will be significantly improved in comparison with the dipole approximation as suggested by figure 3.13.

Now, a 2D system of grains having a packing density, pkdst, is considered. Formally we can write the interaction based on eq. 3.5 as the summation of the inter-grain interaction (first term in eq. 3.5) and self-demagnetisation component (second term):

$$H^{int}_{system} = \sum_{i \neq j} W^{ij} M_j + \sum W^{ii} M_i \tag{3.44}$$

In uniform magnetisation on Z direction, the mean field results apply and for a infinite 2D system of grains, having a packing density (pkdst), the demagnetisation tensor for the entire system is zero except the W_{zz} component, which has the value equal to the pkdst.

For recording system considered in this thesis, with the voronoi structure defined in section 2.3 and the properties given in table 2.1, the packing density and respectively the W_{zz} are 0.8. Due to randomness of grain shape and area, there will be a distribution of the W tensor, with the mean value converging towards the mean field results. In figure 3.14, the distribution of W_{zz} from the inter-grain interaction, self-demagnetisation and sum of the two is given. The inter-grain interactions is smaller than the uniform magnetisation prediction of pkdst (0.8 in this case). The rest of the contribution consists of the self-demagnetisation term. This term is usually included in the effective anisotropy and therefore is not considered in the interaction.

3.6 Conclusion

For accurate description of magnetostatic coupling grains in recording media, the dipole approximation was replaced with numerical calculation of the magnetostatic tensor. For one source grain and field grain, the naive approach consists of 5-fold integral: a double integral over all surfaces of the source grain and a triple integral over the volume of field grain. This approach is computationally slow.

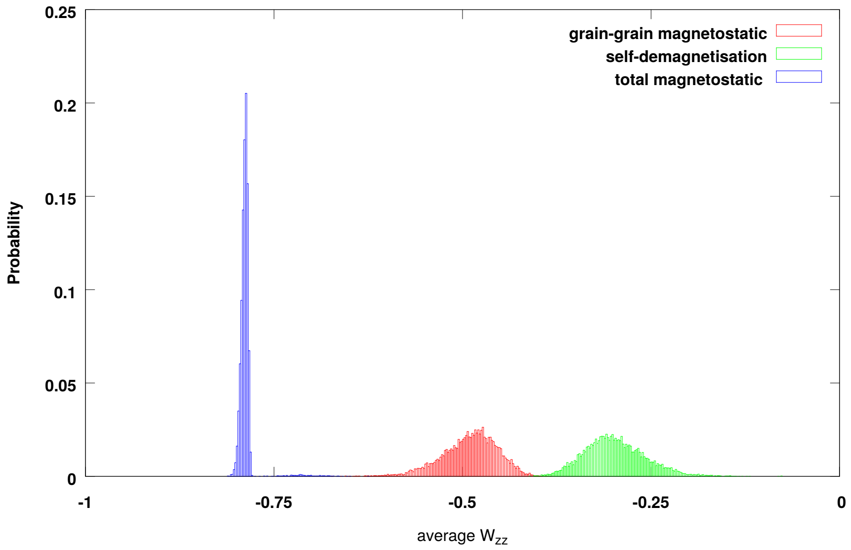

Fig. 3.14 The W_{zz} component of the magnetostatic tensor for 2D voronoi structure used in recoding media. The voronoi consider here is the one described in section 2.3 and the properties given in table 2.1.

The analytical solution for two interacting grains can be done in specific cases, such as cuboid shapes [66]. Also higher order approximations improve the results at large grain separation but have significant errors at small separation and the errors depend strongly on the grain shape. Therefore the numerical approach is used.

To improve computational cost, we use the property of recording media, that the height of the grains is constant. This allows analytical calculation of the two integrals over the grain height, reducing the numerical calculation to a 3-fold integral. Following this approach the calculation time is reduced by a few order of magnitude. The methods are tested against analytical results for cuboid grains, and with independent calculation provided by a collaborator. For the rest of the thesis the magnetostatic interaction is computed based on the method developed in this section.

Chapter 4

Interaction effects in PMR

The properties of PMR media are based on 1) intrinsic granular system properties such as anisotropy value, easy axis orientation, grain size and the corresponding distribution, 2) thermal effects and 3) exchange and magnetostatic interactions. In a non-interacting case, the magnetisation reversal of the system is defined by the reversal process of each grain. Due to interactions, the grains will form magnetic clusters, characterised by a group of grains having collective or correlated behaviour. Strong interactions leading to correlated behaviour have two important implications: firstly, a magnetic cluster reversal will differ from the individual reversal of the cluster elements leading to an overall decrease or increase of the reversal field. Secondly, the reversal process of a given region in space may expand outside the desired region. The second case is especially important for the bit storage on an ensemble of grains. Switching one bit can lead to a spread of the domain structure outside the bit region, affecting the neighbouring bits. The effect of cluster size via magnetic inter-grain correlation on high density recording has been studied in terms of SNR and bit-error-rate. The work of Mehta et.al [70], where different PMR devices were studied, showed that the major improvements in the areal density are due to reduction of the cluster size. Any further improvements of the recording media areal density requires not just reduction of the grain size, but also tuning the exchange interaction to balance the increasing magnetostatic interaction and thus controlling the cluster size [70].

In this chapter, the interaction effects are studied by modelling 3 types of experiments: magnetic hysteresis loops, a demagnetised state produce by an AC external field and magnetic relaxation experiments in zero external field. The system used is described in table 2.1. In the first part, two methods are introduced to investigate different magnetic configurations: magnetic correlations and volume grains. For PMR, the magnetic configuration is described by a domain structure with two possible orientations. A magnetic domain is a connected region of grains with the same magnetic moment orientation. We will show that characterising the domain in terms of the number of grains per domain (*ds*) is not a relevant quantity to probe the effect of interactions. Due to the statistical nature of the magnetic moment switching events (for each grain) between the two possible state, the domain structures always appear, even in a non-interacting system. Thus it is important to distinguish between domains resulting from purely statistical nature of the system and those arising from the minimisation of the magnetic free energy in the presence of inter-particle interactions. We will use the term 'domain' to describe both cases because it is not possible to determine a criterion distinguishing between the cases. For the non-interacting case, of course, domains arise because of the statistical process. However, we will show that, for the case of magnetostatic interactions, domain structures are determined by a mixture of statistical process and interaction effects. Therefore the *ds* value is not just a consequence of inter-grain magnetic correlations induced by the interaction. In the literature, either the domain width or the correlation length is used to characterise the interaction effects from a specific magnetic configuration. In this chapter, the volume grains are introduced as an alternative way of describing the inter-grain correlation effects on the domain structure. Volume grains are grains with all nearest neighbours inside the domains. The results show that volume grains are very sensitive to magnetic interactions and are compared with the magnetic radial correlation function. For the study presented in this chapter, the properties of the system used are described in table 2.1.

In the second part of the chapter, the magnetic correlations and volume grains are used to study the effects of interaction during the relaxation curves in zero external field and during a hysteresis experiment. During the relaxation process, the average magnetisation decreases from the saturation value to zero net magnetisation, which is the equilibrium value in zero external field. In the presence of magnetostatic interaction, the relaxation curve can become non-monotonic, relaxing first to a negative magnetisation and then converging back to zero net magnetisation. The behaviour can be explained by a simple model based on a dimer system (a pair of magnetic moments).

Next, the interaction effects on hysteresis loop, coercivity and individual grain switching field are studied. The switching process in a non-interacting system depends on the intrinsic properties of the grains and on the temperature of the experiment. In this case, the switching field of each grain is used to determine the intrinsic switching field distribution (iSFD). Interactions change both the amplitude and the direction of the effective field acting on each grain leading to a more complex reversal process. Inter-granular correlations modify the intrinsic switching field of each grain leading to an effective switching field distribution (eSFD). In this part, the effects of interaction on eSFD are investigated.

4.1 Magnetic configuration in PMR

To access the magnetic configuration, experimentally, imaging techniques such as magnetic force microscope (MFM) are used. The magnetic map configuration are similar to the one simulated in figure 4.1 consisting of magnetic domains, which are regions of connected grains with the same magnetic moment orientation. For PMR the domains are either magnetised "up" (along the positive Z-direction) or "down" (along the negative Z-direction). In the literature there is a discussion on how to define the relevant cluster size and the nature of the corresponding domains by using magnetic correlations or minimum domain width [33, 32, 64, 36]. Wang [71] defines the cluster size, as the lateral magnetic correlations length, whereas X. Wu [32] defines the relevant cluster size in PMR as the domain width.

It is known that magnetostatic interaction forms magnetic configurations corresponding to flux closure loops, for longitudinal recording, and for perpendicular recording media the magnetic configurations consist of long stripe domains. The energy of a system in zero magnetisation is given by the magnetostatic energy and exchange energy cost of forming the corresponding structures. For a stripe domain, the magnetostatic energy is given in the literature as [72, 73]:

$$E_{mag} = \frac{32W_{dm}M_s^2}{\pi^2 h} \sum_{i=1}^{\infty} \left[\frac{sin^2(i\pi/2)}{i^3} \frac{sinh(iq)}{sinh(iq) + \sqrt{1+1/Q}cosh(iq)} \right] \tag{4.1}$$

where Q is the quality factor: $Q = K/(2\pi M_s^2)$ and q= $\pi h/(2W_{dm})\sqrt{1+1/Q}$. W_{dm} is the domain width. Peng et.al [64] define an upper limit for "i" in the above equations assuming the minimum cluster is defined by twice the grain size: $i_{max} = (2W_{dm})/(D\sqrt{1+1/Q})$. Following the work in reference [64] the domain wall energy is:

$$E_{exch} = \frac{M_s H_{exch} D}{4W} \tag{4.2}$$

From equation 4.1 it can be observed that anisotropy has an important role in the domains energy and implicitly in domain width. On the other hand 4.2 does not have any contribution from anisotropy, which is an approximation as it has been shown that the domain width is inversely proportional to the anisotropy value [64].

The above equation does not consider the complicated structure of domains. For the system considered in section 2.3 table 2.1, the magnetisation map at coercivity is illustrated in figure 4.1 for exchange field of 0 and 6 kOe. The stripe domain is characteristic of magnetostatic dominated systems (figure 4.1a), but with increasing exchange interaction the domain structure will be characterized by more symmetrical circular clusters (figure 4.1b).

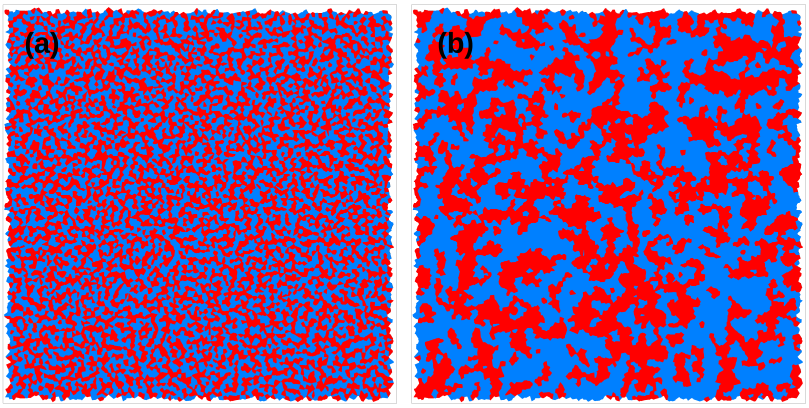

Fig. 4.1 The magnetic moment configuration at coercivity for exchange field 0 (a) and 6 kOe (b).The magnetostatic field is 4.6kOe. (a): In the case of magnetostatic interaction (0 exchange field) the stripe type domain structures are formed due to the tendency of magnetostatic interactions to produce 'antiferromagnetic-like' configurations. If exchange interaction is present (b) the domain structures become more symmetrical.

In a recent work [36], Papusoi suggested a checkerboard domain pattern to describe the more symmetrical domains. The experimental results based on magnetic force microscopy are not in agreement with either of the two approaches [36]. Another aspect that requires attention is the presence of temperature and how the configuration of magnetic moment is obtained. The above approach is based on energy minimisation which is characteristic of the ground state of the system. In general, the magnetic configurations are considered for a demagnetisation state (zero net magnetisation) obtained by a sequence of applied field, which does not necessarily imply a ground state configuration is accessed. Under these considerations, it is important to study the magnetic domain configuration.

To investigate the domain configuration, we show first that characterising the domain as the number of connected grains with the same orientation does not correlate well with the magnetic behaviour as will be discussed in the next section 4.1.1. Subsequently, volume grains are introduced and shown to be more relevant for the magnetic behaviour of the system. The domains will be investigated in terms of grains completely surrounded by nearest neighbours (NN) grains inside the domain (volume grains) or grains at the edge of the domain (surface grains). The surface grains, have at least one first NN grain outside the domain. This will be the focus of the next section. In the last section (4.1.2), the collective behaviour is studied using the magnetic radial correlation function. The configuration in zero net magnetisation obtained from hysteresis measurement at coercivity will be compared with a demagnetised state and the configuration corresponding to the ground state of the system. The demagnetised state is obtain by applying an oscillating magnetic field with decreasing amplitude. For the ground state the system is initialised in the remanence state and then let to evolve in time until reaching equilibrium. This time scales are beyond years and can not be investigated experimentally. The system used for these calculations is described in section 2.3 table 2.1.

4.1.1 Domain structure of PMR

The simulation results allow us to have direct access to the configuration map from where the domain properties can be extracted. Initially we characterise the domain using the quantity "ds" as the number of connected grains with the same orientation. An example is given in figure 4.2 for a non interacting system. The magnetic moment configuration is obtained from the hysteresis loop (fig. 4.2e) during the reversal from negative m_z to positive m_z. The number of grains per domain (ds) was separated into positive (red) and negative magnetisation (blue), with the total number of domains illustrated with black. In this example the domains configuration was studied at 4 values of magnetisation: -0.75 (a), -0.5 (b), -0.1(c) and 0 (d). At negative saturation, all the magnetic moments are in the negative Z-direction and therefore there is a single domain containing the entire system (ds=N, where N is the number of grains in the system). In a positive applied field, the magnetic moments of the grains start to reverse into the positive Z-direction leading first to individual grains reversed inside the large initial domain. As the applied field is increased and more grains are reversed, domains containing small numbers of grains are formed (fig. 4.2a for <m>=-0.75). With larger applied fields domains will join into single domains with large ds (fig. 4.2b for <m>=-0.5). Up to this point the initial domain still exists in the system, but with a smaller ds value. Eventually this domain will split in more domains (fig. 4.2c for <m>=-0.1) leading to the distribution at coercivity (fig. 4.2)d.

The asymmetry between the + and - Z-magnetisation domain in figure 4.2(d) arises from the volume distribution. The average magnetisation, assuming the applied field is on Z-direction, is given by:

$$< m >= \sum_i (M_s V_i m_i^z) \tag{4.3}$$

where m_i^z is the Z-component of the magnetisation unit vector. If all the grains had the same volume the domain size distribution would be symmetric. For a given volume distribution the small grains will reverse first due to lower thermal stability. Based on eq. 4.3, zero average magnetisation requires more grains with small volume to reverse, so that it balances the unreversed large grains.

In the example given above the domain formation is a consequence of the statistical nature of a system containing entities with just two possible states (magnetic orientation). For a 2D Voronoi tessellation, as considered here, a grain i will have the magnetic moment in one of the two states with a probability p_i. The probability p_i depends on the grain properties. Assuming all grains have the same probability, p, from percolation theory, an infinite domain is obtained if the probability of the two states is larger than a critical value (p_c) [74–78]. For the system described here, at coercivity the magnetisation will be 1 or -1 with the probability of approximately 0.5. The probability will be exactly 0.5 if all grains are identical (grain

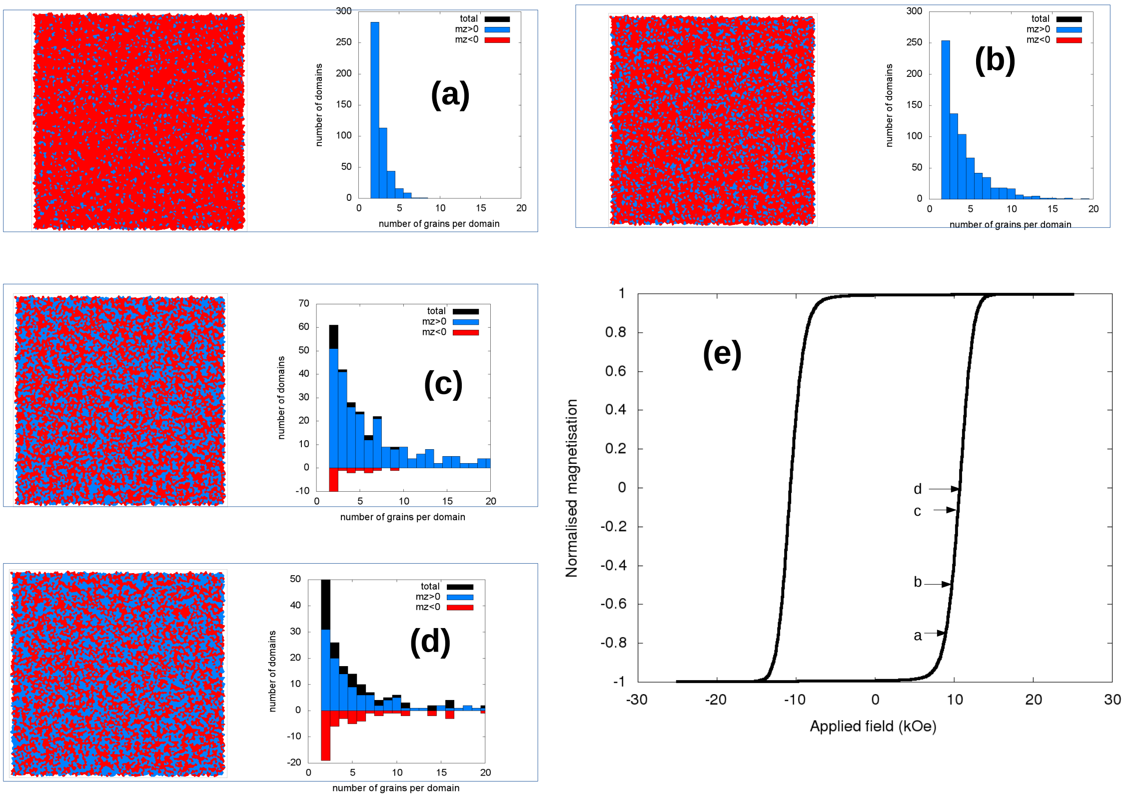

Fig. 4.2 (e) Hysteresis loop for a non-interacting system with the properties in table 2.1. (a)-(d) Magnetic configuration and the distribution of domain as function of number of grains per domain extracted from the hysteresis process along the reversal from negative magnetisation to positive. The information are extracted for normalised magnetisation of -0.75 (a), -0.5(b), -0.12 (c) and 0 (d). For illustration purpose all domain containing 100 or more grains are histogram at 100 grains. The distribution is separated based on the magnetic moment orientation in the negative Z-direction (red) and positive Z-direction (blue). The total domain size is represented with the black histogram. The asymmetry in the two orientation of the domains appear due to distribution of system properties, in particular volume distribution.

size,anisotropy value and easy axis orientation). Also the probability of having a domain with a given *ds* number of grains decreases exponentially with ds, with the exception of the infinite domain [74, 76]. Although the non-interacting granular system is more complex in terms of switching field dependence on grain size, anisotropy and temperature, the percolation theory indicates that defining the domain in terms of number of grains per domain is not sufficient as large domain structure will be present in the system [74–78].

Number of grains per domain,ds, is a combination of the statistical nature of magnetisation orientation (+ and - Z direction for PMR) and interaction influence. To have a large structure like a stripe domain, the extreme points of the domain need to be linked with grains having the same magnetisation. For large ds, the probability of a domain with size ,*ds*, is proportional to ds^{-a0} [79]. $a0$ is empirically calculated, and for a 2D square lattice has been found as 187/91 [79]. For a generic system, it is expected that the probability will be a product between a power law and an exponential decay function. The probability will increase with increasing number of NN grains. Next the volume grains are defined, which we will show are highly sensitive to interactions.

The volume grain can be formulated for a grain i as having all NN grains to $ni-th$ order the same orientation as grain i. For $ni = 1$, just nereast neibour grains are having the same orientation, for $ni = 2$ the first and second NN grains have the same orientation and so on. The probability for such a grain is:

$$P_V(ds, p) = p^{ds} \tag{4.4}$$

where ds is number of grain in the domain given by the number of nearest neighbours up to and including ni order. For the case of equal probability of the two magnetisation orientation (p=0.5), the probability of domains is given in figure 4.3b, based on the total number of grains inside the domain or based on the volume grains. The probability of a domain as a function of total number of grains is given in figure 4.3b with blue. The probability has a slow decay with larger domains (example $ds = 20$), having a more significant probability of appearing in the system in comparison with the volume grains [76]. The result is based on 4 NN grains and it is expected that the probability increases as function of number of nearest neighbour grains. The trend is similar with the granular media data, corresponding to both the non-interacting system and the magnetostatic interacting system. The magnetostatic interaction does not change significant the domain distribution in terms of ds as it favours the stripe type domains which already have a high probability just due to chance. On the other side, the probability of volume grains as the one illustrated in figure 4.3a (II) decreases much faster. The probability to have by chance all the nearest neighbours grains in the same

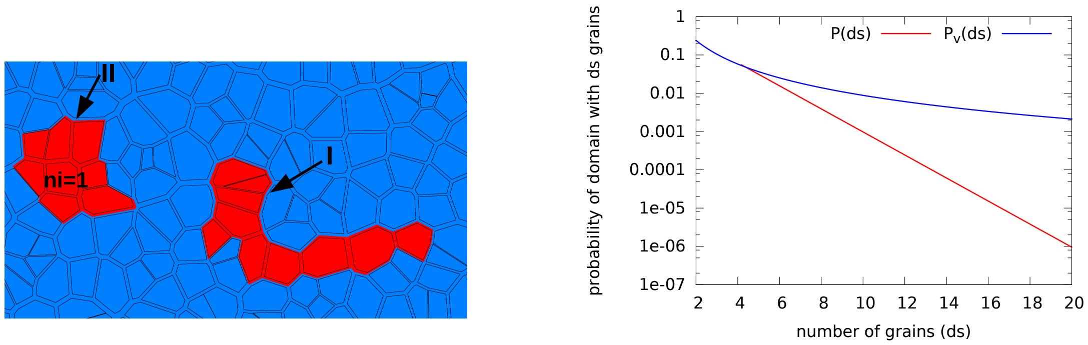

(a) (b)

Fig. 4.3 If a grain is completely surrounded with grains having the same magnetisation the domain is defined as volume domain. (a) Example of a stripe type domain containing no volume grains (I) and a domain containing a volume grain with index ni=1 (II). (b) Probability of a domain having ds grains(red, $P(ds) = ds^{187/91}$) and having the same number,ds, of volume grains (blue, $P_v(ds) = 0.5^d s$) as function of ds.

orientation is around 0.01 depending of number of NN grains. The probability of having also the second NN grains (approximately 20 grains in total) is extremely low (10^{-6}).

Based on the above results a domain can be separated into surface grains and volume grains of the domain. The surface grains define the edge of a domain and will have at least one NN grain of positive orientation and one NN grain of negative orientation. The volume grains of a domain are the grains having all the NN grains magnetisation parallel with the domain magnetisation. The latter, volume grains, are strongly effected by magnetostatic or exchange interaction. The magnetostatic interaction has an antiferomagnetic coupling, tending to align the NN grain in opposite direction and therefore decreasing the probability of volume grains. On the other hand, the exchange interaction has the opposite effect, aligning all the NN grains in the same direction, and thus increasing the probability of volume grains. Next, the volume grains are tested to check if they provide good information about the system behaviour under different interaction conditions.

To investigate the effect of magnetostatic interaction smaller packing density are considered, which correspond to a decrease of the magnetostatic interaction, with respect to the system described in table 2.1 ($< H_{mag} >= 4.6kOe$). The hysteresis loops are shown in figure 4.4a for a few values of magnetostatic field: 0.0 ,0.92, 1.84, 2.76, 3.68 and 4.6 kOe. The magnetic configurations are extracted at coercivity illustrating the domain structure in +Z-direction with blue and in the -Z-direction with red (fig. 4.4b-e). Complex stripe type domain structures are observed. For the same configuration the volume grains are plotted with gold in the corresponding figures 4.4f-i. The rest of the grains, which are surface grains, are illustrated with black. The effect of magnetostatic interaction, which tend to align neighbouring grains in opposite direction, is clearly illustrated by the decreasing number of volume grain with magnetostatic strength.

The previous magnetisation configurations are now characterised in terms of volume grains of the domain (figure 4.5a). The effect of exchange interaction is also investigated for $H_{mag} = 4.6kOe$ in figures 4.5d and for $H_{mag} = 0.0kOe$ in figure 4.5c. First, the difference between the total number of grain in a domain (ds) and volume grains is shown in figure 4.5. ds is the sum of the surface grains and volume grains. For all interaction condition considered

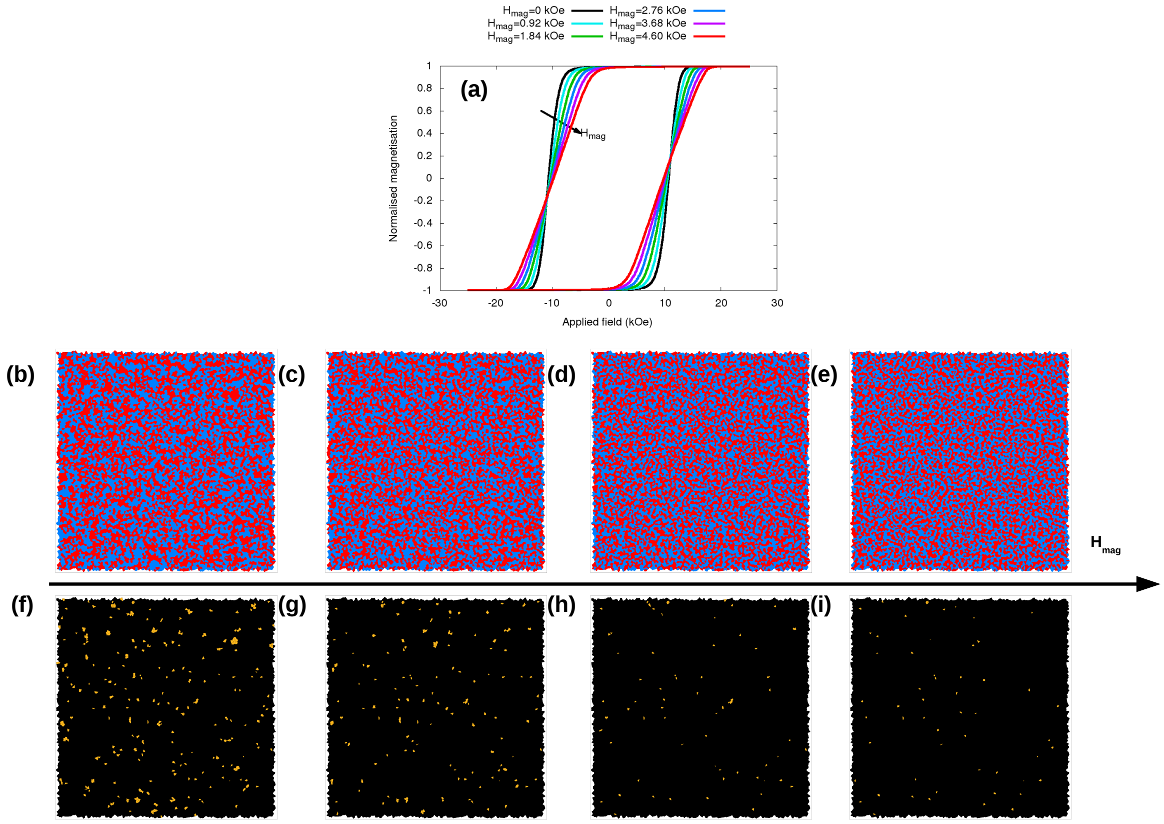

Fig. 4.4 (a) Hysteresis loop for different magnetostatic interaction strength from 0.0 kOe to 4.6 kOe. Magnetic moment configuration extracted from coercivity for H_{mag}= 0.0kOe (b) and (f); 0.92kOe (c) and (g); 2.76kOe (d) and (h); 4.60kOe (e) and (i). (b)-(e) are the domain configuration corresponding to the grains magnetisation on the positive Z-direction (blue) and negative Z-direction (red). The volume grains are illustrated with gold in (f)-(i) and the surface grains with black. The system forms complex stripe type domain structures (b-e), with the number of volume grains decreasing with interaction strength.

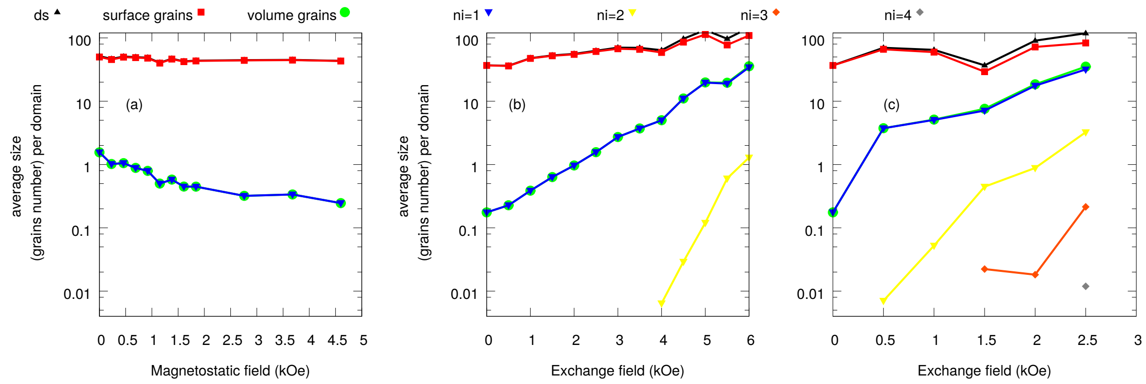

Fig. 4.5 The average number of grains per domain (black triangle), surface grains per domain (red squares) and average volume grains per domain (green circles) for magnetostatic (a) and exchange interaction (b). The results for a system with just exchange interaction is given (c). Also, the number of grains with all NN grains up to order *ni* inside a domain are included. If the magnetostatic interaction is considered (a), all the volume grains have just the first NN grains ($ni = 1$) inside the domain. For a system with magnetostatic and exchange (b), there are grains with first NN grains inside the domain ($ni = 1$) and also grains with first and second NN grains inside the domain ($ni = 2$). Larger NN index (up to $ni = 4$) are observed if just exchange interaction is considered.

here, ds is mainly dominated by the surface grains. These surface grains are weakly dependent on interaction, whereas the volume grains are strongly sensitive to interaction. From this point on we will investigate the volume grains.

The volume grains can be described by the maximum NN index (*ni*) for which all the NN grains magnetisation up to *ni* are parallel with the domain magnetisation. Information about the *ni* are also included in figure 4.5. The volume type grains are unfavourable to magnetostatic interaction due to the fact that the nearest neighbour magnetostatic interaction wants to align the magnetisation antiparallel. By increasing the magnetostatic interaction the volume grains per domain will decrease. This effect is shown in figure 4.5a where the volume grains decrease from 1.5 per domain in the non-interacting case to close to 0.2 per domain for 4.6kOe magnetostatic interaction. This is a clear indication of antiparallel coupling of NN grains and the fact that grains with opposite orientation are coupled together in a cluster. The systematic decrease of volume grains with increasing magnetostatic interaction is an indication that narrow stripe type domains are a good description for the domain configuration in the presence of just magnetostatic interaction.

The exchange interaction has the opposite effect (4.5b), as exchange interaction tends to align all the neighbour grain parallel to each other. The volume type grains are increasing as illustrated in figure 4.5b. The grains having at least the first NN grains are increasing in numbers up to 10 per domain for large exchange (6kOe). To simulate the effect of exchange dominated system, in figure 4.5c is considered the case where magnetostatic interaction is zero. In this case with increasing exchange interaction the volume domains will have large probability including domains having second, third or more levels of NN grains. For exchange 2.5kOe without magnetostatic interaction, volume domains containing grains with up to the $4th$ NN grains inside the domain are appearing. Presence of such domain limits the recording media as the domain size is similar to the bit size. Magnetostatic interaction reduces the presence of such large domain structures (figure 4.5b). For the system considered here, including magnetostatic interaction of 4.6kOe, the larger volume grain is of order $ni = 2$ and just for exchange larger than 4kOe. The increase of the number of volume grains and the presence of grains with large ni index with increasing exchange interaction indicates the change in the domain configuration from stripe type domain to more symmetrical domains. This is also shown in the domain configuration at the beginning of the section (fig. 4.1) where the configuration for 0 and 2.5 kOe exchange interaction is illustrated. Although the method can not fully describe the shape of the domains, the results presented here show that the volume grains are very sensitive to the interaction type (magnetostatic and exchange) and to the interaction strength and can be used to systematically characterise the domains.

4.1.2 Magnetic correlations

An alternative approach to investigate the magnetic configurations is using the magnetic radial correlation function. To investigate the coupling between grains due to correlated behaviour, the radial correlation function can be computed as following:

$$C_j(r) = \frac{\langle m_j(R_0) m_j(R_0+r)\rangle - \langle m_j(R_0)\rangle\langle m_j(R_0+r)\rangle}{\sqrt{\langle m_j^2(R_0)\rangle - \langle m_j(R_0)\rangle^2}\sqrt{\langle m_j^2(R_0+r)\rangle - \langle m_j(R_0+r)\rangle^2}}, \tag{4.5}$$

where $j = x, y, z$ and $m_j(R_0)$, $m_j(R_0+r)$ are pairs of of grains separated by a distance r. For PMR the Z correlation component is the one of interest. For a given distance, r, the correlation function $C_j(r)$ defines the amount of correlation corresponding to all the grains separated by that distance. A value of zero corresponds to a non-correlated system, +1 corresponds to complete positive correlation, meaning that all the magnetic moments at distance r from each other are align parallel and a value of -1 corresponds to anti-parallel alignment of the grains at the corresponding distance. Values in between mean, partial correlations.

The correlation function, offers two types of information. First it computes the average correlation strength as function of grain separation. Secondly the correlation function defines the type of inter-granular correlation: positive (ferromagnetic) or negative (antiferomagnetic). If the interactions are described by NN grains positive exchange coupling, the NN grains will tend to align parallel to each other in a ferromagnetic ordering, leading to positive correlation. If the NN grains are negatively exchange coupled, the system with tend to form domain boundary by aligning neighbouring grains anti-parallel, such as in an antiferromagnet, leading to negative correlations. The magnetostatic interaction has a more complicated behaviour due to the fact that it is a long range interaction. In PMR, magnetostatic interaction has an antiferomangetic effect ,tending to form stripe type domains. An important consequence of antiferomagnetic coupling is that the correlated behaviour is predominant between boundary grains of neighbouring domains. This implies that a domain is not equivalent with a magnetic cluster. Here a cluster is referred to as a group of particles that have a collective or correlated behaviour, which can be either ferromagnetic or antiferomagnetic in term of magnetic correlation function. Next the magnetic correlation method, will be applied for magnetisation configurations at zero average magnetisation obtained by 3 different approaches:

1. Performing a hysteresis loop and extracting the configuration at coercive field (zero net magnetisation).
2. Applying an AC magnetic field with decreasing amplitude until the system is demagnetised (zero net magnetisation) in zero applied field.

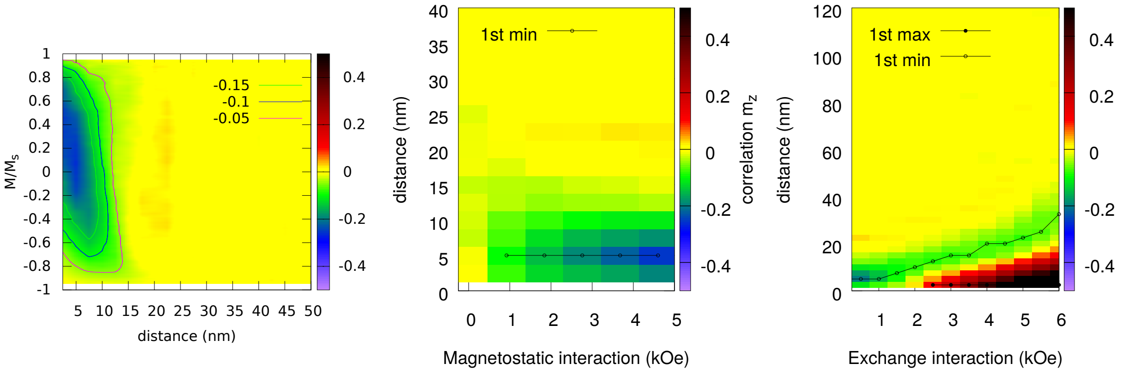

(a) (b) (c)

Fig. 4.6 (a) The magnetic radial correlation of the Z-magnetic moment component during a hysteresis measurements for a system with just magnetostatic interactions ($H_{mag} = 4.6kOe$). Contour line for correlation value of -0.05,-0.1 and -0.15 are plotted to guide the eye. The correlation at coercivity is extracted and study as function of magnetostatic interaction (b) and constant magnetostatic interaction (4.6kOe) and varying exchange interaction (c). The position of the minimum and maximum values of correlation function is plotted as points.

3. Initialise the system at remanence and let the system relax in time towards equilibrium. The final time is $10^{100}s$.

An example of the radial magnetic correlation during the hysteresis loop is shown in figure 4.6a for the case of a system with just magnetostatic interaction ($H_{mag} = 4.6kOe$). The results are plotted as colour map, with yellow corresponding to zero correlation. The correlation value increases from light red towards dark red for positive correlation and increases in absolute value from green towards purple for negative correlations. The magnetic correlation is negative for distances corresponding to the first NN grains and vanishes for larger distances. This is an indication of the stripe domain formation due to magnetostatic interactions. The correlations are extracted at coercivity and studied as function of interaction strength: magnetostatic interaction (fig. 4.6b) and exchange interaction (fig. 4.6c). Considering just magnetostatic interaction, the correlation is predominant for first NN grains, with no significant correlation for further neighbours. Including the exchange interaction, there is a competition between ferromagnetic and antiferomagnetic correlations. For weak exchange coupling the system is dominated by the magnetostatic interaction and the correlations are antiferomagnetic type and short range. With increasing exchange coupling, the magnetic correlation are extended to larger distances. The correlations become ferromagnetic at short distance and the antiferromagnetic correlations develop at larger distances. The hysteresis measurements involve dynamic evolution of the system with respect to the applied field direction and sweep rate.

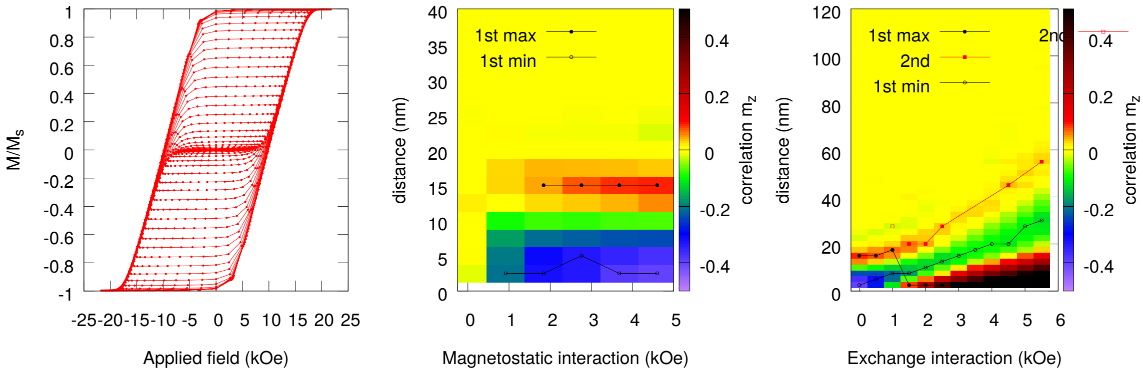

(a) (b) (c)

Fig. 4.7 (a) Magnetisation versus field curve for demagnetisation the sample using an AC magnetic field with decreasing amplitude. The results if for the system with magnetostatic interaction (H_{mag}=4.6kOe). The correlation is extracted at the demagnetisation state (zero net magnetisation) and study as function of magnetostatic interaction (b) and constant magnetostatic interaction (4.6kOe) and varying exchange interaction (c). The position of the minimum and maximum values of correlation function is plotted as points.

Another approach will consist of investigating the so called demagnetised state or erased state, which corresponds to a magnetisation configuration having zero net magnetisation without an external field. Ideally this will correspond to the ground state of the system, although that is not necessary the case. The demagnetised state can be obtained by applying a combination of external field sequence, in which the field amplitude and direction can vary. An alternative method is the thermal annealing of the sample, in which the sample is heated up until the system is demagnetised and then slowly cooled. The latter one is more challenging experimentally as it may require relative large temperature damaging the sample or the support material. Computationally, this approach, will require the temperature dependence of saturation magnetisation and anisotropy. A simpler method consists of applying an AC magnetic field with decreasing field amplitude over successive periods. If the field decreases too fast, the system can be trapped in a non-zero magnetisation state. To avoid this problem, a large number of cycles must be used. Here the field decreases to zero after 40 cycles. An example is shown in figure 4.7a for zero exchange field and 4.6kOe magnetostatic field. The process is repeated for varying magnetostatic and exchange field. The corresponding configurations are extracted (see appendix A fig. A.1) and the radial magnetic correlation is obtained considering just magnetostatic interaction (fig. 4.7b) and magnetostatic plus exchange interaction (fig. 4.7c). The results extracted from the AC field demagnetisation state show systematic variation in comparison with the ones extracted at coercivity. First the correlations are stronger for all the interaction conditions considered and also the correlation

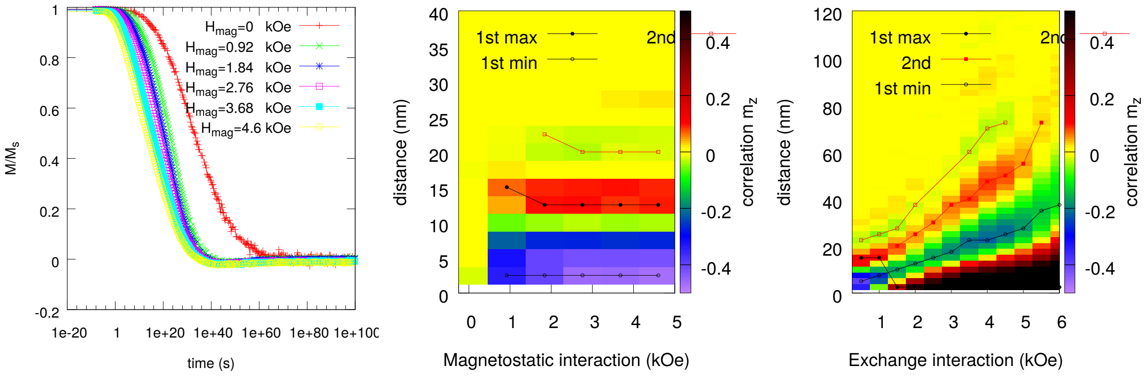

(a) (b) (c)

Fig. 4.8 (a) Average magnetisation of the system relaxing in zero applied field for a system with just magnetostatic interactions ($H_{mag} \in [0, 4.6] kOe$). The correlation is extracted at the end of the relaxation process when the system reaches its equilibrium state and study as function of magnetostatic interaction (b) and constant magnetostatic interaction (4.6kOe) and varying exchange interaction (c). The position of the minimum and maximum values of correlation function is plotted as points.

length is larger. This suggests that the applied field sweep rate ($10^4 Oe/s$) is fast enough to not allow the correlations in the system to evolve towards its maximum, during the hysteresis cycle. Before discussing the results, it is important to mention that a similar effect of the sweep rate is applicable for the procedure considered here to obtain the demagnetisation state [64]. The magnetic correlation has a damped oscillatory form. Ferromagnetic correlations emerge also if just magnetostatic interaction are considered. This is a consequence of the long range nature of the interactions and suggest that also grains in domain further away can be involved collective behaviour beyond the single domain. If exchange interaction is added to the system, the correlation length increases leading to multiple oscillations between ferromagnetic and antiferromagnetic correlation. Nevertheless the system is not in the ground state as shown next.

To access the system ground state, the following experiment is considered: a large magnetic field is applied and it is decreased to zero with a constant sweep rate. The sweep rate is taken to be the same as for the hysteresis loop, $R = 10^4 Oe/s$. Then the system is let to evolve in time until it reaches equilibrium. The relaxation time is given by the Arhenius-Néel relaxation time (eq. 1.11) and increases exponentially with the thermal stability factor KV/k_bT. For recording media the relaxation time will be many years. This is experimentally infeasible and also for most of the computational models. The kinetic Monte-Carlo method does not have any difficulties to simulate such large time scales. The calculation are performed with an adaptive time step. The calculation are initialised with

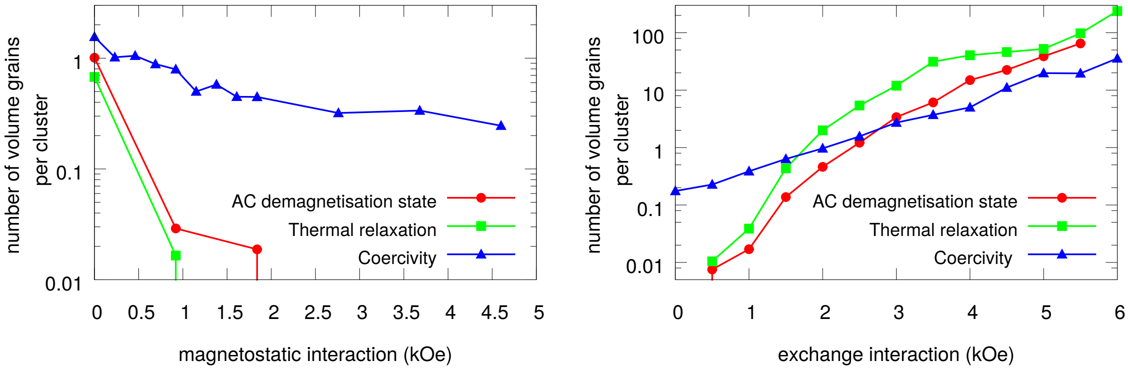

(a) (b)

Fig. 4.9 Domain statistics in term of number of volume grains per domain as function of (a) magnetostatic interaction and (b) exchange interaction for constant magnetostatic interaction (4.6kOe). The symbols and the colour defines the method from which the magnetic configuration was extracted: from coercivity (blue triangle), AC demagnetisation state (red circle) and magnetisation relaxation in zero field (green square). The later one corresponds to the system ground state.

a small time step ($10^{-8}s$). If the system's magnetisation has not changed, the time step is increased by a factor and the calculation is continued. If during the chosen time step, there is a large change in magnetisation, the system resets to the previous time step and the time step is halved. The simulated relaxation curves are illustrated in figure 4.8a, with the relaxation time larger than $10^{20}s$. After the zero magnetisation state is obtained, the system is allowed to evolve for a longer time until there are no variations in magnetisation and magnetic radial correlation. The final configuration is extracted and the corresponding correlation is computed. The results are given in figure 4.8b as function of magnetostatic interaction and in figure 4.8c for varying exchange coupling. Results confirm that the demagnetisation configuration obtained from the AC field is not the ground state of the system.

Next, the magnetic configuration produced using the 3 methods discussed above (coercivity, AC demagnetisation and magnetisation relaxation) are analysed using the volume grains, presented at the beginning of the section (fig. 4.9). Example of the magnetisation configurations is given in appendix A fig. A.1. The results are presented as a function of magnetostatic interaction without exchange interaction (4.9a) and with constant magnetostatic interaction (4.6kOe) and varying exchange interaction (4.9b). The volume grains are very sensitive to the type of interaction and interaction strength. In the presence of just magnetostatic interaction, the system ground state, obtained from magnetisation relaxation, corresponds to the presence of just surface grains. The volume grains strongly decrease in number with increasing magnetostatic interaction. A similar result is obtained from the AC demagnetisation configuration, but a much slower decrease of volume grains per domain is observed in configurations extracted at coercivity. These results are consistent with the correlations presented in fig. 4.6-4.8. The weaker correlation from the coercivity configuration in comparison with the ground state from magnetic relaxation, indicates that the reversal is not fully dominated by the correlated behaviour and the statistical nature of reversal due to thermal bath has an important role. Considering now, constant magnetostatic and increasing exchange interaction, the volume grains in the ground state should also increase as shown in figure 4.9b. At large exchange values (>4 kOe), the volume type grains become comparable with the surface grains and the system forms large cluster, as suggested also by the correlations. This effect needs to be avoided, as it can lead to cluster structures between neighbouring bits thus increasing the error in the information storage. The minimum value of correlation in the presence of both magnetostatic and exchange interaction is obtained for exchange value between 1 and 2kOe. This corresponds to the same range of exchange interaction for which the number of volume grains per domain is around 1, similar value as for the non-interacting case. In this range, statistically, the domains are similar to the non-interacting case.

4.2 Magnetisation relaxation in constant external field

An important property for recording media systems is the thermal stability over long time scales. The stored information must be preserved for at least 10 years. For this period of time, the magnetisation should not decay below a certain value. However, only due to thermal activation, the magnetisation decays inevitably towards its thermal equilibrium state. The transition over the energy barrier is given by the Arhenius-Neel law (eq. 1.11). In an applied field the equation becomes field dependent:

$$\frac{1}{\tau(H)} = f_0 exp\left(\frac{E_b(H)}{K_b T}\right) \tag{4.6}$$

The time dependence of the magnetisation can be described by the sum of the reversible and irreversible components. The reversible component of the magnetisation is constant in a fixed external magnetic field. The irreversible component corresponds to the magnetisation switching between the two states over the energy barrier based on the Arhenius-Neel law (eq. 4.6) for a given applied field, H, and in a given time t. The magnetic relaxation for a single energy barrier is then given by [80, 81]:

$$M(t,H) = A(H) \pm Bexp(-t/\tau(H)) \tag{4.7}$$

Experimentally this was confirmed by Street and Woolley under the consideration of wide energy barrier distribution[82, 2]:

$$M(t,H) = constant \pm S(H)ln(t) \tag{4.8}$$

With the sign depending on the starting point of the relaxation process (in positive or negative magnetisation). They described the process as magnetic viscosity and $S(H)$ is the coefficient of magnetic viscosity. For identical particles S can be directly extracted from equations 4.7. In practice the grains will not be identical, there are distribution of volume, anisotropy and other factors which produce a distribution of energy barriers. In this case the magnetisation time relaxation is:

$$M(t) = \int_0^\infty f(E_b)exp\left(-t/\tau(E_b)\right)dE_b \tag{4.9}$$

Next we consider the long time evolution of the system in a constant external field. The system is first saturated in a large positive field, afterwards the field is slowly decreased to zero ($R = 10^4 Oe/s$) and then the system is allowed to evolve towards the equilibrium state. Final time is of order 10^{100}s such that there are no significant change in the system behaviour (magnetisation or magnetic correlations: fig. 4.10). Thus we assume that the final state corresponds to the ground state of the system.

Here the evolution towards the ground state is investigated for different magnetostatic field and no exchange interaction (fig. 4.10a) and for magnetostatic field of 4.6kOe and different exchange strength (fig. 4.10b). To illustrate that the system does not evolve in terms of magnetic correlation, the magnetic radial correlation is computed along the relaxation process. A few examples are given in fig. 4.10c-e, where the strength of magnetic radial correlation is plotted as a colour map as function of time and grain separation. The magnetic relaxation process is accelerated by the presence of magnetostatic interaction (fig. 4.10a) due to the effective negative field arising from magnetostatic coupling. An important aspect is the non-monotonic shape of the relaxation curves in the presence of interaction. As magnetostatic interaction are included the magnetisation is first decreased below the zero magnetisation value before reaching the final value of zero magnetisation. This effects is enhanced by the presence of exchange interaction smaller than the magnetostatic interaction. When exchange interaction dominates ($H_{exch} > H_{mag}$) the effect disappears.

The non-monotonic behaviour can be reproduced using dimers containing two magnetic particle with very well separated relaxation times. To differentiate the relaxation of the two particles, they are given different sizes (A-small particle, B-large particle), with the small particle having a faster relaxation (fig. 4.11). Here a system containing identical pairs of

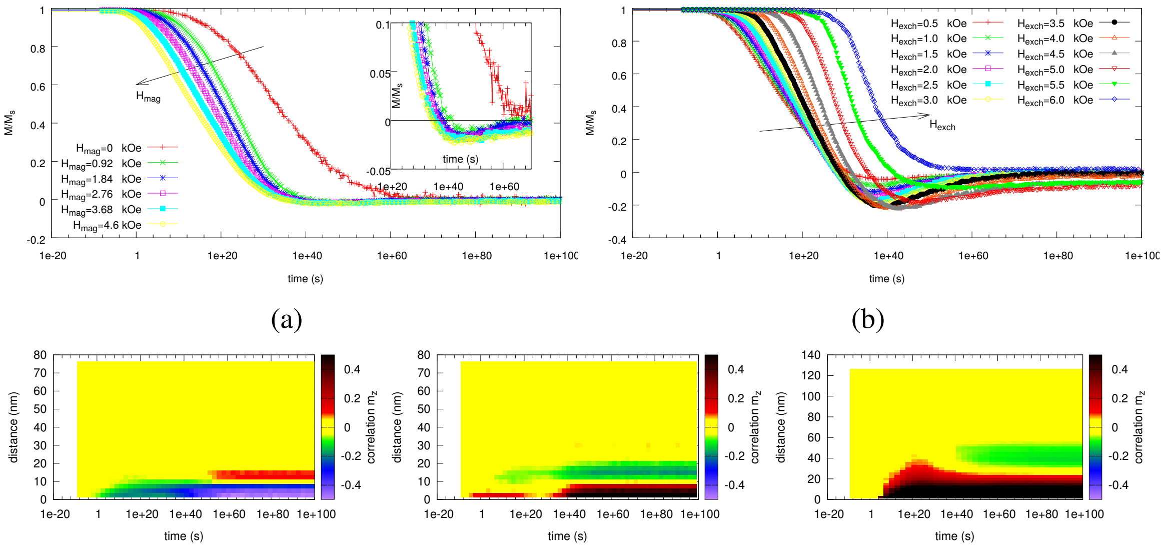

(a) (b)

(c) (d) (e)

Fig. 4.10 Magnetic relaxation curves in zero external field for different magnetostatic and exchange interaction conditions. No exchange and varying magnetostatic interaction lead to a faster relaxation process (a). For magnetostatic interaction of 4.6kOe and increasing exchange interaction the relaxation time increases (b). For a non-interacting system there is a monotonic decrease. Magnetostatic interaction induces a non-monotonic behaviour with magnetisation decreasing below 0 and then recovering towards 0 magnetisation (inset in a). For exchange strength smaller than the magnetostatic interaction, the non-monotonic effect is enhanced and for larger exchange value is vanishes. Correlation map for $H_{mag} = 4.6kOe$ and H_{exch} values of 0 (c), 2.5 (d) and 6 kOe (e). The strength of correlation is plotted as colour map as function of time and grains distance.

the two particles (dimers) is considered. The only interaction is the magnetostatic coupling between the two particles inside the dimer. There are no interactions between dimers. The easy axis of all particles is in the Z-direction and the dimers are formed in x-direction as illustrated in figure 4.11, such that the magnetostatic interaction produces a field just on Z-direction. The field is negative if the particle magnetic moments forming a dimer are aligned in the same direction and it is positive if the particles are aligned antiparallel. There are 4 possible configurations of the magnetic moment of the dimer illustrated in figure 4.11. For simplicity the transition between them are given by single particle switching. For example the transition from state 1 to 4 is possible via 1-2-4 or 1-3-4. The direct transition 1-4 and 2-3 are not allowed. The magnetic moment evolution in time can be computed from eq. 4.9, using the master equation formalism, as a sum of the 4 states with the corresponding

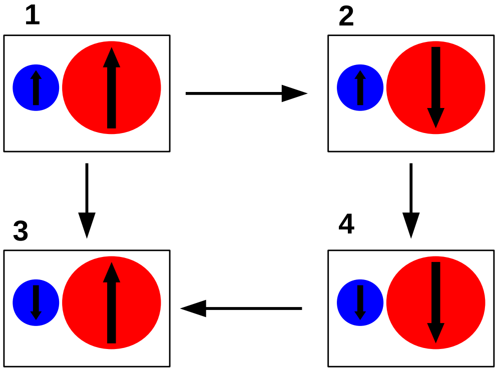

Fig. 4.11 The 4 possible configuration the dimer system can exhibit with the magnetisation of both particle up (1), or both down (4) or one up and one down (2 and 3). The arrows between configuration indicates the transitions the dimer can have.

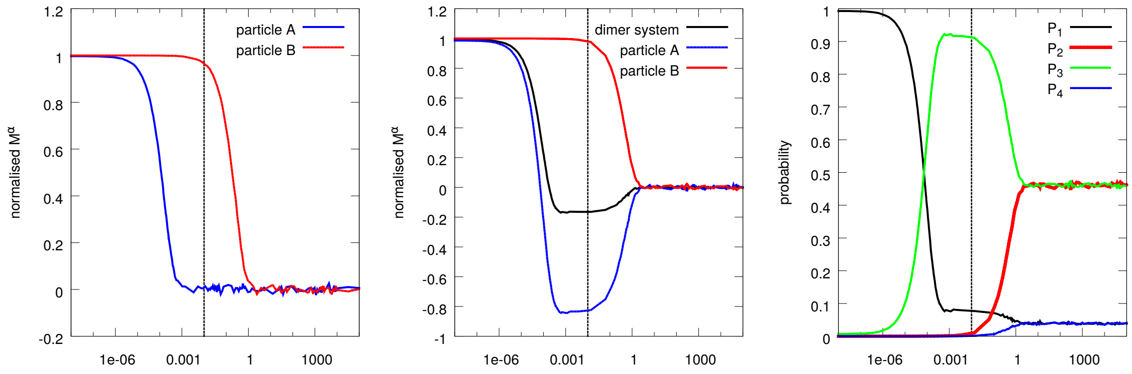

(a) (b) (c)

Fig. 4.12 Time evolution of the magnetic moment for the two particles in separated non-interacting system (a) and for the dimer system (b). The magnetisation of each type of particles is shown with blue for particle A and with red for particle B. The magnetisation of the entire system (AB) is represented with black. The probability evolution of each of the 4 possible states is given in (c) for the corresponding relaxation process illustrated in (b). The vertical dash line indicates the moment when particle B starts to relax.

probability [83–85]:

$$M^{\alpha}(t) = M_1^{\alpha} P_1(t) + M_2^{\alpha} P_2(t) + M_3^{\alpha} P_3(t) + M_4^{\alpha} P_4(t) \tag{4.10}$$

where M^{α} is the magnetisation of the partial α, with α=A,B or AB for the dimer, with $M^{AB} = (M^A V^A + M^B V^B)/(V^A + V^B)$. $P_{1,2,3,4}$ is the probability of the corresponding configuration.

A diagram of the relaxation curve in zero external field is illustrated in figure 4.12a for the individual particles of the dimer without any interactions. The relaxation curve for the dimer system and its components (particle A and B) are given in figure 4.12b. For the latter, the corresponding probabilities of the 4 configuration are shown in figure 4.12c. The vertical dash line corresponds to start of the relaxation process for particle B, indicating the separation of the relaxation time scales. The magnetic relaxation process for the dimers is done under an effective field, which in this case is the field from the magnetostatic coupling. For the case considered here, particle A will relax to zero before the particle B will start to relax (fig. 4.12). In this case the effective field acting on the first particle is up to this point a constant negative field and will lead towards a negative magnetisation corresponding the the equilibrium values in that effective field. From the 4 configuration probabilities, it is confirmed that the probability of both particles having positive magnetisation (P_1) is decreasing and the P_3 probability (small particle negative magnetisation and large particle positive magnetisation) increases. The other two probabilities are zero until the second particle starts to reverse. The corresponding time is illustrated in fig. 4.12 with vertical dash line. When $M_1^{AB}P_1 + M_3^{AB}P_3$ is zero the total magnetisation is zero and afterwards magnetisation decreases below zero. This process will continue until reaching equilibrium or the second particle starts to relax (P_2 and P_4 start to increase). After this point, both particles will eventually reach zero net magnetisation as P_1 is balanced by P_3 and P_2 is balanced by P_4. The key elements for the non-monotonic behaviour is the presence of a negative effective field during the first part of the relaxation when the average magnetisation becomes negative and large separation of the relaxation times. The separation of relaxation times is important as the negative effective field will be also present on the part of the system that does not have non-monotonic behaviour. The separation of the relaxation time is to ensure that on that part of the system, there is not significant influence from the effective field during the first part of the relaxation.

Going back to the PMR system from figure 4.10, the relaxation curves are separated into contributions from small and large grains. Using the distribution of grain size, the grains are partitioned in two subsystems based on the grain area with respect the average grain area of the system: the grains with smaller area are labelled as I and the one with larger area with II (fig. 4.13a). The relaxation curves of the system, and the two subsystems (I and II) (fig. 4.13b for $H_{exch} = 3kOe$) show the same behaviour as in the dimer system presented previously. The small grains exhibits the non-monotonic behaviour whereas the large ones do not. The presence of the negative effective field originating from inter-granular interaction is shown in figure 4.13c, where the average effective field over the entire system is extracted. The effective field is calculated as the local field acting on each grains at each time step. In zero

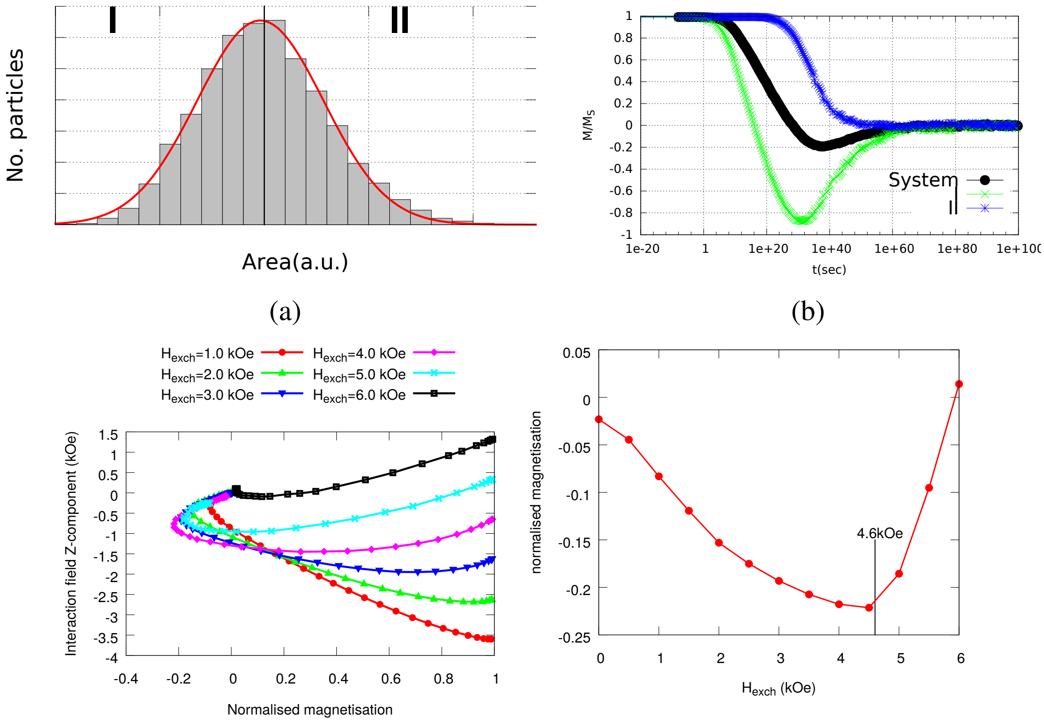

(a) (b)

(c) (d)

Fig. 4.13 (a) Diagram of the grain area distribution and the separation of the system in two subsystem: subsystem I contains all the grain with area smaller than the average grains size and the larger grains are in subsystem II. (b) The magnetisation relaxation curves for the entire system (black) and the two subsystems I (green) and II (blue). Data are from the case with $H_{exch} = 3kOe$. The average effective field as function normalised magnetisation during the relaxation process is given in (c) for different exchange values. The minimum magnetisation value reached during the non-monotonic behaviour is shown in (d). The vertical line corresponds to the 4.6kOe which is the value of the magnetostatic field in this system.

external field as considered here, the effective field is the sum between the magnetostatic field and exchange field. The average effective field is negative during the relaxation process and has a non-zero value in zero net magnetisation as it would be in a mean-field approximation. The presence of this average field leads to the non-monotonic behaviour. It is important to notice, that the exchange strength has an role in the non-monotonic behaviour. The minimum value of the magnetisation during the non-monotonic part has the maximum amplitude when the exchange and magnetostatic interaction strength are equal ($H_{mag} = H_{exch}$). The effect is diminishing at larger and smaller value of exchange in comparison with magnetostatic. The effect does not disappear if the exchange interaction is not present in the system and therefore endorsing the idea that the magnetostatic interaction is the key factor with the exchange interaction enhancing or suppressing the effect.

4.3 Hysteresis loop

The interaction effects on the hysteresis loop are investigated using the magnetic radial correlation function and volume grains of domains. The correlation corresponding to the m_z component of magnetisation during the reversal from m_z=+1 to m_z=-1 is illustrated as a colour map in figure 4.14. For the non interacting system (fig. 4.14a) there are some weak correlations (less than 0.05 in absolute value). This can arise from a correlation between grain volume and grains position. Small grains with similar volume, who are NN (nearest neighbours), will reverse at similar times due to similar thermal stability factor KV/k_bT. If magnetostatic interaction is added (fig. 4.14b), then more grains which are also NN will switch at the same time due to a combination of thermal stability factor and the coupling via the magnetostatic interaction. As the magnetisation decreases towards 0 the correlations are stronger and expand to larger distances. Afterwards as the reversal process evolves towards

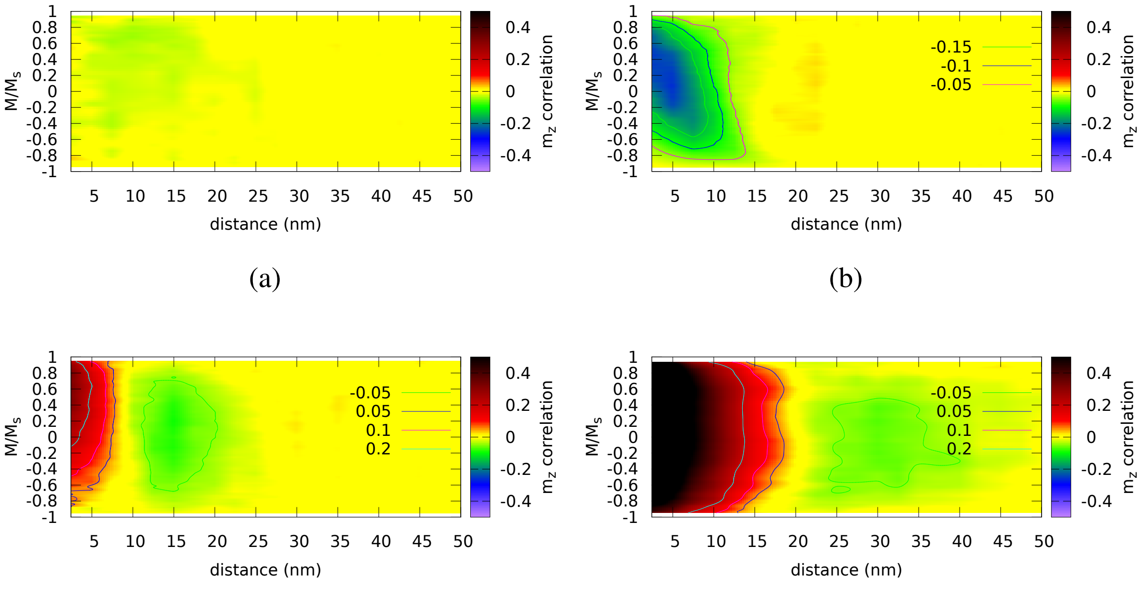

(a) (b)

(c) (d)

Fig. 4.14 Radial magnetic correlation for m_z during the hysteresis loop on the reversal process from +1 to -1. The results for non-interacting system is given in (a). The other 3 are for 4.6kOe magnetostatic interaction and exchange interaction of : 0kOe (b), 3 kOe (c) and 6 kOe (d). Contour line for correlation values in steps of 0.05 are also shown.

m_z=-1, the correlations decrease. Similar behaviour is for the system under both magnetostatic interaction and exchange interaction ($H_{mag} = 4.6kOe$ and $H_{exch} = 3.0kOe$). The correlation for this system in illustrated in fig. 4.14c. Now due to positive (or ferromagnetic) coupling from the exchange interaction, positive correlations appear at small distances corresponding to first NN grains, with some negative correlation developing at distances corresponding to second NN grains. Doubling the exchange interaction to 6.0 kOe, the correlations are expending to larger distances and become more symmetric around 0 magnetisation.

The extreme values of the correlations are extracted from the date illustrated in figure 4.14 and compared with the average number of volume grains per domain. The results are given in figure 4.15. In the presence of just magnetostatic interaction the positive correlation values are extremely low (fig. 4.15b), below 0.05 value, but the negative correlation are increasing with larger magnetostatic interactions (fig. 4.15a). The absolute value of the negative correlations is asymmetric during the reversal process (fig. 4.15a). During the first

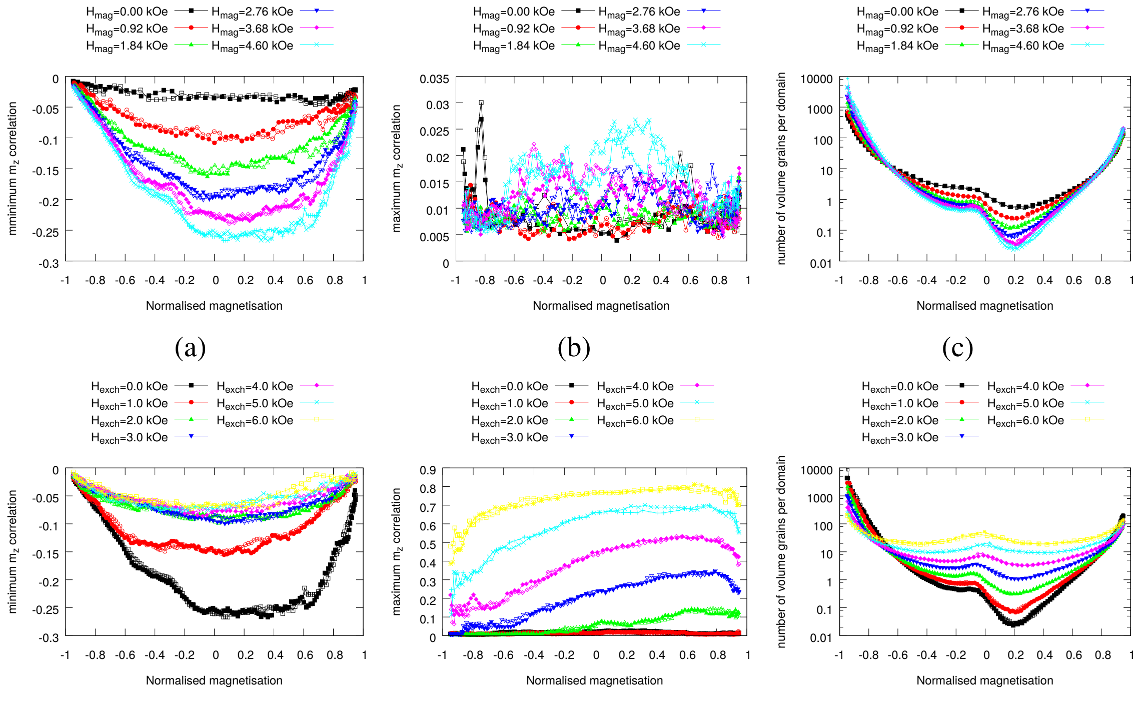

(a) (b) (c)

(d) (e) (f)

Fig. 4.15 Results from radial correlation function and volume grains during the reversal process on the hysteresis loop for m_z form +1 to -1. Top row (a-b) correspond for a system under just magnetostatic interaction and the bottom row (d-f) is for magnetostatic interaction of 4.6kOe and different exchange interaction strength. The extreme value of the correlations are extracted and the maximum values shown in a and d and the minimum value in b and e. Also the average number of volume grains per domain is given in c and f.

part of the hysteresis when the magnetisation decreases from 1 , the correlation increase (in amplitude) rapidly reaching the maximum amplitude before the magnetisation reaches zero, with a slow decrease of the correlation as magnetisation is evolving towards -1. Similar effects are observed from the volume grains characterisation of the domain structures (4.15c). The average volume grains per domain it is reaching a minimum for a magnetisation value of approximately 0.2, followed by a fast increase as the magnetisation is becoming negative and then a slow increase towards negative magnetisation. As exchange interactions are included and the exchange strength is increased the negative correlations from the magnetostatic interaction are decreased (in amplitude) (4.15d) and strong positive correlation emerge (4.15e). The positive correlation increases from 0 (for 0 kOe exchange) to 0.8 at 6.0kOe exchange field. This is reflected in the average number of volume grains per domain, which increase by 3-4 orders in magnitude in the same interval.

4.3.1 SFD

The intrinsic switching field distribution ($iSFD$) is a fundamental characteristic of granular magnetic materials as it determines the quality of recording media used in hard disk drives.

The intrinsic switching field distribution, $iSFD$, is defined as a distribution of irreversible switching events of magnetic grains in the absence of intergranular interactions. SFD provides direct information about the distributions of intrinsic material properties of grains, such as anisotropy, volume and easy axis. The intrinsic SFD can be described as [86]:

$$(\sigma_{iSFD})^2 = \left(\frac{\partial H_S}{\partial H_K}\right)^2 (\sigma_K)^2 + \left(\frac{\partial H_S}{\partial V}\right)^2 (\sigma_V)^2 + \left(\frac{\partial H_S}{\partial \alpha}\right)^2 (\sigma_\alpha)^2 + (\sigma^t_{SFD})^2 \tag{4.11}$$

where H_S is the average switching field; σ_K and σ_V are the width of the anisotropy and volume distribution. The easy axis distribution σ_ϕ is related with α in the above equation, with some values tabulated in reference [86]. In an thermal case, the SFD is described just by the distributions of easy axis, volume and anisotropy. In the presence of thermal bath, the SFD has two contributions from thermal effects: one from the average switching field (H_S) and an extra component from thermal activation, σ^t_{SFD}. Due to all of these contributions the SFD becomes non-linearly dependent on the field sweep rate of the external field applied during the hysteresis loop measurements. If just the contribution from anisotropy is considered, standard deviation of SFD can be calculated as[87]:

$$\sigma^K_{SFD} = \sigma^K_{SFD}(0K)\left[1 - S\sqrt{\frac{(ln(tf_0)}{\beta}}\right] \tag{4.12}$$

with the t and β defined in 2.20. S depends on the input anisotropy distribution [87]. σ^K_{SFD} decreases with temperature similarly to the coercivity (eq. 2.20). This allows extrapolating the results at quasi-static (100s) conditions (e.g. VSM measurements) to recording conditions (nanoseconds or lower).

This relatively simple physical picture becomes complicated by interparticle interactions leading to correlated switching of magnetic grains, when the intrinsic switching thresholds of individual grains can no longer be resolved, leading to an extrinsic SFD. In any experimental measurements, the interactions are always present and a direct measurement of the intrinsic SFD is not possible. The measurements will give an extrinsic SFD ($eSFD$), which includes the contributions from interaction effects. Evaluating the intrinsic SFD of a magnetic recording system is an essential tool for developing and optimising the present-day and future magnetic recording technology. In this chapter the extrinsic SFD is studied and different methods of extracting the intrinsic SFD from the extrinsic SFD (or measurements) are investigated in chapters 5 and 6.

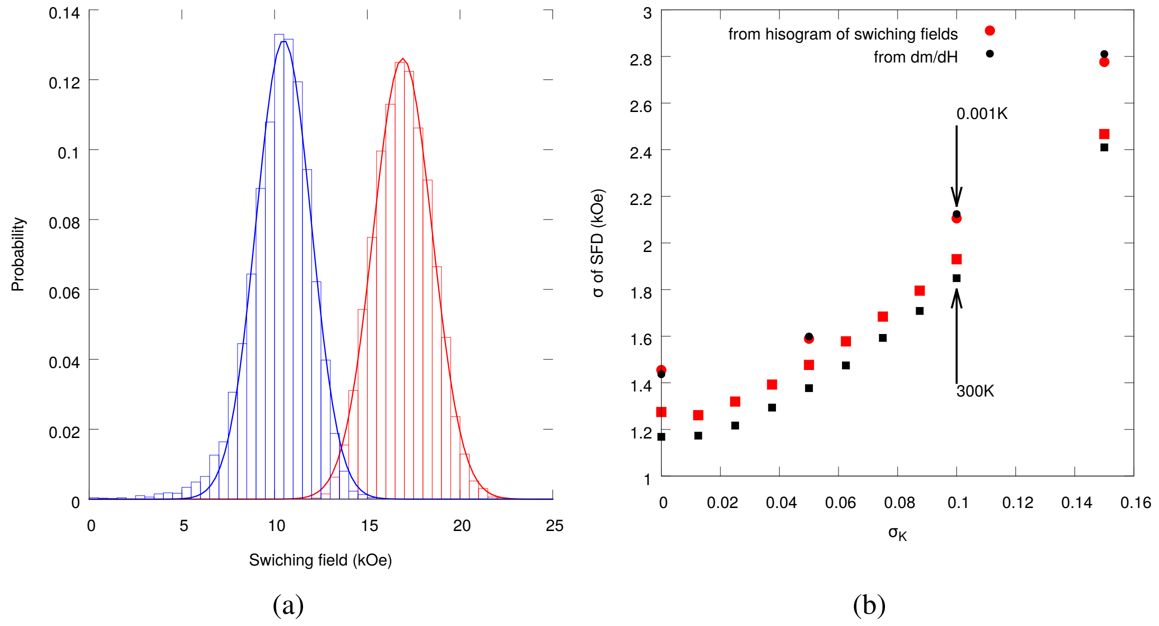

(a) (b)

Fig. 4.16 (a) Example of SFD extracted using histogram of individual particle switching field at 0.001K (red) and 300K (blue). The results are fitted with a Gaussian distribution (continuous line). The standard deviation is plotted in (b) as function of σ_K from the histogram method (red) and derivative of hysteresis loop (black).

Assuming SW particles at 0K, the switching field of an individual grain depends on anisotropy field and the angle between easy axis and field direction. In the presence of temperature, the Neel relaxation time introduces a volume dependence via the energy barriers.

For PMR media, where the hysteresis loop for each grain is approximately rectangular, the variation in magnetisation is dominated by irreversible switching events and the SFD can be extracted by the derivative of magnetisation with respect to the field during the hysteresis loop. The approach fails for large angle between easy axis and applied field and for interaction conditions. In the model, we have direct access to each grain and the SFD can be determined by calculating the histogram of the switching field of each grain. Here the switching field is considered the first applied field value at which the particle switches between states. The switching field are extracted for the system saturated in a larger positive field, during the reversal towards a larger negative field.

In figure 4.16, the SFD is illustrated for the non-interacting case at 0.01K and 300K. In the non interacting case the iSFD and eSFD are coinciding. The width of the SFD is given in figure 4.16b from histogram method and from the derivative of hysteresis loop for different σ_K. The difference between the methods is due to 3°easy axis dispersion, which introduces a small reversible component to the hysteresis loop and respectively to the derivative dm/dH. The width of SFD decreases with increasing temperature. This is consistent with the equation 4.12 from reference [87]. Calculating the SFD using the derivative of the hysteresis loop is limited to easy axis aligned with the field direction and the non-interacting case.

The extrinsic switching field distribution for the interacting case will strongly depend on the angle of the applied field. Besides the switching events due to thermal fluctuation and the switching at the critical field, interactions create an extra switching contribution. This switching appears due to the rotation of the effective field acting on each particle, which changes the energy barrier due to change of the angle between easy axis and the effective field. Also the change in the magnitude of the effective field acting on the particle is important. In extreme case, the rotation of the effective field can lead to multiple switching events by crossing the critical fields corresponding to different angle of applied (or effective) field. Next we consider the case of the field applied on the Z-direction. Results on eSFD considering angle variation of the external field are discuss briefly in the appendix A.

To extract the eSFD for the interacting case, the system is saturated in large positive field. During the hysteresis loop, the switching field corresponds to the first value of applied field in which the grain magnetisation switches between the two stable states. The mean and width of the eSFD is calculated as:

$$<SFD>=\frac{1}{N}|\sum_{i}^{N} H_s^i| \tag{4.13}$$

$$\sigma_{SFD}=\sqrt{\frac{(H_s^i-<SFD>)^2}{N-1}} \tag{4.14}$$

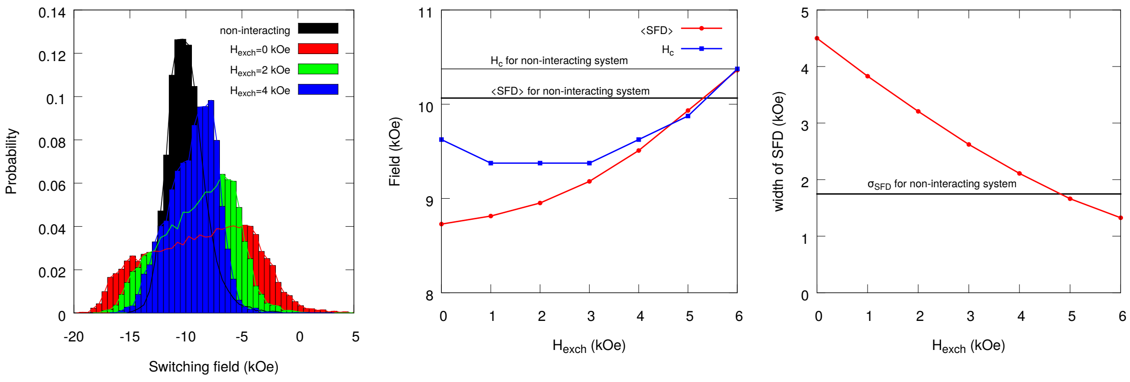

(a) (b) (c)

Fig. 4.17 (a) SFD obtained by histogram of the applied field corresponding to the first switching of each particle. The average SFD and the coercivity as function of exchange interaction (b). (c) The width of SFD as function of exchange interaction. The value for the non-interacting system are included (with black) for comparison.

where H_s^i is the switching field of grain i and the symbol $||$ corresponds to the absolute value. The SFD of a non-interacting sample is compared with the interacting case considering 3 value of exchange field: 0 kOe, 2 kOe and 4 kOe (fig. 4.17a). The average SFD ($< SFD >$) and the coercivity are given in figure 4.17b and the width of SFD (σ_{SFD}) is in 4.17c.

The non-interacting <SFD> is approximately 10.0kOe for the applied field in the easy axis direction and the corresponding coercivity is 10.4kOe. Including magnetostatic interaction of 4.6kOe ($H_{exch} = 0kOe$ in figure 4.17b) leads to a lower value of bot the average SFD and the coercivity. The exchange interaction compensates the effect, increasing the <SFD> towards the non-interacting case and having a larger value for exchange field of 6kOe. The interaction effects are less significant for coercivity, as there is weaker variation of H_c between different interaction conditions. Overall the <SFD> and coercivity are within 25% of the non-interacting case. The width of the SFD (4.17c) has a stronger variation with the exchange interaction. The magnetostatic interaction leads to an increase of σ_{SFD} by a factor of 2.5. With increasing exchange interaction the width of SFD decreases as expected. To further study the effect of interaction on eSFD, three case are selected: $H_{exch} = 0.0kOe$, $H_{exch} = 2.0kOe$ and $H_{exch} = 4.0kOe$.

The switching field distribution depends on the energy barrier (described in chapter 2) [46]:

$$Eb = \frac{KV}{k_bT}(1 + \frac{H_{eff}}{H_{cr}(\varphi)})^{(0.86+1.14g(\varphi))} \tag{4.15}$$

where φ is the angle between easy axis and the applied field. In a first approximation, the effects of easy axis orientation distribution can be neglected for a dispersion of orientation of 3°(fig. 4.18c) and therefore ψ can be approximated with the angle between Z-direction and the applied field. There are 3 important aspects to consider: the thermal stability factor, KV/k_bT, the effective field value and the orientation of the effective field. Next we extract the thermal stability factor, and the interaction field at the switching condition for each grain. These values are plotted in figure 4.18. In figure 4.18a the thermal stability normalised to the average value is plotted as a function of the switching field. The same colour scheme as before is considered: non-interacting with black, 0kOe exchange field with red, 2kOe with green and 4kOe exchange field with blue. The Z-component of the interaction field at switching versus the switching field is given in 4.18b and the corresponding orientation of the effective field is illustrated in 4.18c.

For the external field in the Z-direction as considered here, the effective field is mainly on the Z-direction as indicated in figure 4.18c , and therefore the exponent in the energy barrier (eq. 4.15) is approximately 2. Thus, each grain switching will be determined just by KV (fig. 4.18a) and interacting field on Z-direction (fig. 4.18b). During the reversal from a larger positive applied field to a negative field, the low thermal stability grains (low

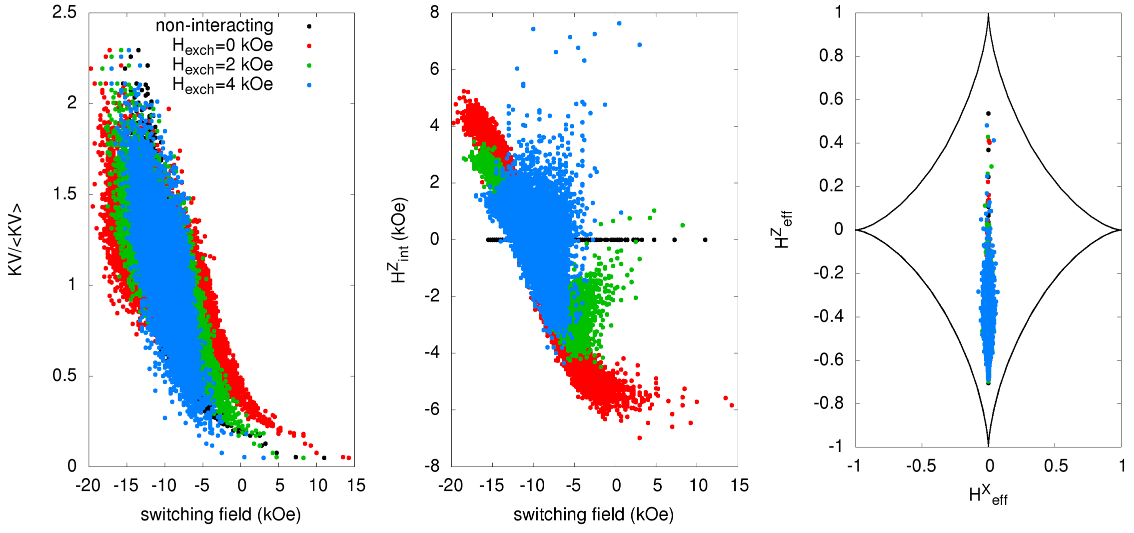

(a) (b) (c)

Fig. 4.18 Illustration of the thermal stability factor, Z-component of the interaction field and the orientation of the effective field when each grain switches for the applied field at 0°. (a) Thermal stability factor, KV/k_bT, as function of the switching field. For each grain, the interaction field is extracted at the switching field and the Z-component is given in (b). The orientation of the effective field during at the switching condition is illustrated in (c). The non-interacting system (black) is compared with 4.6kOe magnetostatic interaction and 0kOe exchange field (red), 2kOe (green) and 4kOe exchange field (blue).

KV) are switching first, if interactions are not considered. For, zero exchange field, the system behaviour is determined by the magnetostatic field (red dot in fig. 4.18) and gives rise to a large width of SFD (4.17c). The first grains that switch are in a negative interacting field ($\approx$ 5kOe fig. 4.18b), which reduces the contribution from the applied field. Thus the value of switching field is decreased. As sufficient grains switch, the magnetostatic field becomes positive and stabilises the magnetisation. In this scenario a larger negative applied field is required for the magnetisation of these grains to switch. Due to large initial negative interacting field on each grains, the switching events are more predominant at positive field as in comparison with the non-interacting case (black dots). Considering non-zero exchange interaction, the effect is balanced by the positive field from the exchange interaction. The effective interacting field (Z-component), in which the grain reverse are narrower with increasing exchange interaction strength. As a consequence the width of the SFD is also smaller as shown in figure 4.17c.

Here we show that the SFD is described by: the intrinsic properties of the grains, the amplitude of the interactions and the orientation of the effective field. For such complex case, separating the intrinsic SFD from the effective SFD is extremely difficult. The methods used to separate the intrinsic SFD from the effective SFD (e.g. FORC, ΔH) are based on rectangular shape hysteresis, which corresponds to applied field in Z-direction. In this scenario, the results presented here show that the change in the effective field orientation is minimal. Thus the SFD is described mainly by the intrinsic properties of the grains and the amplitude of the interactions. For this reason, the investigation of extracting the intrinsic SFD presented in chapters 5 and 6 are done just for the field in Z-direction.

4.4 Conclusions and Discussions

The information about collective behaviour and domain structure are important for magnetic recording media. Here the collective behaviour is described using magnetic radial correlation and surface/volume grains of a domain. The volume grains are sensitive to interaction strength and type (exchange or magnetostatic) and gives an indication if the domain are elongated (stripe type) or more symmetrical domains.

It has been shown that the zero magnetisation configuration obtained from multiple AC field cycles with decreasing amplitude, does not necessarily correspond to the system ground state. This opens a few questions: can an AC field procedure produce the configuration corresponding to the ground state of the system, and if it can, in which conditions of sweep field rate and how slowly the field amplitude needs to decrease? If not, is there any alternative procedure which consistently generates the ground state under experimental conditions?

A secondary effect of magnetic collective behaviour is discussed in the relaxation process, where a system initialised in one direction will exponentially time evolve towards the equilibrium state. This will define the thermal stability of the stored information and can be significantly altered by interactions. In a non-interacting system the process is monotonic. In zero external field, the normalised average magnetisation will decreases monotonic from 1 to 0. Here it has been shown that a non-monotonic behaviour can be observed in the presence of magnetostatic and exchange interactions. The non-monotonic behaviour arises from the magnetostatic interaction and the exchange interaction can increase or decrease the effect. The key elements can be explained using a dimer system, where two magnetic particles are coupled together via magnetostatic interaction. The system will first relax in an effective negative field. If the two individual particles relaxation processes are in well separated time scales, then the first particle will relax to the equilibrium state corresponding to the negative effective field. Afterwards the second particle relaxes as well and both particle relaxation process will evolve towards zero net magnetisation. This is observed in the PMR system considered here, where the small grains, are less thermally stable and relax much faster than the large grains. When the small grains reach zero magnetisation, there is still a large negative field from the magnetostatic interaction as the large grains did not completely evolve toward the equilibrium state. This leads to a negative magnetisation of the small grains in that effective field, which eventually disappears as the larger grains converge to equilibrium.

In the final part the hysteresis properties and switching field distribution is investigated. The intrinsic SFD is modified due to interaction effects leading to an effective SFD. The effective SFD depends not just on the individual grain properties (e.g. anisotropy, volume, easy axis orientation) but also on the local interacting field amplitude and direction. The results demonstrate that in the case of PMR system with the applied field perpendicular to the system, the change in the individual grain switching field is mainly from the local interaction strength and the effect from the orientation of the local interaction field is minimal. This is not the case if the external field is applied with a different angle.

Chapter 5

FORC method for SFD identification

5.1 Introduction

First Order Reversal curve (FORC) method is extensively applied as a tool to qualitatively capture the general aspects of a magnetic system: mixed magnetic phases[88], cluster/long-range ferromagnetic state, magnetic characterization of geological mixtures minerals and different magnetization reversal mechanisms [89–91]. The method is also used as a quantitative approach for determination of intrinsic switching field distributions (SFD), and interaction field distribution (IFD) in magnetic systems with hysteresis, such as in recording media [92–94].

The attractiveness of the FORC method is in its simplicity and its straightforward applications to a wide range of systems displaying hysteresis. The correct SFD identification of the FORC based techniques originate in the work of Mayergoyz [95, 96]. He mathematically proved that for any hysteresis system (magnetic or non-magnetic) that satisfies the Preisach model condition, the input SFD (or the equivalent quantity for non-magnetic system) can be accurately re-obtained using the FORC method. There are two condition for a Preisach system, wiping-out and congruency, which will be discussed in the next section[95, 97].

Experimentally is hard to produce samples that satisfy the Preisach conditions. However, FORC methods are applied more generally and used widely for quantitative analysis, such as the determination of the SFD. Presently, the accuracy in determining the SFD quantitatively is under intensive critical discussions [98, 99]. The FORC method is decoupled from the restrictions of a Preisach system and can be applied to any system. Consequently, given the importance of the SFD in magnetic recording, it is imperative to establish the range of validity and applicability of the Preisach analysis of FORC data and to consider more advanced techniques.

In this chapter it is described how well the FORC method can evaluate the SFD of a recording magnetic system for different levels of the magnetic system complexity, from the simple Preisach model to the more realistic strongly interacting granular system present in current recording devices. In the end of the chapter a validity diagram of the method is presented.

5.2 Preisach model: The basics of the FORC method.

The Preisach model is the most simplified mathematical description of a magnetic system. The main entity of this mathematical construction is a rectangular hysteresis loop (RHL) referred to as a hysteron (fig. 5.1a). Each hysteron is characterized by a coercivity field (H_c) and a shift field (H_u) or by a switching field from positive to negative magnetization (H_b) and from negative to positive magnetization (H_a). The link between the two pairs is given by the following equations:

$$H_a = (H_u + H_c)/2 \tag{5.1}$$

$$H_b = (H_u - H_c)/2 \tag{5.2}$$

In the Preisach model, H_b is also known as the negative switching field and H_a as positive switching field.

If we consider a system containing an ensemble of hysterons, based on the Preisach model, the system behaviour will be described by two distributions: firstly that of the coercivity field D(H_c) and secondly that of the shift field D(H_u) or by the two equivalent distributions D(H_b) and D(H_a). To access these distributions Mayergoyz, suggested measuring a sequence of first order reversal curves starting at different H_b. In this way you access part of the D(H_b) and D(H_a) distribution. He expressed this in terms of FORC distribution by:

$$\rho_{ab}(H_a, H_b) = -\frac{1}{2}\frac{1}{M_s}\frac{\partial^2 M(H_a, H_b)}{\partial H_a \partial H_b} \tag{5.3}$$

Figure 5.1(b) illustrates the measurement protocol used to generate the FORC data. The starting point is the saturation of the sample by applying a large positive field. The field is then decreased towards the reversal field, H_b, after which the field direction is reversed and increased from H_b back to positive saturation. This process generates a FORC curve attached to the major hysteresis loop at the reversal point H_b (red line in Fig. 5.1(b)). The magnetisation point at an applied field $H_a > H_b$ along this FORC, denoted as $M(H_a, H_b)$, is internal to the major hysteresis loop. As illustrated in Fig. 5.1(b), at any value of H_a in the

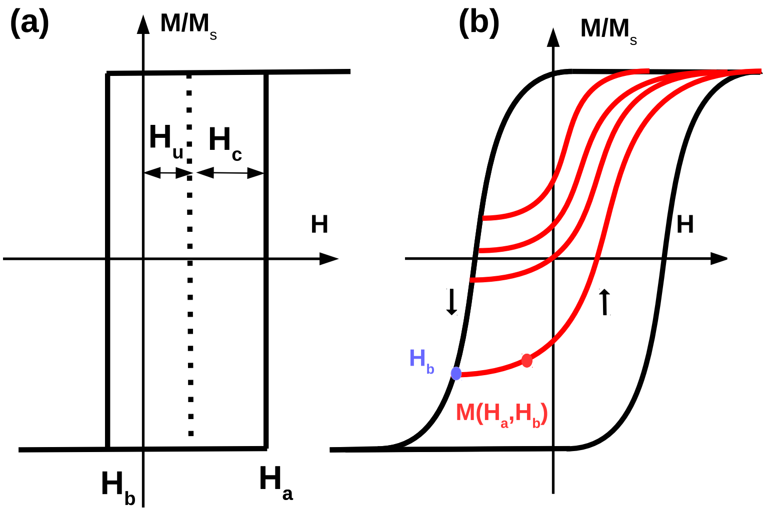

Fig. 5.1 The ideal single particle hysteresis loop has a rectangular shape corresponding to the hysteron model (a), where the only change in magnetization is due to switching events. (b) The hysteresis loop of a distribution of hysterons and example of first order reversal curves.

hysteresis region, there is an entire family of such internal magnetisation points $M(H_a,H_b)$ distinguished by the reversal field H_b of their corresponding FORCs. The FORC data are then analysed by computing the numerical second-order derivative of the functional dependence $M(H_a,H_b)$ with respect to the applied field H_a and H_b (eq. 5.3). It is conventional to transform ρ_{ab} to depend on H_c and H_u based on eq. 5.1-5.2, which leads to the FORC distribution represented as:

$$\rho_{ab}(H_a,H_b) = \rho_{ab}(H_a(H_c,H_u),H_b(H_c,H_u)) \equiv \rho(H_c,H_u) \tag{5.4}$$

For the Preisach system the FORC distribution is the product between the coercivity distribution and the shift field distribution:

$$\rho(H_c,H_u) = C \cdot D(H_c) \cdot D(H_u) \tag{5.5}$$

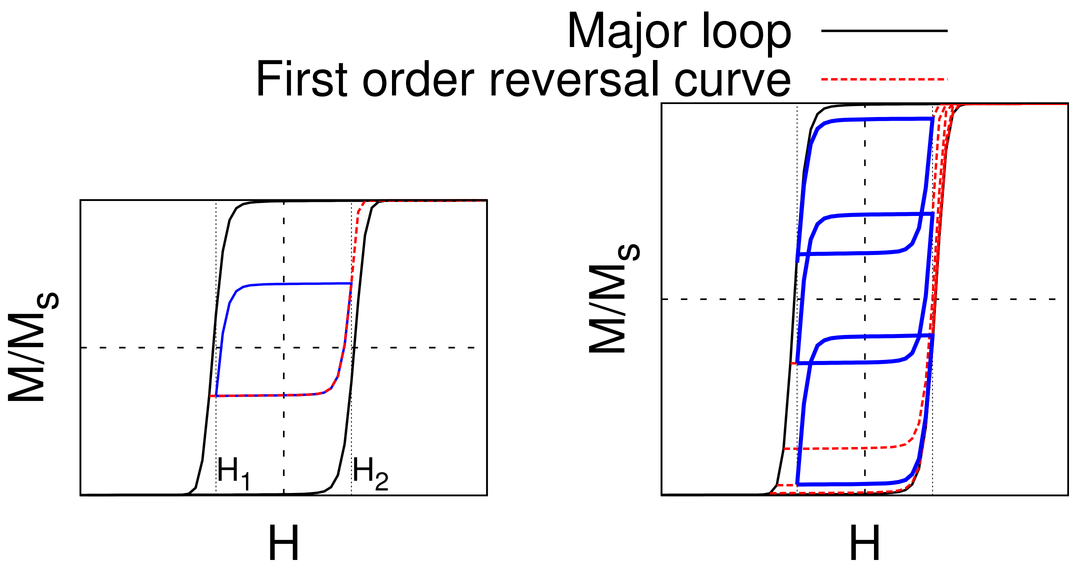

Fig. 5.2 Example of hysteresis loops for a system of hysteron showing the wiping-out condition (a) and the congruency condition (b).

where C is a normalization factor. From eq. 5.5, the SFD can be obtained by a straightforward integration over the variable H_u [100]:

$$\rho_{SFD}(H_c) = D(H_c) = \int_{-\infty}^{\infty} \rho(H_c, H_u)\, dH_u \tag{5.6}$$

For a Preisach description, the system must satisfy two conditions[95]:

- Wiping-out conditions which essentially means that the minor loops are closed. If we consider a minor loop between two fields H_2,H_1, going from H_2 to H_1 and then back from H_1 to H_2, the same magnetic moment configuration is reobtained at H_2 (fig. 5.2(a)). This means that each point is uniquely characterized by the magnetization value M and the applied field, independently of the field sequence leading to that specific magnetization.

- Congruency condition states that all minor loops obtained between the same fields, but started at different states are congruent. Essentially all the minor loops between the same two fields are the same size and shape (fig. 5.2(b)).

Equations 5.4, 5.5, 5.6, illustrate how the SFD can be obtained from mapping the individual grain switching field in positive and negative field (H_b, H_a) using FORC curves. This is referred to as the Preisach interpretation of the FORC method.

5.3 FORC method

Unfortunately, the straightforward interpretation as given above does not apply in realistic cases when the particles are represented by non-ideal RHLs, the inter-particle interactions are relevant, or in the presence of thermal fluctuations.

General systems with hysteresis do not always display the wiping-out and congruency properties. The later work of Pike et al. [1999], suggested that the FORC method should be applicable for any system, even if the system does not correspond to the Preisach condition. In this case the accuracy and uniqueness of the identification of SFD from the FORC distributions needs to be established with respect to the relevant physical picture and by independent measurement methodologies. Following Pike et.al. [92] we make the distinction between the raw FORC data, the FORC diagram and the usual interpretation of the FORC data based on the Preisach model, which uniquely links the FORC diagram to the SFD and interaction field distribution of the model.

The FORC method has two main steps. The first one consists of obtaining the first order reversal curves(FORC data) and creating the FORC diagram. In the second part, the FORC diagram is modified such that the undesirable contribution of the inter-particle interaction is removed. The latter is not always possible without losing accuracy in the SFD. To extract the SFD from the FORC data, a matlab code provided by Seagate was used [101]. The code is similar to the implementation used in the commercial FORCinel software [102]. The raw FORC data are mapped to a rectangular grid with each point fitted using 2-dimensional polynomial fit, based on the Locally Weighted Polynomial Regression Method. Each point on the grid is calculated depending on the neighbouring points weighted by the distance to the grid point:

$$w_i = \left(1 - \left[\frac{d_{ij}}{max(d_{ij})}\right]^3\right)^3 \tag{5.7}$$

where d_{ij} is the distance between the grid point 'i' and the neighbouring points from the FORC data 'j'. This method has the advantage that it does not require the FORC data to be at equidistant values of H_a and H_b. To extract the SFD, first the non-interacting FORC diagram needs to be obtained. This is done by modifying the (H_a, H_b) diagram to ($H_a^* = H_a - \alpha m(H_a)$, $H_b^* - \alpha m(H_b)$), where α is a mean field correction factor [93, 103]. During this process, the original (H_a,H_b) grid is distorted and the Locally Weighted Polynomial Regression Method is important to take into account this and maintain the original grid. α is varied to satisfy two conditions: 1) the FORC diagram is symmetric with respect to the second bisector in (H_a,H_b) plane (equivalent to symmetry around H_u=0 in (H_u,H_c) plane) [93, 104] and 2) the

FORC diagram, being a distribution of interaction and switching fields, can not have negative values. When these two conditions are satisfied, the SFD can be extracted by projecting the corrected FORC diagram on the H_c axis. H_u is interpreted as an interaction field, even if this is not always the case. A non-zero value of H_u can occur in the absence of interaction, if the magnetic system has reversible component (non-aligned easy axis as discussed in the next section figure 5.4) or thermal effects are considered.

In the simplest case of an assembly of bistable magnetic particles magnetically aligned along the direction of an external magnetic field (as for example the hysteron model illustrated in figure 5.1(a) in the absence of inter-particle interactions, the macroscopic hysteresis loop is simply a superposition of the projections of the magnetic moments of the particles onto the field direction ordered according to the switching events of individual particles. The FORC diagram is a straight line $\rho(H_c,H_u) = \rho^*(H_c)\delta(H_u)$. Then the SFD can be determined by a straightforward application of equation 5.6, which makes the FORC-method an inherently accurate technique for its identification. The problem is complicated for three main reasons, which are studied in detail in the next section:

1. Non-rectangular hysteresis loops of single particles.
2. Thermal relaxation phenomenon introducing the dependence of the measurement outcome on the measurement time scale, such as the rate of variation of the external field.
3. Inter-particle interactions: Inter-granular exchange and magnetostatic interactions produce partially correlated magnetization reversal, essentially wiping out information about the individual nature of grains from the magnetization measurement. The switching threshold of individual grains then contains a component from neighbouring grains, which is hard to separate from its own intrinsic threshold.

In the next sections the original FORC diagram with no corrections for interactions are illustrated and the characterisation of SFD is done after the corrections to remove the interaction is done.

5.4 Model of non-interacting grains

Here we consider PMR as described in table 2.1. The system consist of elongated grains with an aspect ratio (h/d) of 1.17, uniaxial anisotropy (K) with mean value of $7 \cdot 10^6$ erg/cm^3 and 3 degree dispersion of the anisotropy easy axis around the perpendicular direction to the grain plane. The grain height (h) is 10 nm, the mean grain size (grain diameter) (d) is

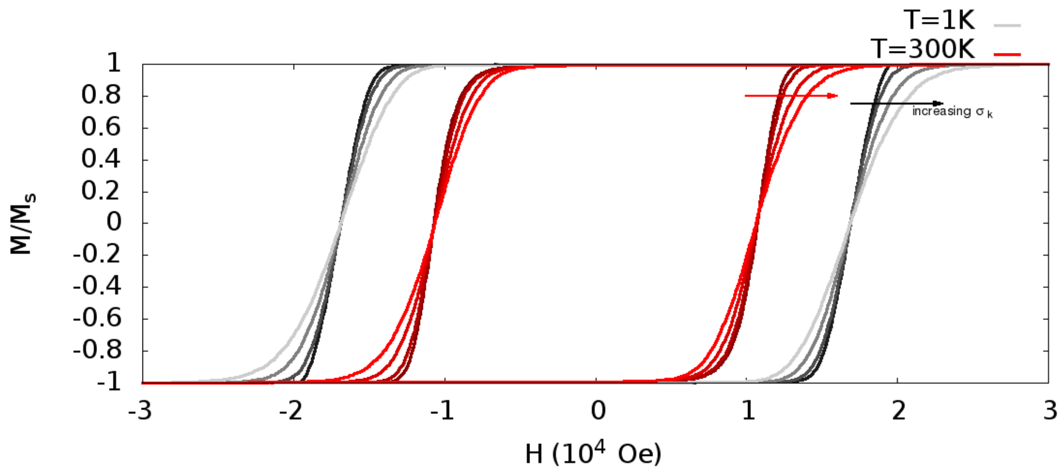

Fig. 5.3 Hysteresis loop for non-interacting system of recording media at 1K (gray colors) and 300K (red colors) for 4 value of σ_k=0.0,0.05,0.1,0.15.

8.5 nm and the saturation magnetization (M_s) is 700 emu/cm^3. The calculations assume an external field rate of $4 \cdot 10^4$ Oe/s at room temperature (300K). For all the results presented here, between 50 and 60 FORC curves are used with a field step of maximum 100 Oe.

Non-interacting, non-aligned easy axis

First we will consider the non-interacting case, where each grain will have a non-RHL due dispersion of easy axis and temperature effects. Hysteresis curves for 4 values of σ_K (0.0,0.05,0.1 and 0.15) are simulated (figure 5.3), together with the reversal curves at 1K and 300K. The 300K corresponds to the typical recording media measurements and the 1K data are essentially athermal. In figure 5.4 the FORC diagram of the system at 1K and 300K are shown. Deviation from the Preisach model can be observed even in the non-interacting case. The reversible components in the hysteresis loop lead to non-zero values on the H_u axis. This is in reality not an interaction field, but rather errors from the FORC method in interpreting the reversible components. Also, on the basis of the Preisach model the FORC diagram should be perfectly symmetric around the H_u axis, which is not the case in experiments or in our calculation. This is due to the fact that the thermal effects are proportional to the coercivity field.

Fig. 5.4 shows that the FORC distribution ρ is no-longer a straight line $\rho(H_c,H_u) = \rho^*(H_c)\delta(H_u)$ as in the case of a system of ideal non-interacting particles with RHLs discussed above, and instead has a significant H_u component even if the inter-particle interactions are absent. This is due to the particle hysteresis loop rounding, when the change of magnetization

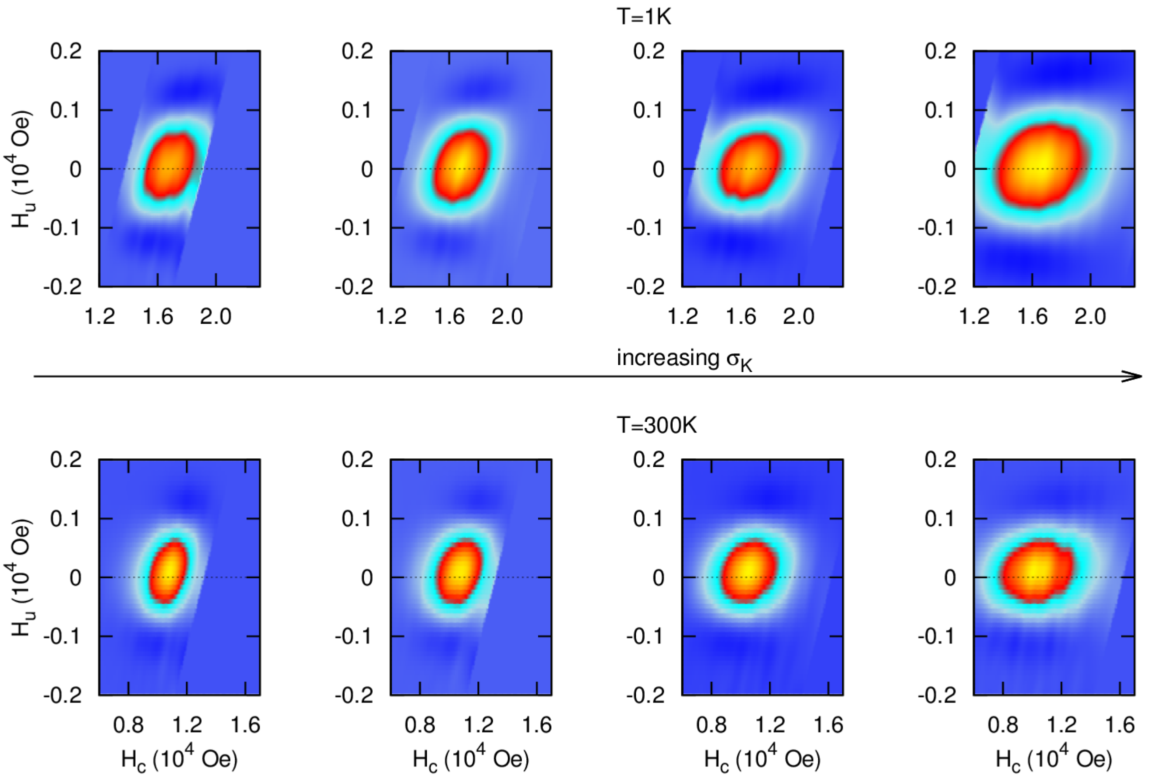

Fig. 5.4 FORC diagram for non-interacting case at 1K top row and 300K bottom row for 4 values of σ_k=0.0, 0.05, 0.1, 0.15.

along the macroscopic loop no longer occurs only at the switching thresholds of particles, as in the ideal RHL case, but in addition includes a smooth nonlinear component from the rounding effect. The 1K data illustrated in the top of figure 5.4 is a good approximation of non-thermal hysteresis loops as the thermal stability factor, KV/k_bT, is 28771. The similarity of the FORC diagram between the non-thermal (T=1K) and the room temperature (T=300K) FORC diagrams (fig. 5.4), with the exception of the shift of the distribution on H_c axis, indicates that the main source of errors are not the thermal effect, but the misalignment of the easy axis.

Nevertheless the FORC method correctly recovers the SFD and, within the resolution of the method, zero interaction field. In the non-interacting case, the SFD can be directly extracted from the projection of the FORC distribution on the H_c axis, equivalent to computing eq. 5.6. In 5.5 and 5.6 the mean value of SFD and σ_{SFD} is correctly obtained from the FORC method, with the note that no correction for interaction fields was done. The expected value is obtained directly from the histogram of computational data of each grain switching

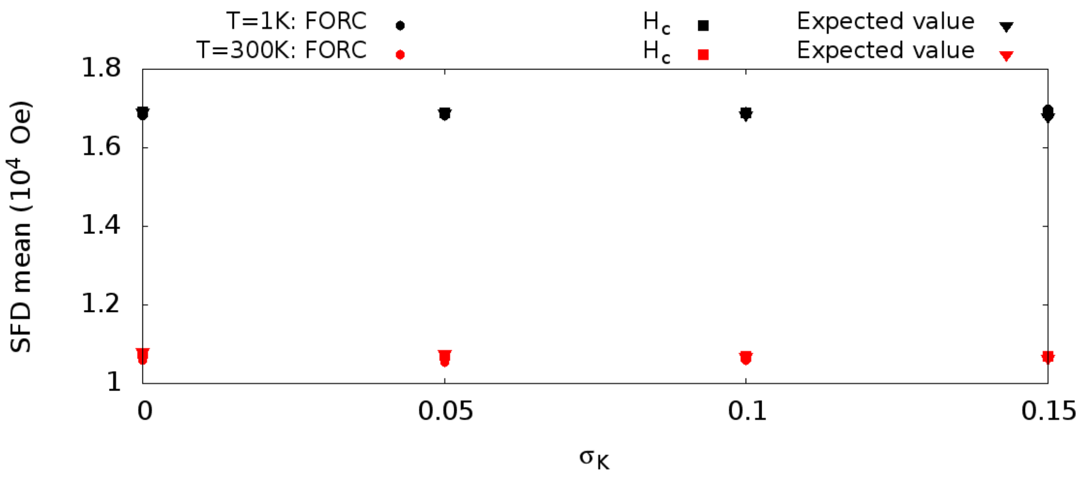

Fig. 5.5 Mean value of the SFD as function of σ_K at 1K (black) and 300K (red).

field. Both mean SFD and σ_{SFD} are lower at 300K in comparison with 1K as an effect of decreasing of coercivity field with temperature.

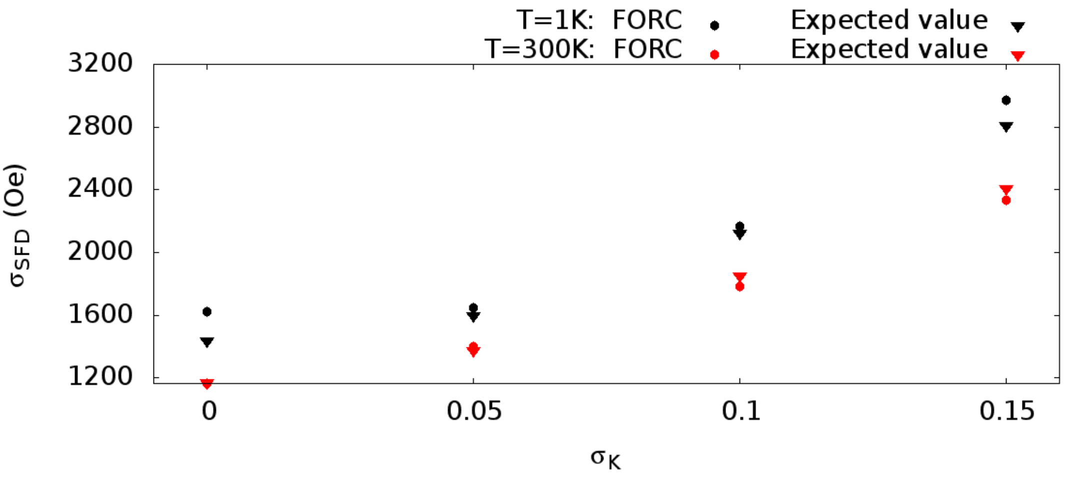

Fig. 5.6 σ_{SFD} as function of σ_K from FORC method (circle) and the expected value (triangle) at 1K (black) and 300K (red).

Thermal effects have a small impact on the broadening of the FORC distribution around the H_u axis for the recording media system. For soft material like iron-oxides with low thermal stability, even the thermal effects have strong impact on the accuracy of FORC method, but this aspect will not be discussed here. To ensure that the field step will not effect the results, a field step of 100 Oe will be used in the following calculation. This field step is one order of magnitude smaller then the broadening of the fictitious interaction field produced by the misalignment of easy axes.

5.5 Models of interacting grains

The recording media system is a densely packed configuration of grains, leading to both long range magnetostatic interaction and short range exchange interaction. The system energy is given by:

$$E = \sum_i K_i V_i (\hat{k}_i \times \hat{m}_i)^2 - \sum_i M_s V_i \hat{m}_i \cdot \vec{H}_{ap} - \frac{1}{2} \sum_{nn\, i \neq j} E^{ij}_{exch} - \frac{1}{2} \sum_{i \neq j} E^{ij}_{mag} \tag{5.8}$$

The third term in Eq. (5.8) describes the exchange interaction between the nearest neighbour grains. The last term in Eq. (5.8) represents the magneto-static interaction between the grains and is represented as $E^{ij}_{mag} = M_s V_i \hat{m}_i \cdot H^{ij}_{mag}$. The evaluation of H^{ij}_{mag} is done by integration over the surface charges. The average magnetostatic field is 4.6 kOe, almost half of the coercivity field at 300K (10.4 kOe). The FORC method is applied for a set of exchange field amplitude (0-6kOe) and anisotropy distribution dispersion(σ_K= 0-0.15). The expected values are obtained from the same system in the non-interacting condition. The results are summaries in figure 5.7. For all the values of exchange and σ_K, the obtained SFD is underestimated by the FORC method.

The inaccuracy of the FORC method can not be explained from the thermal fluctuations and misalignment of easy axis as these effects for the same system were investigated and discussed in the previous section. The only possibility is the presence of interparticle interactions. In the literature, there is a large number of investigations applying the FORC method as a qualitative tool to distinguish between different types of interactions: mean-field interactions, cluster behaviour, strong interaction dominated system. In the work of Papusoi et al. [93], is discussed the ability of determining SFD and interaction field for a PMR media with low to moderate interaction strength without discussing the type of interactions. In recording media combining the nature of interaction, short range (for exchange interactions) and long range for magnetostatic interactions leads to a complex behaviour of the magnetic system.

For recording like system (large thermal stability),in the literature, there are specific features of the FORC diagram depending on the nature and type of interactions:

- Zero or very weak interactions. The FORC diagram is elongated on the H_c axis with small dispersion around the H_u axis, similar to figure 5.4.

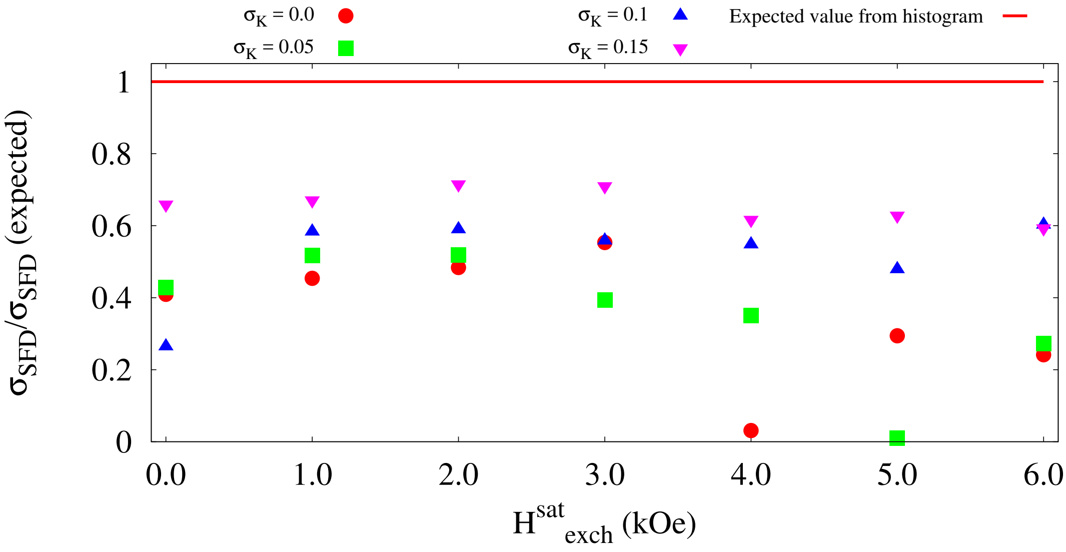

Fig. 5.7 σ_{SFD} normalized to the expected value as function of exchange field strength for 4 values of σ_K: 0.0, 0.05, 0.1, 0.15.

- Mean field interaction. FORC diagram has the typical rotated "V" or "L" shape (figure 5.9a) [105, 94].
- Positive interactions (e.g. exchange interaction with positive coupling) has the FORC distribution at low H_c shifted to negative H_u (figure 5.12) [92, 94].
- Negative interactions (e.g. exchange interaction with negative coupling or in general magnetostatic interaction) has the FORC distribution at low H_c shifted to positive H_u (figure 5.12) [92, 94].
- Strong magnetostatic/exchange interaction produce a FORC diagram with distribution along the H_u axis(5.9b) [106, 94].
- Presence of clustering or correlated behaviour produces segmentation/fragmentation of the distribution (figure 5.10) [94].

Although the type and nature of interaction can be identified using the FORC diagram, the relevant question is if the SFD can be correctly obtained in all of the above conditions. Another important aspect in addition to the amplitude of the interactions is the type of interaction. To investigate this aspect we model the same system based on equation 5.8 where interactions are exactly calculated and where interactions are mean field. For simplicity, here we consider the case without the exchange interaction. The energy expression given in

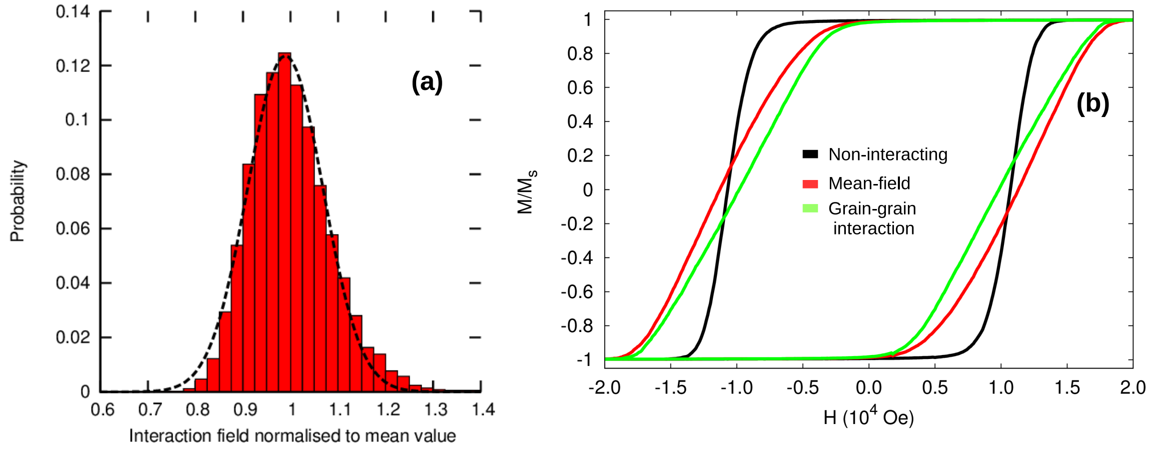

Fig. 5.8 a)Magnetostatic interaction field distribution histogram (red) at saturation normalized to the mean value (4.6kOe) and the fitting Gaussian function. b) Example of hysteresis loop for $\sigma_K = 0.05$ in non-interacting, mean field and exact interaction.

equation 5.8 is simplified to:

$$E = \sum_i K_i V_i (\hat{k}_i \times \hat{m}_i)^2 - \sum_i M_s V_i \hat{m}_i \cdot \vec{H}_{ap} - \frac{1}{2} \sum_{i \neq j} E^{ij}_{inter} \tag{5.9}$$

where the E^{ij}_{inter} is obtained from the surface integrals for the exact interaction and for mean field is given by:

$$E^{ij}_{inter} = M_s V_i H^{i}_{inter} \langle \hat{m} \rangle \cdot \hat{m}_i \tag{5.10}$$

$$\langle \hat{m} \rangle = \frac{1}{N} \sum_{i}^{N} \hat{m}_i \tag{5.11}$$

where the symbol $\langle \hat{m} \rangle$ implies averaging over all grains in the system at a given applied field. H^{i}_{inter} is determined as follows by fitting to the interaction field distribution at saturation calculated using the exact interactions (equation (3.8)). We found that a Gaussian distribution represents well the distribution of interaction fields in the exact interaction approach at positive saturation (figure 5.8). This allows us to calibrate the mean-field interaction strength to be consistent with the exact interaction model at saturation, which is used as a reference. H^{i}_{inter} is the random interaction field given by a Gaussian distribution with mean $\langle H_{inter} \rangle$ and standard deviation σ_{inter}:

$$H^{i}_{inter} = \langle H_{inter} \rangle G(1, \sigma_{H_{inter}}) \tag{5.12}$$

The magnetostatic field distribution obtained from the exact interaction model and the corresponding Gaussian function for the mean field approach are illustrated in figure 5.8(a).

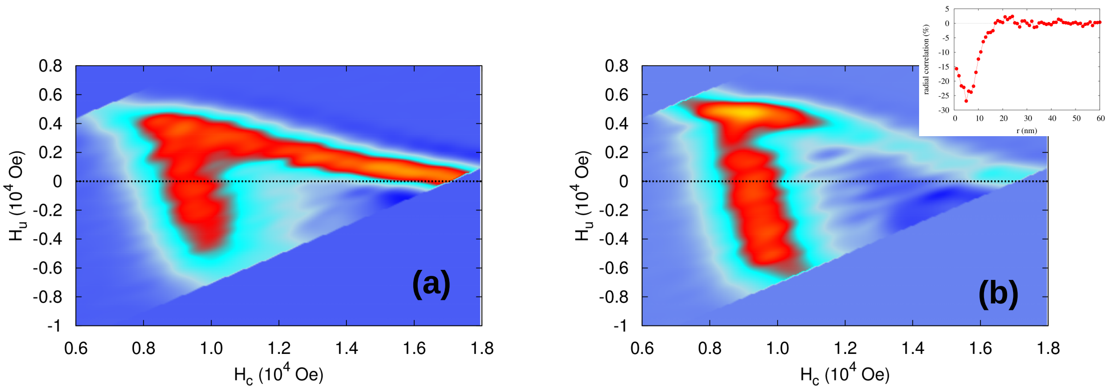

Fig. 5.9 FORC diagram with no correction for interactions: (a) mean field interaction and (b) exact interaction. The radial magnetic correlation at coercivity is given in the inset.

The corresponding hysteresis loops are shown in figure 5.8(b). At a macroscopic level, analysing the average behaviour of the system in terms of hysteresis loop (figure 5.8(b)) there is not a large difference between the two approaches for taking into account interactions. If we analyse microscopically, the behaviour of each grain, which is given by the densely FORC diagram (figure 5.9) and by the radial magnetic correlation, there are significant difference in term of correlating behaviour of the grains. Using Preisach analysis, the width of SFD,σ_{SFD}, is correctly re-obtained for the mean field case, but not for the exact interaction. The FORC diagrams (figure 5.9 illustrates how important is the approach for including interactions. Also the radial magnetic correlation function is calculated for the system at coercivity. The radial magnetic correlation is defined in section 4.1.2. If interactions are treated as mean field as in figure 5.9(a), the FORC diagram has the typical rotated "V" or "L" shape and there is no correlation between grains. In this case, the effect of interaction can be removed and the FORC method successfully computes the correct SFD. For exact interaction example illustrated in figure 5.9(b), the σ_{SFD} is underestimated by 60%. The most significant difference between the mean-field and exact treatment of the interactions is the prospect of magnetic correlations, which are not included in the Preisach model interpretation of the FORC curves. The radial magnetization correlation function, illustrated as an inset in Fig. 5.9(b) shows correlation between nearest neighbours, producing partially correlated magnetization reversal, essentially wiping out information about the individual nature of grains from the magnetization measurement. The switching threshold of individual grains then contains a component from neighbouring grains. For this type of system, the FORC diagram is stretched along the H_u axis, suggesting that the reversal process is dominated by interaction, thus masking the intrinsic properties of the system. Thus we hypothesize that spatial magnetic correlations distort the Preisach model interpretation, leading to the failure to deconvolute the SFD and interaction effects.

The mean field approach is a first order approximation of an interacting system. For many applications the magnetic nanostructures are close packed, such as granular media for HDD, leading to stronger interaction effects, beyond the mean field approach. The effect of interaction on the microscopic details of the sample, such as SFD, are given not just by the amplitude of interaction but also by the type of interaction. Interaction strength can be characterized in terms of collective behaviour, which can be quantified by the radial correlation function.

Cluster model-interacting: Correlation/Collective behaviour

We hypothesize that spatial magnetic correlations distort the Preisach model interpretation, leading to the failure to deconvolute the SFD and interaction effects. To validate the above statement for a general system we adapt the kMC model to a 'toy model' in which the correlated behaviour is artificially included.

For the exact magnetostatic interaction model the correlation between the grain varies as a function of the applied field and clusters with different shape and size are formed. To simplify the problem, in the 'toy model', grains are arbitrarily grouped in clusters of same size with N_g grains. The clusters are not coupled with each other and the system energy will obey the following equation:

$$E = \sum_i K_i V_i (\hat{k}_i \times \hat{m}_i)^2 - \sum_i M_s V_i \hat{m}_i \cdot \vec{H}_{ap} - \sum_j E^j_{cluster} \tag{5.13}$$

The interaction energy per cluster is defined as:

$$E^j_{cluster} = \sum_i^{N_g} M_s V_i H^i_{inter} \langle \hat{m} \rangle_j \cdot \hat{m}_i \tag{5.14}$$

$$\langle \hat{m} \rangle_j = \frac{1}{N_g} \sum_i^{N_g} \hat{m}_i \tag{5.15}$$

similar to the mean field approach. The interaction field will depend on the average magnetization of a cluster of grains with the interaction amplitude H^i_{inter} obtained from the Gaussian distribution eq. 5.12.

If in equation 5.14 the average cluster magnetization, $\langle\hat{m}\rangle_j$, is explicitly written, the equation can be written as:

$$\sum_i^j M_s V_i H^i_{inter} \langle\hat{m}\rangle_j \cdot \hat{m}_i = \sum_i^{N_g} \left[M_s V_i H^i_{inter} \hat{m}_i \cdot \frac{1}{N_g} \left(\sum_l^j \hat{m}_l \right) \right] \tag{5.16}$$

$$\sum_i^j M_s V_i H^i_{inter} \langle\hat{m}\rangle_j \cdot \hat{m}_i = \sum_i^{N_g} \sum_l^{N_g} [J_i \hat{m}_i \cdot \hat{m}_l] \tag{5.17}$$

where

$$J_i = \frac{M_s V_i H^i_{inter}}{N_g} \tag{5.18}$$

$$\sum_i^j M_s V_i H^i_{inter} \langle\hat{m}\rangle_j \cdot \hat{m}_i = \sum_i^{N_g} \sum_{l,l\neq i}^{N_g} [J_i \hat{m}_i \cdot \hat{m}_l] + \sum_i^{N_g} [J_i \hat{m}_i \cdot \hat{m}_i] \tag{5.19}$$

where the second term is a constant value. Equation 5.19 can be applied for any type of interaction, with J_i being either an exchange or magnetostatic coupling factor. A similar approach is used by Gilbert et al [94], where analogous segmentation effects have been studied in terms of a nearest neighbour grain interaction model. Using equation 5.14 we control the degree of correlation in the system, which is inversely proportional to N_g. If the number of grains per cluster is small the system will be strongly correlated as a change in magnetization in one grain will produce a large local field variation acting on the rest of the cluster, whereas the rest of the system is unaffected. For the other extreme, large number of grains per cluster, the system will be uncorrelated, obtaining the mean field model. The amplitude of interaction at saturation is maintained the same as the exact interaction calculation presented in the previous section.

This toy model, gives the possibility to explore the effects of correlation in a general system, as the interaction strength is always the same and just the degree of correlation is systematically varied. The uncorrected FORC diagrams for cluster size of 4 5 10 and 100 grains are illustrated in figure 5.10. For large cluster size (N_g=100), the 'toy model', reproduces the mean field results: "V" shape of FORC diagram. By decreasing the cluster size, effect of collective behaviour manifests as fragmentation of the FORC diagram. At $N_g = 10$, the correlation starts to be significant and the FORC diagram shows a very weak fragmentation. As the cluster size decreases even more (N_g=4,5) the correlation between grains increases and the fragmentation of the FORC diagram is clear. The effect is due to the fact that interaction field does not vary continuously as in mean field, but discontinuously in

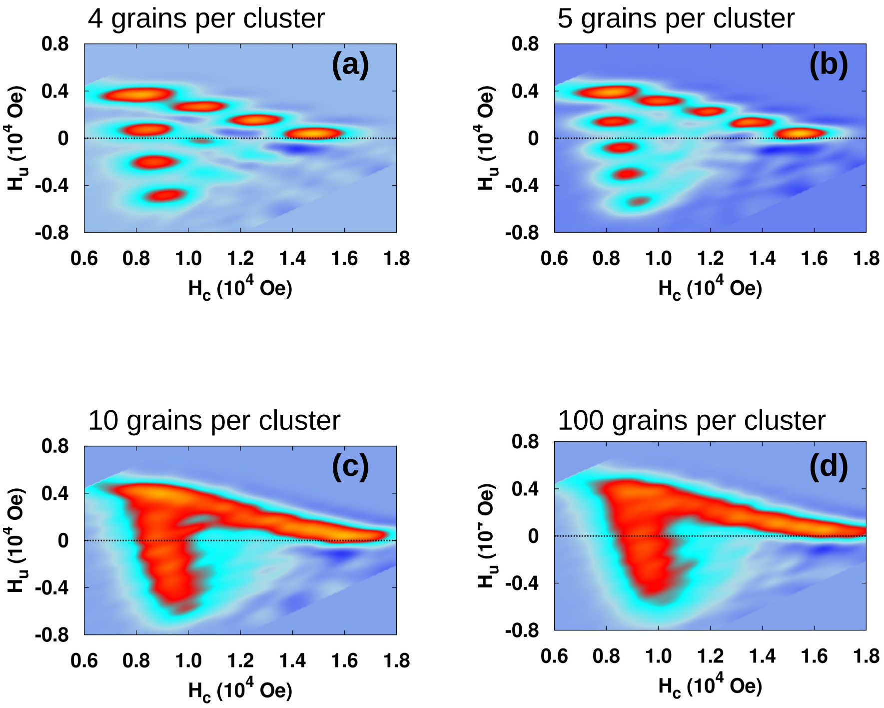

Fig. 5.10 FORC diagram for cluster size of (a) 4, (b) 5, (c) 10 and (d) 100 grains. By decreasing the cluster size the fragmentation of the FORC distribution is more pronounce as correlation inside each cluster are increasing.

quantified jumps. For example for the 4 grain cluster, the change in cluster magnetisation when one grain switches to the opposite direction is approximately $< m >_j = 0.5$, leading to a large change in the interaction field from the saturation value to 50% of that particular value, thus hiding all the switching in that field interval. A similar effect is described by Gilbert et al [94]. Although this is a toy model, the same behaviour happens when we consider nearest neighbours interaction; the switching of a grain produces a large change in the field acting on the neighbouring grains.

Next we apply the mean field correction to extract the σ_{SFD} and calculate the radial magnetic correlation function for cluster size of 4,5,10, 100, 500 grains. The results for this simplified model are given in Fig.5.11, where for comparison we also include the calculation of the exact interaction model. Firstly, the correlation results confirm that we can control

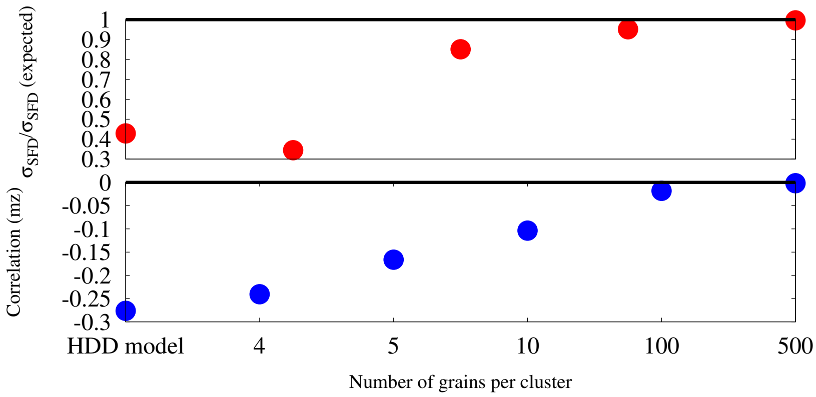

Fig. 5.11 Extracted σ_{SFD} for toy model
The width of the SFD, σ_{SFD} (red), and the radial magnetic correlation at coercivity state (blue) as function of cluster size for the toy model. The cluster size in inverse proportional with the degree of correlation in the system. The larger the cluster size the closer the model is to a mean-field-like model, which is completely uncorrelated system and FORC method can be applied successfully. By increasing the correlation, the FORC method is underestimating the σ_{SFD}.

the degree of correlation in the toy model with the number of grains per cluster (bottom graph in figure 5.11). For large cluster, the system is uncorrelated tending towards the mean field approach, whereas for decreasing cluster size the correlation are large, having similar values as in the exact interaction case. The extracted σ_{SFD} are compared to the expected values, showing a deviation from the expected value with decreasing cluster size. These results suggests that increasing the degree of correlation between grains will make the FORC method unreliable, leading to the underestimation of σ_{SFD}. Based on the toy model results we can conclude that in the systems exhibiting significant correlations, the FORC is not able to accurately determine σ_{SFD}.

Full interacting system model

Following our hypothesis discussed in the previous section, two question are of interest: 1) how strong the correlation needs to be for the Preisach analysis of the FORC method to give SFD values deviating from the expected value and 2) how large are those deviations. The answer will depend on the type of system in terms of interaction (strength and nature of interaction) and grain properties (such as anisotropy, volume, saturation magnetization, etc.). In recording media the interactions (magnetostatic and exchange) can be varied systematically, thus making the recording media system ideal for studying the two questions. The answer will depend on the type of system and here we will study the two questions for the system described at the beginning of the section, 5.4 which is important in recording media industry.

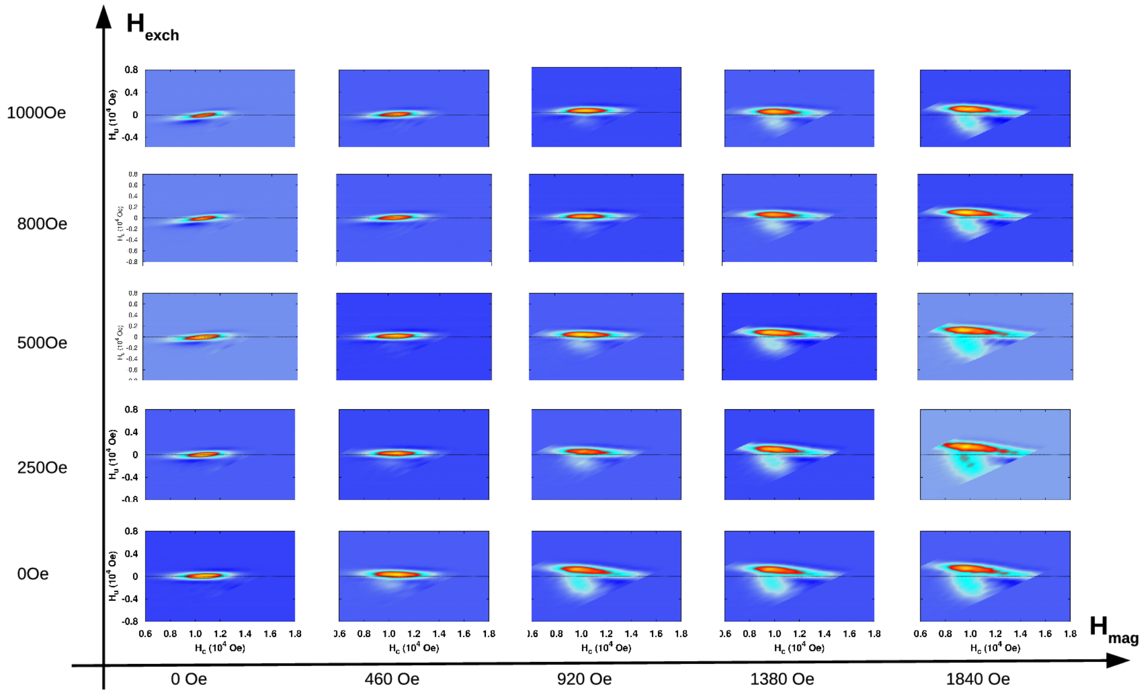

Fig. 5.12 FORC diagram before correction for different exchange and magnetostatic fields.

To investigate the interaction range where the FORC method can be used, and to further quantify the mapping between the magnetic correlations and the failure of the Preisach-based FORC analysis, we systematically vary the strength of the exchange and magnetostatic interaction and extract the σ_{SFD} from the FORC diagram. Examples of FORC diagrams are shown in figure 5.12 for different combination of exchange and magnetostatic field. The typical elements observed in experimental FORC diagrams can be observed in figure 5.12. A systematic shift of the FORC density towards smaller switching fields, the formation of a "V" shape distribution for increasing magnetostatic fields, shift of the low H_c distribution towards negative H_u for exchange fields.

Next, following the toy model results, we investigate the postulate that the errors in SFD determined from the Preisach analysis are related to the presence of correlations. First we calculate the magnetisation correlation at the coercivity. Figure 5.13 illustrated the radial correlation as function of distance for each interaction strength (just magnetostatic in (a) and just exchange in (b)). Analysing figure 5.13, we can observe that the nature of correlation also has an important role. The interactions can be either ferromagnetic, aligning

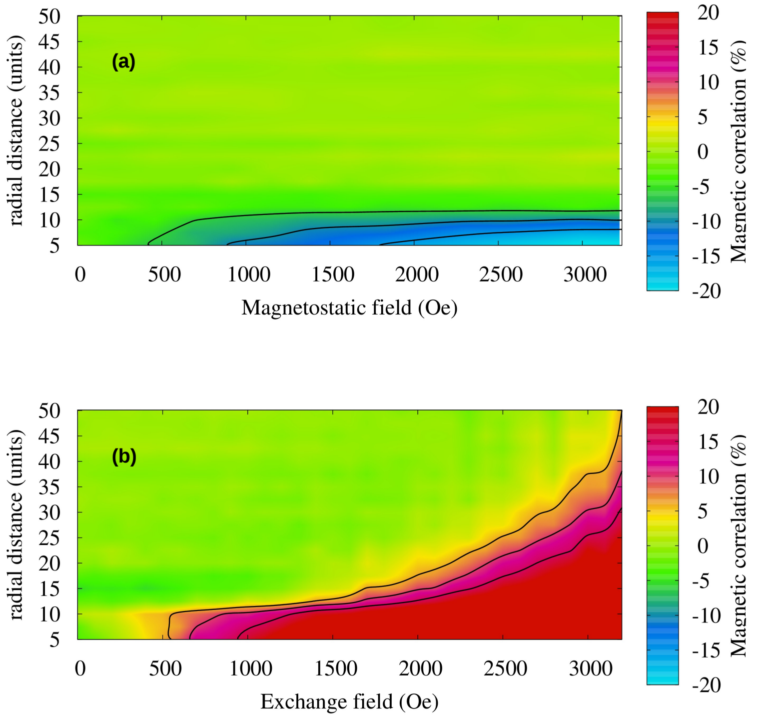

Fig. 5.13 Radial magnetic correlation for just magnetostatic interacting system (a) and just exchange interacting system (b).

the magnetic moment in the same direction, or antiferomagnetic, aligning the magnetic moments in opposite direction, leading to positive correlation and negative correlation respectively. The exchange is a short range ferromagnetic interactions, characterized by large domains and strong correlation (as seen in figure 5.13b). On the other hand the magnetostatic interactions are long ranged and can be ferromagnetic or antiferomagnetic characterized by small domains and weaker correlation as shown also in figure 5.13a. The weak correlation is due to the statistic nature of correlation function, where two grains positive correlated are statistically cancelled by 2 grains negatively correlated. This does not necessary means that the switching events of both pairs of grains are not strongly affected by the coupling between them (positively for one pair and negative for the other).

The results for all combination of exchange and magnetostatic fields are summarised in figure 5.14. Figure 5.14(a) shows the dependence of the maximum value of the correlation function in absolute value as function of the exchange and magnetostatic field magnitudes. Figure 5.14(b) shows the corresponding errors in the determination of σ_{SFD}, with the solid lines being a mapping of the correlation function from Fig. 5.14(a). The errors are calculated

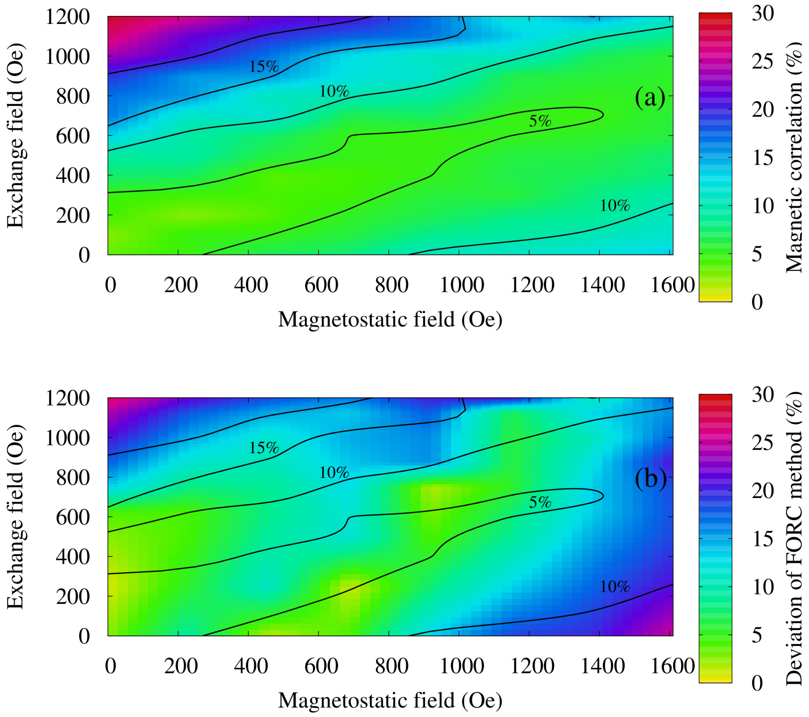

Fig. 5.14 (a) Correlation diagram: The magnetization correlation is calculated at coercivity and the maximum correlation is extracted in absolute value. As exchange and magnetostatic interaction increase the coupling between grains also increases leading to large correlation values. The values on the diagonal are minimum because positive and negative correlation, due to exchange and magnetostatic interaction, compensate overall. (b) Validity diagram: Diagram showing the deviation of σ_{SFD} from the FORC method in comparison with the expected value. The contour lines from (a) are indicate the correlations for the same interaction parameters.

as the deviation of the FORC method prediction from the expected value normalized by the latter one. Clearly a dominance of either magnetostatic or exchange interactions leads to strong correlations, with a diagonal region within which the effects essentially cancel out leading to a relatively spatially uncorrelated magnetization structure. It can be seen that the parameter space having the best determination of the SFD from the Preisach-based FORC analysis corresponds to that having weak spatial correlation of the magnetization structure. Depending on the required accuracy of determination of the SFD, Fig. 5.14(b) indicates the range of parameter space in which this can be achieved. The SFD prediction from the FORC method deviates in a systematic way by underestimating the SFD with increasing interaction strength.

5.6 Conclusion

The FORC diagram method does not rely on a certain model, thus having few constraints on the data. The method is successfully used for qualitative investigation of magnetic behaviour, considered as a fingerprint of the system. Although there is an increased interest in using the FORC method for quantitative investigation of switching field distribution (SFD) [94] and interaction field distribution, we have shown that it has limitations which need to be taken into account.

However, it is important to note that the shortcomings are associated with the Preisach-based analysis, which maps the FORC data directly onto a (H_u, H_c) plane whilst neglecting the degree of correlation in the magnetization structure. FORC data certainly contains information on the interactions and SFD, but the Preisach-based analysis cannot, in general, reliably carry out the required deconvolution of the relative contributions. The joint interaction field and switching threshold distribution obtained from Eq. 5.3, which is the basis of the FORC method, has data structure equivalent to the hysteron distribution in a broad class of Preisach models. The difference is that the interpretation of Eq. 5.3 as Preisach distribution requires that the first order magnetization reversal curves satisfy additional properties, namely the wiping-out and congruency properties[99]. These properties then guarantee uniqueness, i.e. that the identified Preisach distribution is the true and the only switching distribution associated with a given material or system[95].

It has been shown that Preisach analysis of FORC data can only be used in a limited range of conditions for quantitative investigation. The limitation is due to correlated switching in strongly interacting systems, where individual switching behaviour is masked by the collective switching. The investigation is done in a generic way using a toy model, showing that the deviation of the SFD can be directly linked with the presence of correlations.

An important consequence is for recording media, which is based on increasing the bit density by decreasing the grains size and by decreasing inter-granular distances. As a consequence the interactions will increase in strength. For these conditions, which are relevant for current and future recording system, the FORC method fails to provide accurate SFD. While this is true for conventional PMR it may be that the higher anisotropy of HAMR media will mean that this is no longer the case, at least in the early stages of HAMR.

Generally speaking, to identify the SFD in the material parameter range beyond the applicability of the FORC method requires inverse problem solving techniques based on physically realistic models, which allow reproducing the relevant correlated switching of particles. Moreover, besides identifying accurate models suitable for interpreting the experimental data, such methods also require establishing uniqueness properties of the identified solutions. One such technique is discussed in the next chapter.

Chapter 6

SFD method: simulation and experiments

Following the presentation of the FORC method for SFD identification, in this chapter the $\Delta H(M,\Delta M)$ method is introduced and compared with the Preisach analysis. We initially discuss the $\Delta H(M,\Delta M)$ method as analysed using a Preisach approach, followed by a more general reference function method [57, 107] based on the kMC model.

The aim of this chapter is to make a comparison between FORC and the $\Delta H(M,\Delta M)$ method using data generated by the kMC model. The ΔH class of methods is directly based on inverse problem solving techniques applied to realistic models of granular media and their accuracy depends on the choice of the model. It is found that both interaction effects and thermal activation must be taken fully into account. The chapter is organised as follows. Firstly the basis of all methods used are described, followed by a comparison of the σ_{SFD} from all approaches. Finally an analysis of experimental data provided by colleagues at Seagate is presented.

6.1 $\Delta H(M,\Delta M)$ for SFD identification

Tagawa et al. proposed a method based on measurements of hysteresis loop and reversal curves started from coercivity [108]. In this case $\sigma_{SFD} = \Delta H_c/1.35$, where ΔH_c is given by the field difference between major and reversal curve at half magnetization. Berger et al developed the $\Delta H(M,\Delta M)$ based on a set of reversal curves [109], which has been generalized to the partially correlated magnetization reversal regime [107].

Both methods, the FORC and $\Delta H(M,\Delta M)$-method, are based on the measurement of hysteresis loops and the corresponding recoil curve (first order reversal curves), and identify the SFD as an inverse problem analogous to identifying the Preisach hysteron distribution in the Preisach models. The method is based on the hysteron model similar to those commonly used for FORC analysis. Each grain is a perfect hysteron with time reversal symmetry. This corresponds to symmetric positive and negative switching fields (no shift field). The measurements are time independent and thermal effects are not considered. The method was developed in the mean field interaction approximation, which is discussed next.

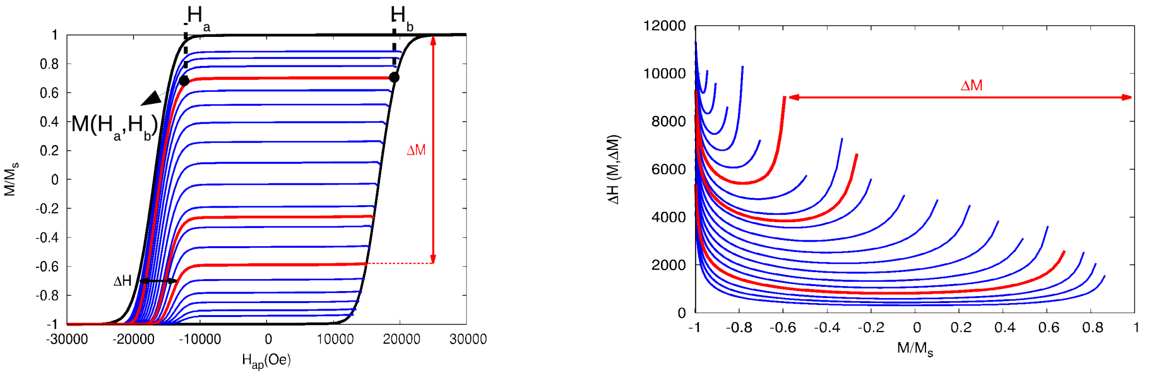

Fig. 6.1 Hysteresis curve and first order reversal curves (a) and the data transformation for the $\Delta H(M,\Delta M)$ method (b).

6.1.1 Mean field approach

Figure 6.1 shows a typical hysteresis curve and the recoil curve for a non-interacting case. Each point on the recoil curve ($M(H_a,h_b)$ is a function of the field when the recoil curve started (H_b) and the field at the point (H_a). For the $\Delta H(M,\Delta M)$-method it is more convenient to replace H_b with the equivalent $\Delta M = M_{sat} - M(H_b)$. Under this consideration the magnetic moment and the corresponding field on the increasing field branch can be written as[110, 111]:

$$M(H) = 1 - 2\int_{-\infty}^{H} D(H_c)dH_c \tag{6.1}$$

$$H(M) = I^{-1}\left[\frac{1-M}{2}\right] \tag{6.2}$$

where I^{-1} is the inverse of the integral function $I(x) = \int_{-\infty}^{x} D(H_c)dH_c$. And for the reversal curves at H_b characterize by ΔM the magnetization is given by:

$$M(H_a,H_b) = 1 - \Delta M - 2\int_{-\infty}^{H_a} D(H_c)dH_c \tag{6.3}$$

$$H_a(M,\Delta M) = I^{-1}\left[\frac{1-M-\Delta M}{2}\right] \tag{6.4}$$

The data is transformed into a field difference at a constant magnetization, e.g. $M(H) = M(H_a, M_b)$, between the major loop and a recoil curve (figure 6.1(b)), in this way removing the mean field interaction contribution. The method links the field difference with the standard deviation of the SFD (σ_{SFD}) [109].

$$\Delta H = H(M) - H_a(M,\Delta M) = \sigma_{SFD} f(M,\Delta M) \tag{6.5}$$

Where the function $f(M,\Delta M)$ can be analytically calculated for mean field interactions. Berger et al. found for Gaussian distribution of SFD the following expression[112, 111]:

$$\Delta H = \sigma_{SFD}\sqrt{2}\left[erf^{-1}(M+\Delta M) - erf^{-1}(M)\right] \tag{6.6}$$

where $erf(x) = \frac{1}{\pi}\int_{-x}^{x} e^{-t^2}dt$ is the error function. For a log-normal distribution[57]:

$$\begin{aligned}\Delta H = &\sigma_{SFD}\left\{exp\left[-\sqrt{2}\tilde{\sigma}erf^{-1}(M)\right] - exp\left[-\sqrt{2}\tilde{\sigma}erf^{-1}(M+\Delta M)\right]\right\}\\ &\left[exp(\tilde{\sigma}^2)\left(exp(\tilde{\sigma}^2)-1\right)\right]\end{aligned} \tag{6.7}$$

where $\tilde{\sigma}$ is related to the asymmetry of the distribution described by the skewness factor $\gamma(\tilde{\sigma}) = (exp(\tilde{\sigma}^2)+2)\sqrt{exp(\tilde{\sigma}^2)-1}$. To determine the SFD, equation 6.5 is fitted to the $\Delta H(M,\Delta M)$ measurement with σ_{SFD} being the fitting parameter.

The above approach works well if the mean field approximation holds and starts to fail with the presence of correlation in the magnetic system, when nearest neighbour exchange and dipole interaction are considered[113].

6.1.2 Reference function $\Delta H(M,\Delta M)$ method: 0K

In the presence of exchange/magnetostatic interaction beyond the mean field approximation the $\Delta H(M,\Delta M)$ method can be extended. Although there is no generic solution, the function, $f(M,\Delta M)$, can be numerically pre-calculated for a set of interaction condition, $f_{ref}(M,\Delta M,H_{exch},H_{mag})$, and used as a reference set to find σ_{SFD} [57, 107]. This is known as the "reference function $\Delta H(M,\Delta M)$ method" and in this work it would be labelled as the $\Delta H(M,\Delta M)$ method, whereas the mean field approach will be labelled as $\Delta H(M,\Delta M)$ mean field. The accuracy of the methods will depend on the model chosen to generate the reference set. A model, which incorporates more elements of the experimental conditions, will reproduce the experimental results with high fidelity but will also increase the complexity of the problem and will lead to a large number of parameters in the reference function, f_{ref}. By simplifying the model, the number of parameters decreases, but possibly also the accuracy of the method will decrease.

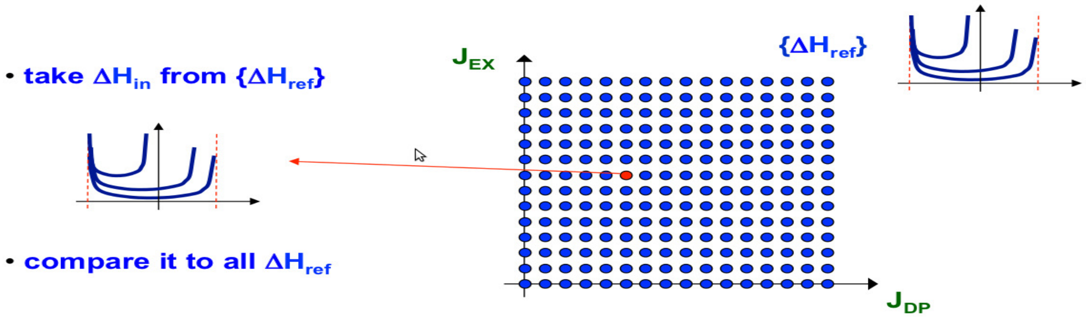

Fig. 6.2 Diagram of the reference method. The input $\Delta H(M,\Delta M)$ measurements are compared with 2 dimensional grid of exchange and dipole interaction precalculated $\Delta H(M,\Delta M)$ curves and the best agreement provide the fitted σ_{SFD} with an estimation of exchange and dipole field. Figure provided by Ondrej Hovorka.

Ondrej Hovorka et.al generated a reference set using the 0K hysteron model with log-normal SFD, adding exchange and magnetostatic interaction [57]. In this model both the magnetostatic and exchange interaction strength can be arbitrarily tuned [57]. The magnetostatic interactions are computed using the dipole approximation for grains in a hexagonal lattice. In this case the reference set will depend on just 3 parameters: magnetostatic interaction, exchange interaction, and the asymmetry in the SFD distribution. To extract the width of SFD, σ_{SFD}, the input ΔH_{in} data are compared with all the ΔH_{ref} data from the reference table set as illustrated in figure 6.2. The degree of agreement between the two is given by:

$$\chi^2 = \sum \left[log(\Delta H_{in}) - log(\sigma_{fit} \Delta H_{ref}) \right] \tag{6.8}$$

where the ΔH_{ref} is the pre-calculated $f_{ref}(M,\Delta M,H_{exch},H_{mag})$. σ_{fit} and ΔH_{ref} are tested to minimize the χ^2. For the minimum value of χ^2, the σ_{SFD} is equal with the corresponding σ_{fit} and ΔH_{ref} describes the input data.

We have carried out a number of calculations comparing the reference function methods for the HDD model presented in previous section (figure 6.3). We use a $\Delta H(M,\Delta M)$ method using a reference table data generated with a Preisach model at 0K described above. The reference table was provided by Ondrej Hovorka [57]. Both FORC (figure 5.7) and $\Delta H(M,\Delta M)$ method (figure 6.3) have significant deviation from the expected value.

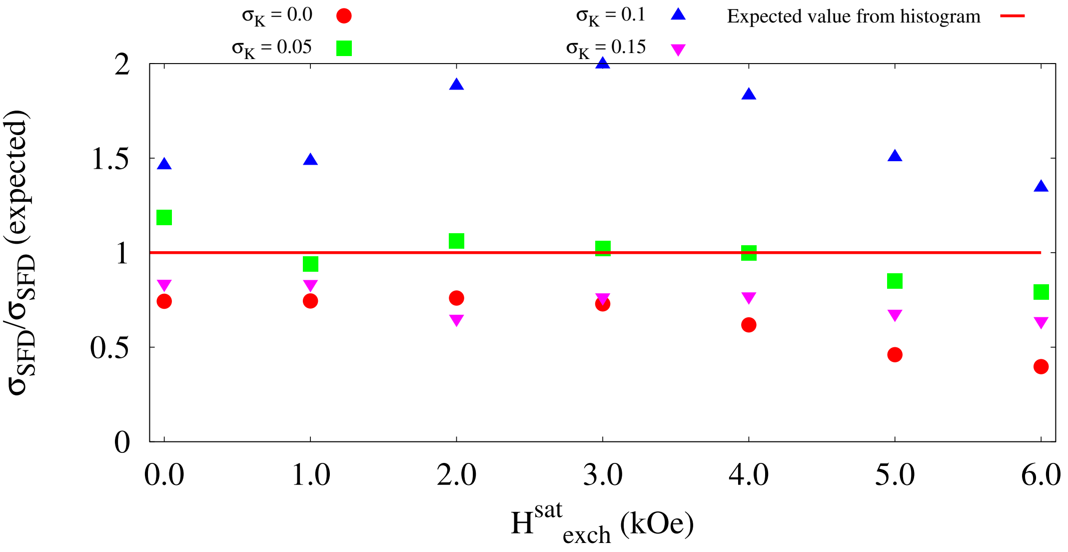

Fig. 6.3 σ_{SFD} as function of exchange strength from the $\Delta H(M,\Delta M)$ methods normalize to the expected value. The results are shown for 4 value of anisotropy distribution, σ_K=: 0.0, 0.05, 0.1, 0.15.

Although the work demonstrate that the $\Delta H(M,\Delta M)$ method can be extended beyond mean field interaction, the role of thermal relaxation, misalignment of easy axis, and the accuracy of interaction are neglected. This elements need to taken into-account if we want to apply for current and future recording devices.

6.1.3 Updated reference table 300K

The simple picture of the 0K Preisach model is insufficient to have a good description of the magnetic behaviour, leading to large deviation of the $\Delta H(M,\Delta M)$ from the expected value. For improving the results we refine the $\Delta H(M,\Delta M)$ method by generating the function $f(M,\Delta M)$ using the kinetic Monte-Carlo model, taking into account the thermal effects and also the complex interactions between grains. The parameters to be considered are: grain size, aspect ratio, volume distribution, spacing between grains, exchange interactions, σ_K. The magnetostatic interactions are computed using the surface integral method and are fixed by the system geometry (grain size, aspect ratio, distribution, spacing between grains), which can be known from experiments (e.g. TEM measurements). The strength of exchange interaction and σ_K are the parameters that will vary in the new reference table. To obtain the new reference set, hysteresis loop and first order reversal curves were calculated using kinetic Monte-Carlo model, with σ_K between 0.0 and 0.15 and the exchange varying between 0 and

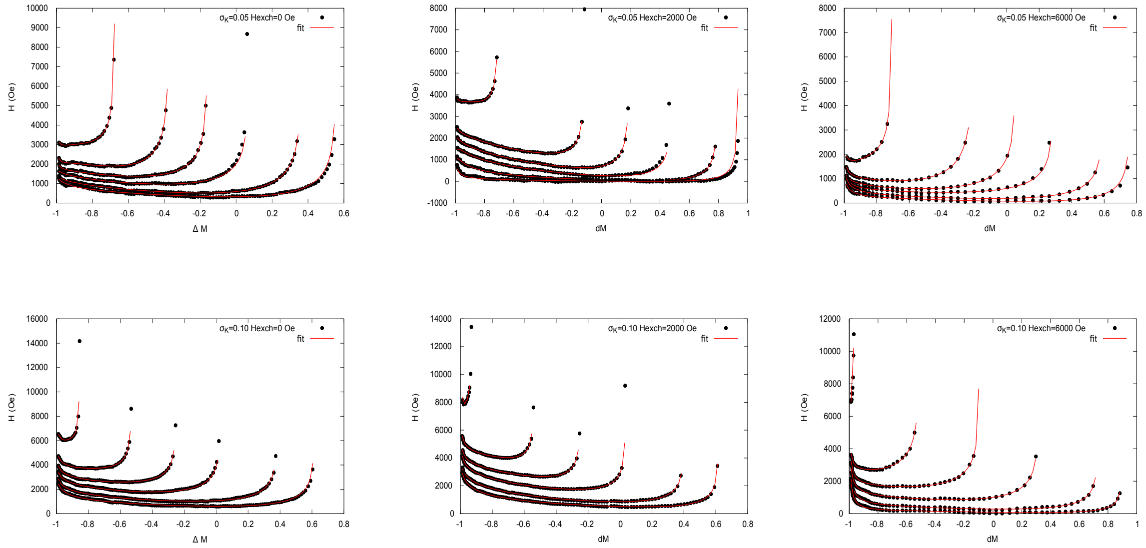

Fig. 6.4 Example of $\Delta H(M,\Delta M)$ data and the corresponding fit for generating the updated reference set.

6 kOe. Then the data was transformed to obtain the $\Delta H(M,\Delta M)$ curves and these curves were fitted to:

$$\Delta H(M,\Delta M) = \sigma_{SFD}\sum_{i=1}^{3}\left[a_i erf^{-1}(M+\Delta M)^{(2i-1)} - b_i erf^{-1}(M)^{(2i-1)}\right] \tag{6.9}$$

The expression 6.9 was chosen as it was successfully used in the previous reference table [107]. This allows reusing the algorithm for any reference set, so it can be extended beyond the current model. Examples of the data and the fit with equation 6.9 are shown in figure 6.4 for two σ_K values, 0.05 top graphs and 0.1 bottom graphs. The simulated data (black dots) is reproduced by the fit function 6.9 (red line) using the sum up to the 3rd coefficient pair (a_i, b_i). The first pair (a_1, b_1) is the dominant one and the next decreases by one order of magnitude. The simulations are done for at least 50 reversal curves, to have a good density of recoil curves (in figure 6.4 just a few recoil curves are displayed for clarity). When an input ΔH_{in} is compared with the reference set, the reversal curves will not necessarily correspond to the same ΔM value. The large number of reversal curves and the use of analytical function to describe them is important for decreasing the error in the interpolation process of matching the reference data points on top of the input data. Here, this new reference set is labelled as updated $\Delta H(M,\Delta M)$. To minimize the number of calculation the reference set was generated for 4 values of σ_K, (0.0,0.05,0.1,0.15) and 7 values of H_exch (0,1,2,3,4,5,6 kOe). This is a

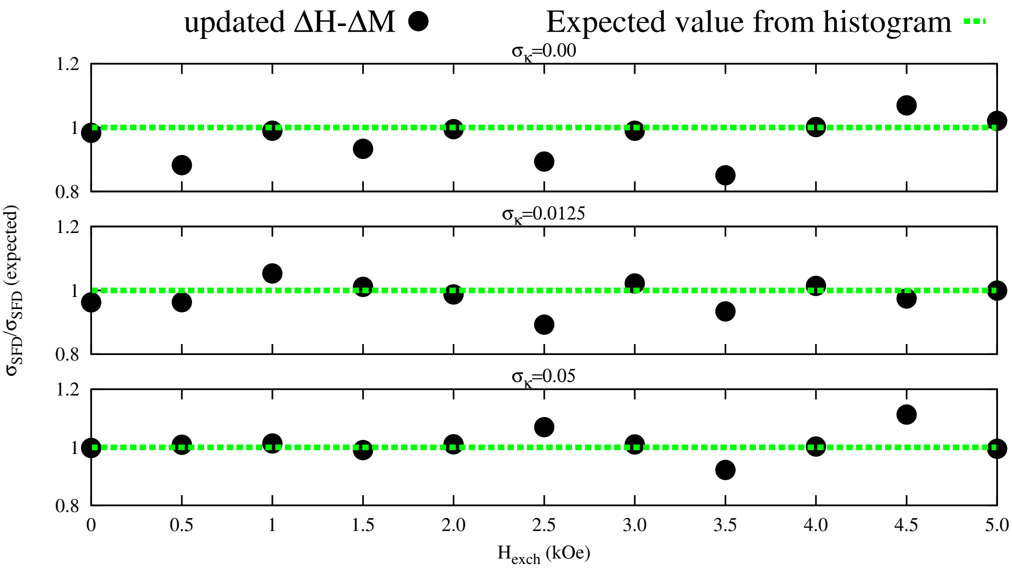

Fig. 6.5 Results for the updated $\Delta H(M,\Delta M)$ reference table.

small number of data, but enough to show that the $\Delta H(M,\Delta M)$ can be successfully extended to more complex magnetic systems.

First, the uniqueness of the new reference set is checked, by making a self consistency test. The updated $\Delta H(M,\Delta M)$ method is applied for simulated data with exchange and σ_K values in the range of the new reference set (figure 6.5). All the points from the reference set are accurately and uniquely reobtained as observed in figure 6.5 for σ_K equal 0.0 and 0.05 and the corresponding H_{exch} values. For exchange values not in the reference table, the σ_{SFD} is obtained with an error up to 20% for σ_K=0.0. Increasing σ_K, the error decreases at small exchange field. For both σ_K and H_{exch} not in the reference set (middle graph in figure 6.5) the σ_{SFD} is also obtained with errors smaller than 15%. A higher accuracy can be achieved by a more dense reference set.

Next we apply the method for same model parameters as in the FORC method case. Figure 6.6 summarises the ability of the FORC and $\Delta H(M,\Delta M)$ method to determine the SFD in a current perpendicular magnetic recording device. The FORC method (green dots) is underestimating the σ_{SFD} for all 4 values of σ_K, 0.0 (figure 6.6a),0.05 (figure 6.6b),0.1 (figure 6.6c), 0.15 (figure 6.6d) and for all values of exchange. Also the $\Delta H(M,\Delta M)$ method based on the 0K hysteron reference set (blue squares) is not consistent, under or over estimating based the σ_K. Just for σ_K=0.05, the value are around the expected values, similar to the results in ref. [57], where a similar model was used. The only difference consist in the dipole approximation used in the ref. [57], leading to a completely different correlations behaviour.

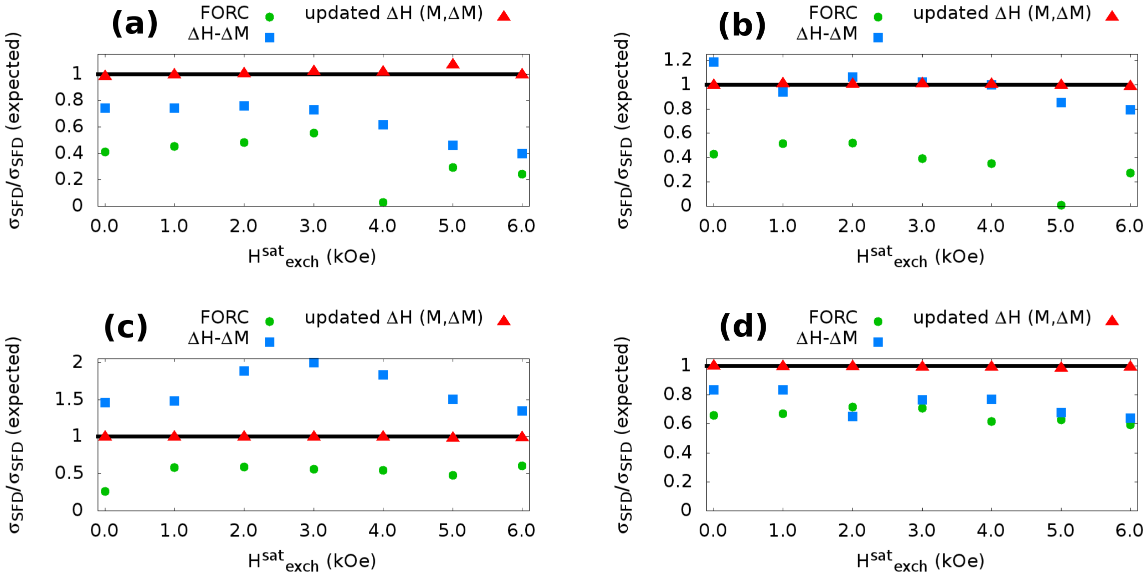

Fig. 6.6 σ_{SFD} as function of exchange strength from the FORC (green circle) and $\Delta H(M,\Delta M)$ (blue square) and updated $\Delta H(M,\Delta M)$ (red triangle) methods normalize to the expected value. The results are shown for 4 value of anisotropy distribution: (a) $\sigma_K = 0.0$, (b) $\sigma_K = 0.05$, (c) $\sigma_K = 0.1$, (d) $\sigma_K = 0.15$.

However, the correct σ_{SFD} can be extracted by considering a more appropriate model to generate the reference set, as the updated $\Delta H(M,\Delta M)$ (red triangles).

6.2 Analysis of experimental data

Next we will apply the FORC and the $\Delta H(M,\Delta M)$ methods for experimental measurements of perpendicular recording media systems. There are 2 sets of experimental data provided by Seagate, labelled C49-C53 (Fig.6.7a) and T23-T29 (Fig.6.7b). Both samples are CGC recording structures, with the recording layer consisting of grains with 8.5nm average grain and 10nm in height. The grains have a log-normal volume distribution with $\sigma_V = 0.33$. The hysteresis loops and first order reversal curves (figure 6.7) are acquired at room temperature using MOKE, with a field sweeping rate of roughly 80kOe/second.

The intergranular exchange is gradually varied by increasing the CGC thickness, with C53 and T23 corresponds to the lowest thickness for each sample. As can be observed from figure 6.7, the magnetostatic interaction dominate, even in the strongest exchange case (C49 and T29). The CGC layer is decreasing both the SFD and coercivity field [114–116]. The coercivity field can be extracted from the hysteresis loop and it is plotted in figure 6.8. As expected, the coercivity of both samples decreases with increasing CGC thickness. This

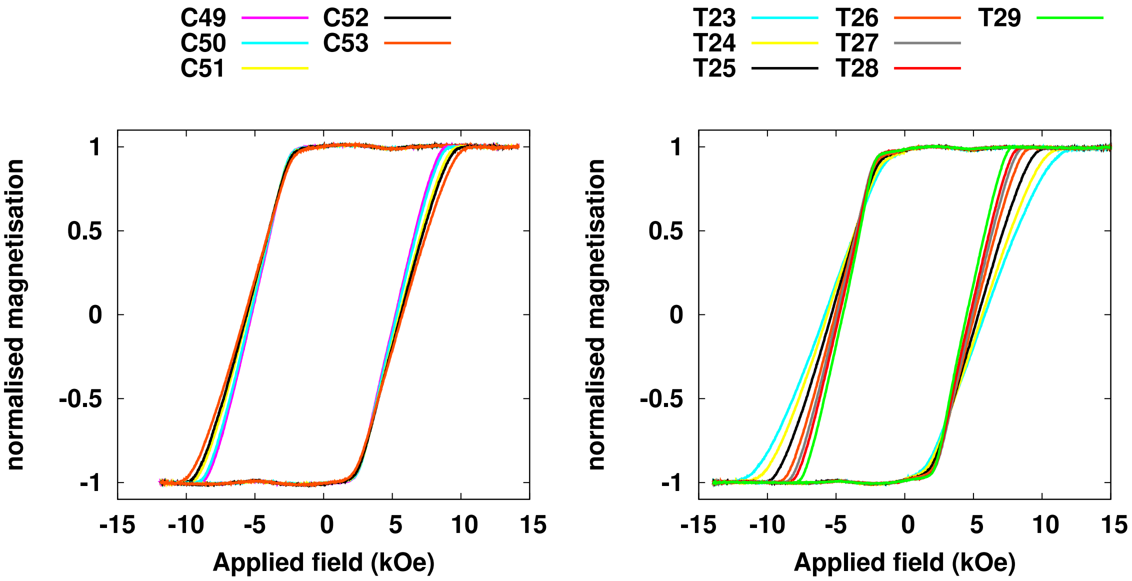

Fig. 6.7 Hysteresis loop and first order reversal curves for two sets of samples.

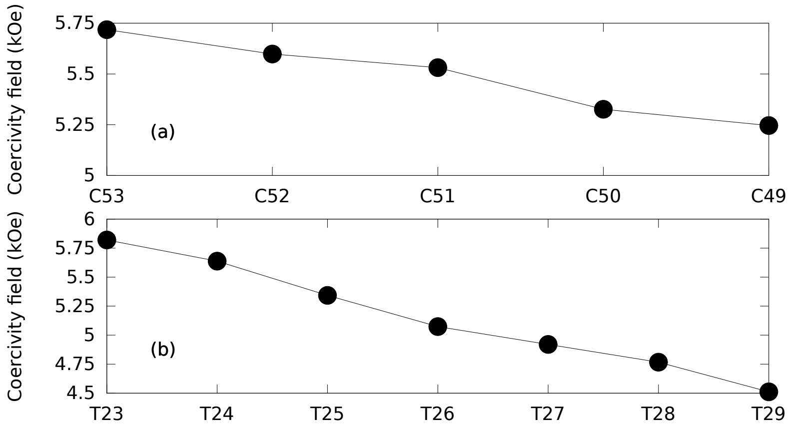

Fig. 6.8 Coercivity field for the two samples. The sample labelled are ordered from the lowest CGC thickness to the highest, from left to right.

corresponds to decreasing index in the label name for C sample and increasing index for the T sample. The "C" samples have a weak exchange variation, in comparison with the T sample as it can be observed from the hysteresis loops in figure 6.7a (for C sample) and figure6.7b (for T sample). Similar trends are for the coercivity in figure 6.8. The variation of the H_c is an indication of the CGC effect as discussed in section 1.3.1. Increasing the soft layer on top of the recording layer, lead to reduction of coercivity as the one observed in figure 6.8 and a decrease of SFD width [117, 30].

The presence of strong interaction is confirmed by the FORC diagrams of the samples. Example of the FORC diagrams for each samples are given in figure 6.9 for C53 sample and in figure 6.10 for T23. The left panel corresponds to the original data and the right panel to the corrected FORC diagram. The original FORC diagram are elongated on the interaction axis (H_u), having similar features with the simulated recording media system in previous chapter in figure 5.9, where based on simulation, the system was strongly correlated. Next, using the corrected FORC diagram, the σ_{SFD} is extracted.

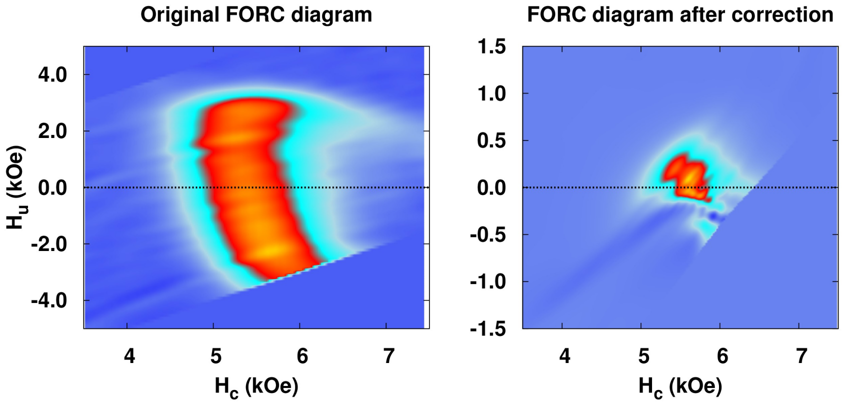

Fig. 6.9 FORC diagram for sample C53.

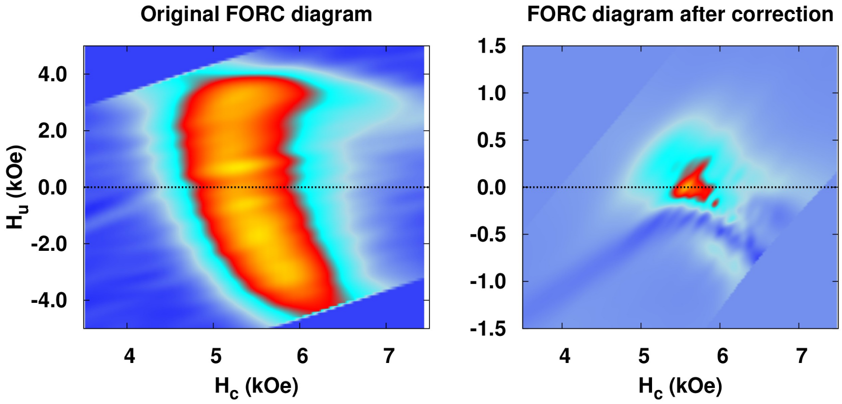

Fig. 6.10 FORC diagram for sample T23.

The σ_{SFD} extracted using the three methods FORC, $\Delta H(M,\Delta M)$ and updated $\Delta H(M,\Delta M)$ are compared and the results are summarised in figure 6.11. There are no experimental values of σ_{SFD} obtained in any other way. The results in figure 6.11 are normalized to the value from the updated $\Delta H(M,\Delta M)$ corresponding to the lowest exchange coupled case for each sample(C53 and respectively T23). The FORC method has for both samples a lower value in comparison with the two $\Delta H(M,\Delta M)$ methods. The results are in agreement with the prediction from the simulation presented in previous section (figure 6.6). For the C samples FORC predicts an increase of the width of the SFD with increasing exchange coupling between grains, whereas for T samples a decrease. The value extracted using $\Delta H(M,\Delta M)$ has a non-monotonic behaviour for both samples similar with the simulation results in figure 6.6. Just the updated $\Delta H(M,\Delta M)$ method provided a monotonic decrease with increasing exchange coupling, providing a similar trend of σ_{SFD} with the coercivity field of the samples, as expected from increasing the CGC layer thickness [116, 117]. The strong variation of the σ_{SFD} for the T sample is due to the larger variation of the CGC layer thickness as indicated by the large decrease of the coercivity.

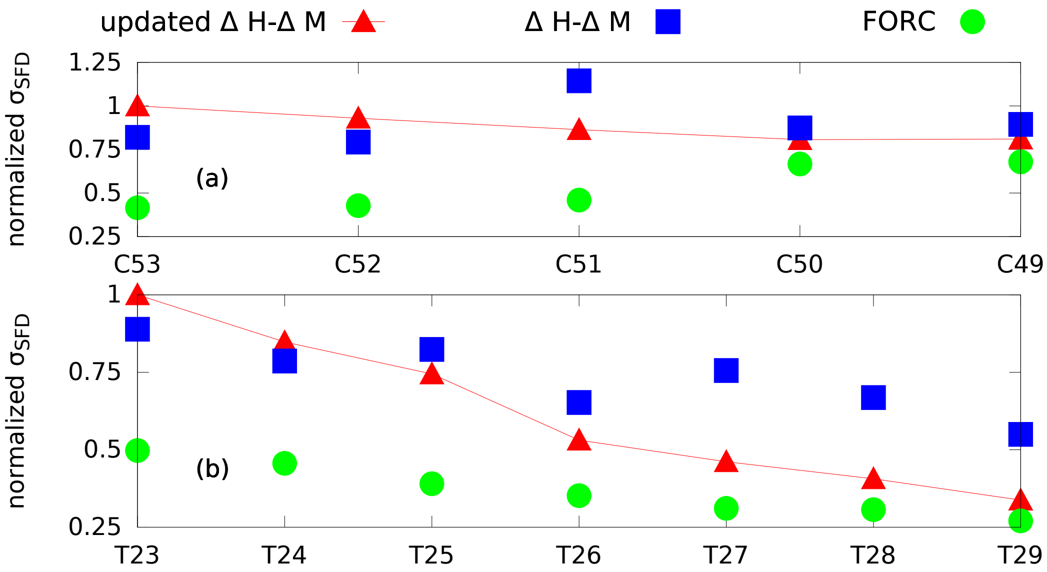

Fig. 6.11 σ_{SFD} for the two samples extracted from the FORC (green circles), $\Delta H(M,\Delta M)$ (blue squares) and updated $\Delta H(M,\Delta M)$ method (red triangles). The values are normalized with respect to the σ_{SFD} of the updated $\Delta H(M,\Delta M)$ method from sample C53 (σ_{SFD}(C53)=573 Oe) and T23 (σ_{SFD}(T23)=924 Oe).

6.3 Conclusion

The $\Delta H(M,\Delta M)$ methods are inverse problem solving techniques, which allow for the SFD width to be extracted from experimental magnetisation data. For the mean field $\Delta H(M,\Delta M)$ method a known analytical function (such as 6.6 and 6.7) is used to fit the experimental data. Although this approach is fast and easy to implement, if the system has correlated behaviour, the mean field approach has the same problems as the FORC method, due to the underlying Preisach model assumptions. However, the method can be extended to have numerically pre-calculated reference set functions. There is in the literature a set of reference functions generated with a 0K interacting model [57]. This was not enough to describe the recording media simulated here. For this reason, we updated the reference set (updated $\Delta H(M,\Delta M)$ method) with functions generated using the kinetic Monte-Carlo model. To extract the SFD width a direct approach employing optimisation techniques based on the grid-search method for fitting is used and the method uniquely recovers the expected SFD.

The $\Delta H(M,\Delta M)$ method, together with the FORC method has been applied to experimental data provided by Seagate. Strongly correlated behaviour is present as indicated by the FORC diagrams. In this case the $\Delta H(M,\Delta M)$ and FORC method can not be used to obtain the SFD and a updated $\Delta H(M,\Delta M)$ method need to be considered. The updated $\Delta H(M,\Delta M)$ method requires to have a reference function for a large set of conditions in terms of interactions, grain size, anisotropy value and distribution.

Solving the problem of identifying the SFD from hysteresis loop measurements in the parameter range relevant in applications such as recording media fundamentally requires applying the inverse problem solving techniques based on models capable of describing complex behaviour, such as thermal effects and correlated switching of particles. The most reliable, but computationally expensive approach, is to carry out a direct fit of the experimental FORC data to a complex model, including the detailed calculation of the interactions such as presented here for the specific example of perpendicular recording media.

Chapter 7

Conclusion

Closed packed granular system such as in recording media leads to large interaction coupling between magnetic grains. In this work, the interaction effects in such system have been investigated. First a granular media model was developed based on the kinetic Monte-Carlo method. This approach allows investigating experimental time scales characteristic of VSM, SQUID and also at larger times corresponding to years and beyond. The model assumes, a single layer of a 2D granular structure generated by Voronoi tessellation. Each grain is described by a mono-domain Stoner-Wohlfarth particle. To investigate the recent PMR systems, the model parameters were discussed with collaborators from Seagate Fremont. The two main focuses of the study were: the effects of interactions on the magnetic behaviour and the ability of extracting the intrinsic SFD from hysteresis based measurement.

First, in chapter 3, an accurate method for computing the magnetostatic interaction in granular systems is presented. The magnetostatic interaction field, created by a grain (source grain) onto another grain (field grain), can be written as a product between a demagnetisation tensor and the magnetisation vector of the source grain. The demagnetisation tensor contains the geometry information such as the shape of the two grains and the relative position between them. In the simpler case, the grains can be consider single points and the demagnetisation tensor is given by the dipole approximation. In chapter 3 we show that the dipole approximation can be used for particles with high symmetry such as spheres or cubes. For general polygon such as those in granular media the dipole approximation becomes inaccurate at short distance when the shape of the grains can not be neglected. Based on Maxwell equations, the magnetostatic field generated by the source grain can be calculated by surface integral over the source grain, which implies a 2-fold integral. The magnetostatic field inside the field grain is non-uniform and an average value over the entire volume of the field grain needs to be considered, leading to a 5-fold integral. For specific grain shapes, the integration can be done analytically , e.g. Newell [66] derived the solution for cuboid shape. If all the grains would have exactly the same shape, a parametrisation of the demagnetisation tensor can be done as function of grain separation. As each grain has a different shape and the grain positions are random, the integration needs to be done numerically for each pair of grains. The 5-fold integral was numerically implemented and successfully tested against known results. The accuracy of the calculation was proportional with the number of discretisation steps. Due to large computational cost of the 5-fold integral, different levels of approximations were studied, eventually leading to the conclusion that the integration over the grain height can be done analytically. Thus reducing the computation cost by at least 2 orders of magnitude and also reducing the numerical errors for the same level of discretisation.

In chapter 4 the exchange and magnetostatic interaction effects on PMR were investigated. One limitation for high-density recording consists of large magnetostatic coupling. For PMR media devices, magnetostatic interaction creates a large demagnetisation field, which decreases the stability of stored information in time. To balance the effect, the media are tuned to include inter-grain positive exchange coupling. A secondary effect of the exchange interaction is the formation of magnetic clusters, or groups of particles that behave collectively. In this case the grains behaviour are effected by the cluster effects. Strong exchange interaction can lead to cluster sizes larger than the bit size and thus increasing the signal to noise ratio in the media. Magnetic correlation and domain width are used in the literature to probe the collective behaviour based on the magnetisation configuration. Here we define, a new approach, based on volume and surface grains. Volume grains are grains with all the nearest neighbours up to order *ni* inside the same domain. If at least one of the nearest neighbours grains has the opposite orientation, the grain is defined as a surface grain. The results are compared with magnetic radial correlation function. Due to the nature of PMR media, where the are basically two possible orientation of the magnetic moment, domain structures appear also in non-interacting system, where there are no magnetic correlations. These domains appear due to purely statistical clustering and lead characteristically to a small presence of volume grains. In the presence of magnetostatic interaction, which want to align neighbour grains antiparallel and form negative correlations, the number of volume grains per domain decreases. If exchange interaction is added, parallel alignment of nearest neighbour is induced more with increasing exchange interaction. As a consequence, nearest neighbours are positively correlated and therefore the number of volume grains increases. The correlation function and the volume grain statistics show similar behaviour for magnetic configuration in zero net magnetisation state obtained at coercivity, after AC demagnetisation or the ground state obtain from long time relaxation simulation. An important observation is that the minimum correlation is obtained for systems under magnetostatic and exchange interaction, corresponding to the case when the average volume grains per domain is similar to the non-interacting case. The non-monotonic behaviour of the magnetisation relaxation curves in zero external field is explained via the anti-parallel coupling from the magnetostatic interaction. The results are reproduced using a simple dimer model.

The intrinsic switching field distribution (SFD), contains the information about the reversal condition for each grain separately. For PMR the intrinsic SFD is modified by intergranular interaction just via the change of local field amplitude and not the field direction. This is true for the applied field perpendicular to the PMR thin film system as discussed at the end of chapter 4. This allows the use of the FORC method and the $\Delta H(M,\Delta M)$-method (chapter 5 and 6) to extract the intrinsic SFD based on the measurement of hysteresis loops and the corresponding first order reversal curves. Although the FORC method was originally created for specific hysteron models, with congruency and wiping out conditions, the approach is used for other systems. Here it is shown that the method cannot obtain the intrinsic SFD if the magnetic grains are correlated. The limitation is a consequence of the Preisach-based interpretation, which neglects the correlations in the system. The $\Delta H(M,\Delta M)$-method is also based on Preisach model and the original formulation has similar limitation. The method consist on comparing (fitting) the measurement with specific functions. The advantage of this method, consist of the fact that the function can be tabulated based on any model and therefore can include different level of complexity present in the experimental system. The disadvantage is that for each new level of complexity added, properties required for inverse problem such as uniqueness need to be studied. For many inverse problem, there are a wide range of model parameters describing the same data and therefore there is not a unique link between the parameters and the data. In chapter 6 it is shown that the unique condition is valid for the kMC model in the parameter range investigated. Both methods are applied for experimental data provide by Seagate. The FORC method, indicates that strong interactions are in the system and for this reason the FORC method can not be successfully applied for identification of SFD. The $\Delta H(M,\Delta M)$ using the kMC parametrisation is applied and shown a decrease if SFD width with increasing CGC layer as expected from literature.

Further Work

The model can be extended:

- To include multi-layer structures.
- To incorporate other reversal mechanism for a two state system such as domain wall motion, which requires just a modification of the energy barrier expression[80].

- by combing with an LLG solver to include the short time scale physics corresponding to the writing process.

The results in chapter 4 suggest that the magnetic configurations obtained at coercivity or in the demagnetisation state obtained from a sequence of AC external field with decreasing amplitude does not corresponds to the ground state of the system. The kMC model allows the investigation of the system ground state, by simulating magnetic relaxation over a large period of time (e.g. $10^{100}s$). Another alternative which has not been investigated here, but can be done is to consider thermal annealing by heating the sample to high temperatures until the system magnetisation vanishes and then cooling slowly back. One work, that can be investigated in the future, is which combination of external field and temperature sequences can the ground state be obtained, considering the experimental conditions.

The long time behaviour of a magnetic recording system is important as the stored information needs to be maintained error free for years. The model and the tools developed here can be used to investigate this aspect in two scenarios:

- Magnetic relaxation experiments of the entire system. The system is magnetised in one direction and the relaxation process is investigated for the entire system.
- Stability in time of recorded information. A specific configuration of bits can be simulated and the long time behaviour investigated.

The relaxation process of the entire magnetic system in zero external field corresponds to years time scales, which experimentally are not accessible. The process can be accelerated by applying a negative external field. Using the thermal fluctuation field introduced by Néel, the magnetisation relaxation curves in negative fields, which are obtained in the short time range (1-100s), can be scaled to the zero external field relaxation curve corresponding to large time scales (years). This technique will allow, experimentally, access to the zero external field relaxation curve. Initial results (theoretically and experimentally) demonstrate the success of the method in weakly interacting systems. For strongly-interacting systems, where a non-monotonic relaxation curve behaviour is observed the scaling approach partially fails. All the relaxation curves are rescaled to a single curve but it does not corresponds to the zero external field relaxation curve. A correction is needed. The dimer system presented in 4 can be used to explore the corrections required for the scaling method to work.

To investigate the stability of stored information, configurations of written bits can be provided to the model followed by simulation of the evolution of the bits over a number of years. This can be combined with models of bit writing and/or reading. The effects of correlation can be studied and the ideal bit size can be explored for different read/write head devices. The amount of exchange interaction to maximised the area density can be explored.

Appendix A

Interaction effects in PMR

Domain configuration

Interaction effects are studied for zero net magnetisation obtain from simulating 3 different experiments: 1) hysteresis loop, 2) ac demagnetisation using an alternating magnetic applied field with decreasing amplitude and 3) magnetisation relaxation in zero applied field. Example of the magnetisation configuration are illustrated in figure A.1. The corresponding domain distribution as function of number of grains per domain is shown in figure A.2. Here the domain is defined as regions of connecting grains with at least one nearest neighbour grains having the same magnetic moment orientation as the domain. The magnetic moment orientation is based on the Z-component.

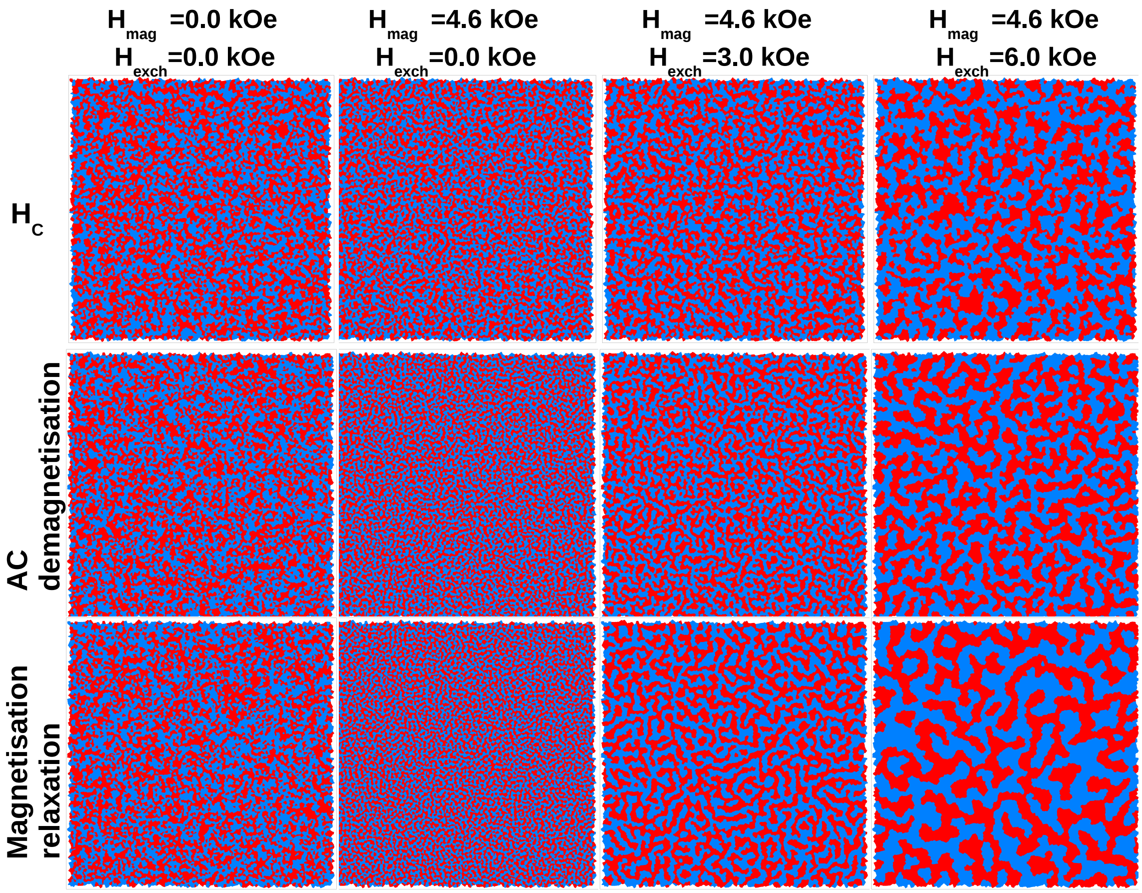

Fig. A.1 Magnetic configuration in zero magnetisation: (top row) obtain from hysteresis loop at coercivity, (midle row) obtain from AC demagnetisation and (bottom row) obtain from magnetisation in zero applied field. First column corresponds to the non-interacting system. The other 3 are for 4.6kOe magnetostatic interaction and exchange interaction of : 0kOe (second column), 3 kOe (third column) and 6 kOe (fourth column). Counter line for correlation values in steps of 0.05 are also shown. The positive m_z value of magnetisation is illustrated with blue and the negative m_z value with red.

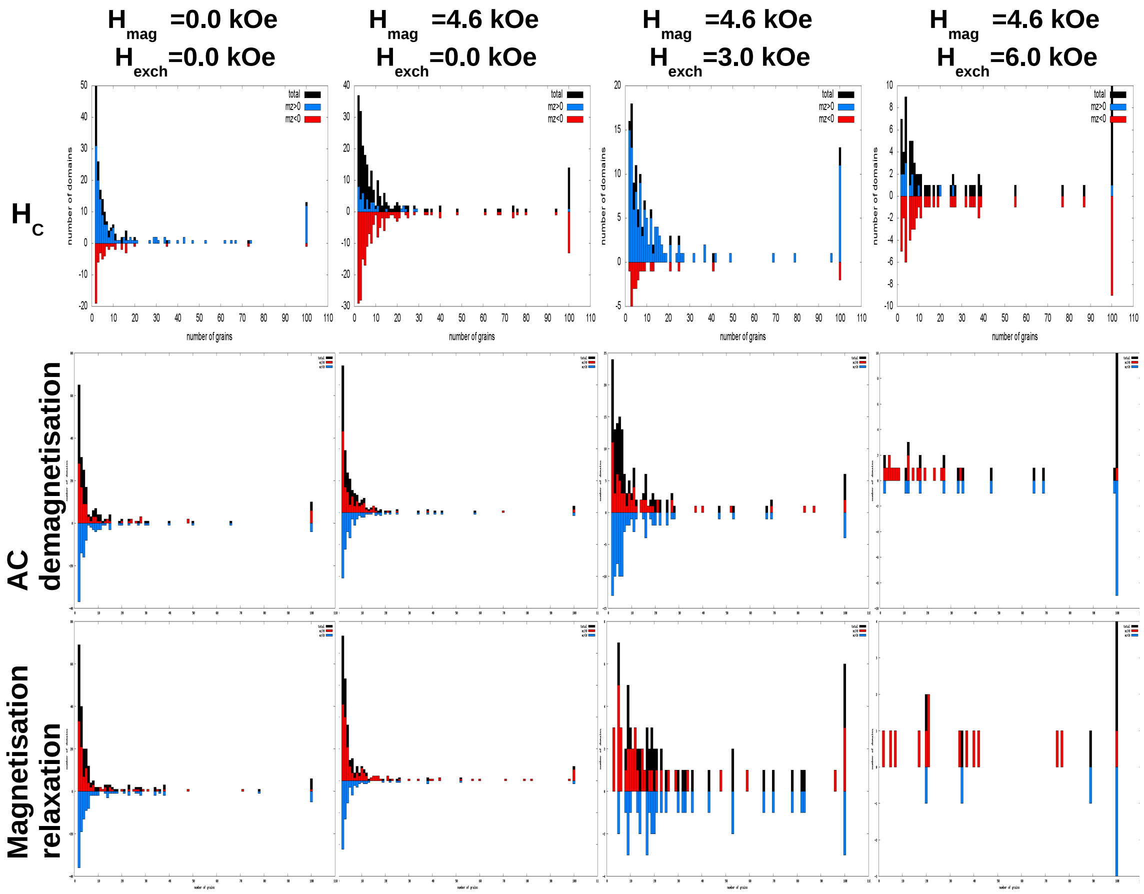

Fig. A.2 Distribution of domains as function of number of grains per domain: (top row) obtain from hysteresis loop at coercivity, (midle row) obtain from AC demagnetisation and (bottom row) obtain from magnetisation in zero applied field. First column corresponds to the non-interacting system. The other 3 are for 4.6kOe magnetostatic interaction and exchange interaction of : 0kOe (second column), 3 kOe (third column) and 6 kOe (fourth column). Counter line for correlation values in steps of 0.05 are also shown. The positive m_z value of magnetisation is illustrated with blue and the negative m_z value with red.

Switching field distribution with applied field direction

Here we consider the effect of applied field orientation in the determination of the extrinsic SFD (eSFD). First we describe again how the eSFD is extracted: "To extract the eSFD for the interacting case, the system is saturated in large positive field. During the hysteresis loop, the switching field corresponds to the first value of applied field in which the grain magnetisation switches between the two stable states. The mean and width of the eSFD is calculated as:

$$< SFD >= |\sum_{i}^{N} H_s^i| \tag{A.1}$$

$$\sigma_{SFD} = \sqrt{\frac{(H_s^i - < SFD >)^2}{N-1}} \tag{A.2}$$

where H_s^i is the switching field of grain i and the symbol $||$ corresponds to the absolute value. " The mean and width of SFD ($< SFD >$, σ_{SFD}) are given in figure A.3b and A.3c. The cases considered here are for 3 values of exchange field: 0 kOe, 2 kOe and 4 kOe (fig. A.3a). Also the non-interacting system is included for comparison. The non-interacting <SFD> is

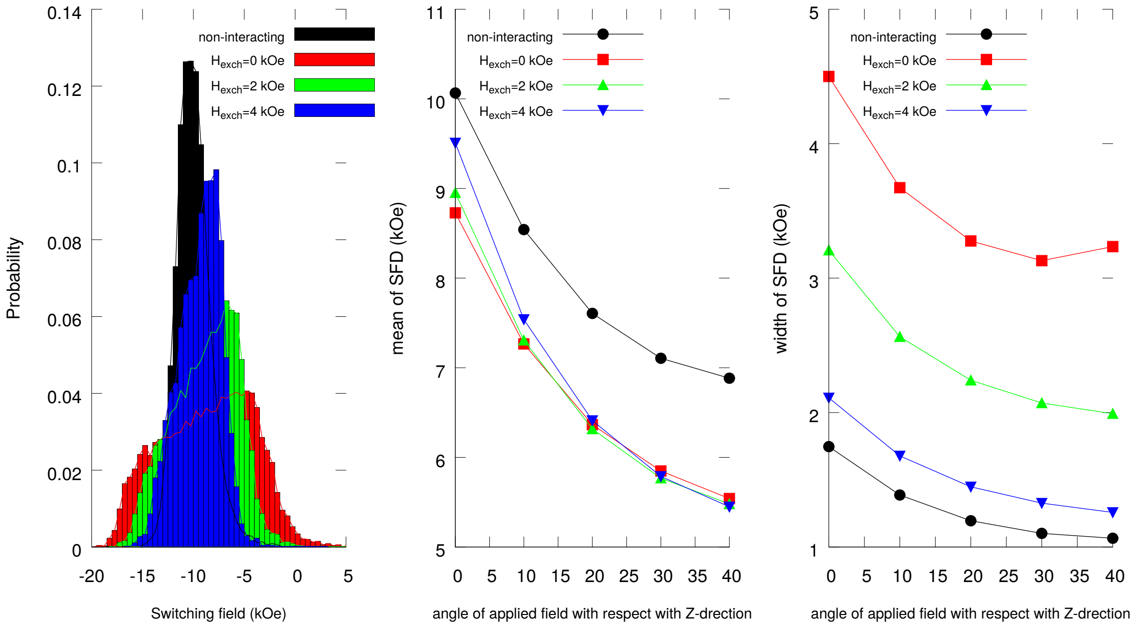

(a) (b) (c)

Fig. A.3 (a) SFD obtained by histogram of the applied field corresponding to the first switching of each particle. The field is applied at angles between 0 and 40 °with respect to the Z-direction. The histogram in (a) are for 0°. The mean (b) and width (c) of SFD are extracted as functions of applied field angle.

approximately 10kOe for the applied field in the easy axis direction and monotonic decrease to 7kOe with increasing the applied field angle. Including magnetostatic interaction leads to a lower value of the mean SFD, in particular for the field parallel with the Z-direction. The exchange interaction compensates the effect, increasing the <SFD> towards the non-interacting case, but just for small deviation of the field from the Z-direction. The interaction effects are less significant for large angle, as there is weak variation of <SFD> between different interaction condition. There is a large difference (around 1kOe) between non-interacting system and the interacting system for all angles. The width of the SFD (A.3c) has a stronger variation due to interactions, with magnetostatic interaction leading to an increased width of the SFD. For exchange interaction of 2kOe and 4kOe the width of SFD decreases towards the non-interacting case and also the angle dependence is very similar to the non-interacting case, a monotonic decrease with increasing applied field angle. The only exception is for the system with 0 exchange interaction, where the minimum width is observed at 30°.

The same investigation as in section 4.3.1 is done also the applied field at 40°. The reversal process for the applied field at 40°is more complex (fig. A.4). The reversal produces not just in different effective field value, but also the orientation of varies. Fig. A.4c illustrates the direction of the effective field at the switching point. The non-interacting results (black dots) are on a single line, just in the field direction, but for the interacting case the is a large dispersion of effective field orientation. The distribution of angle orientation corresponding to the effective field and the relevant statistics are shown in figure A.5 in appendix A.Figure A.4c indicated a significant rotation of the effective field under which the magnetic moment switches to the opposite orientation. Due to this fact, the thermal stability factor and the Z-component of the interaction field are not sufficient to explain the SFD. The magnetostatic interaction rotates the effective field towards the X-axis and thus increasing the angle between the effective field and easy axis. As a consequence the energy barrier is decreased. This leads to a larger amount of grains with the KV value close to 0.5 of the system average or lower to switching in positive applied field (fig. A.4a). Similar with the align case the exchange interaction balance the effect by rotating the effective field towards the Z-direction and implicitly towards the easy axis, thus increasing the energy barrier. This will not be the case of external field applied at angles larger than 45°, for which also the exchange interaction will rotate the effective field towards the X-direction. Nevertheless, it can be notice that the width of the SFD is decreasing with increasing exchange interaction in a similar way as for external field at 0°from Z-direction.

For the SFD obtain above, the effective field is computed and the angle between the effective field and Z-direction is histogram. Example of the histogram for the applied field at

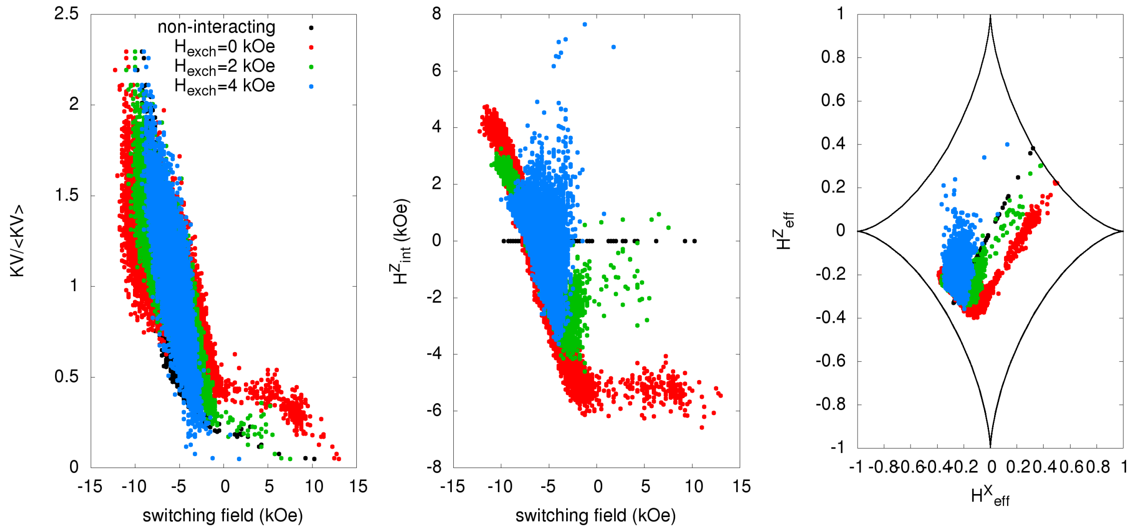

(a) (b) (c)

Fig. A.4 Illustration of the thermal stability factor, Z-component of the interaction field and the orientation of the effective field when each grain switches for the applied field at 40°. (a) Thermal stability factor, KV/k_bT, as function of the switching field. For each grain, the interaction field is extracted at the switching field and the Z-component is given in (b). The orientation of the effective field during at the switching condition is illustrated in (c). The non-interacting system (black) is compared with 4.6kOe magnetostatic interaction and 0kOe exchange field (red), 2kOe (green) and 4kOe exchange field (blue).

0°and 40°from the Z-direction are in figure A.5a and A.5b. The variation of the mean and width of the histogram as function of applied field angle is given in figure A.5c and A.5d. For the applied field in Z-direction, there is a very small variation of the effective field with respect to Z-direction (smaller than 3°). As the external field is applied at larger angles, the effective field creates larger angles at switching and therefore the effective field orientation must be taken into account.

For large angle of the applied field, the orientation of the interaction field is important leading to a more complex description of the SFD. For such cases, separating the intrinsic SFD from the effective SFD is extremely difficult.

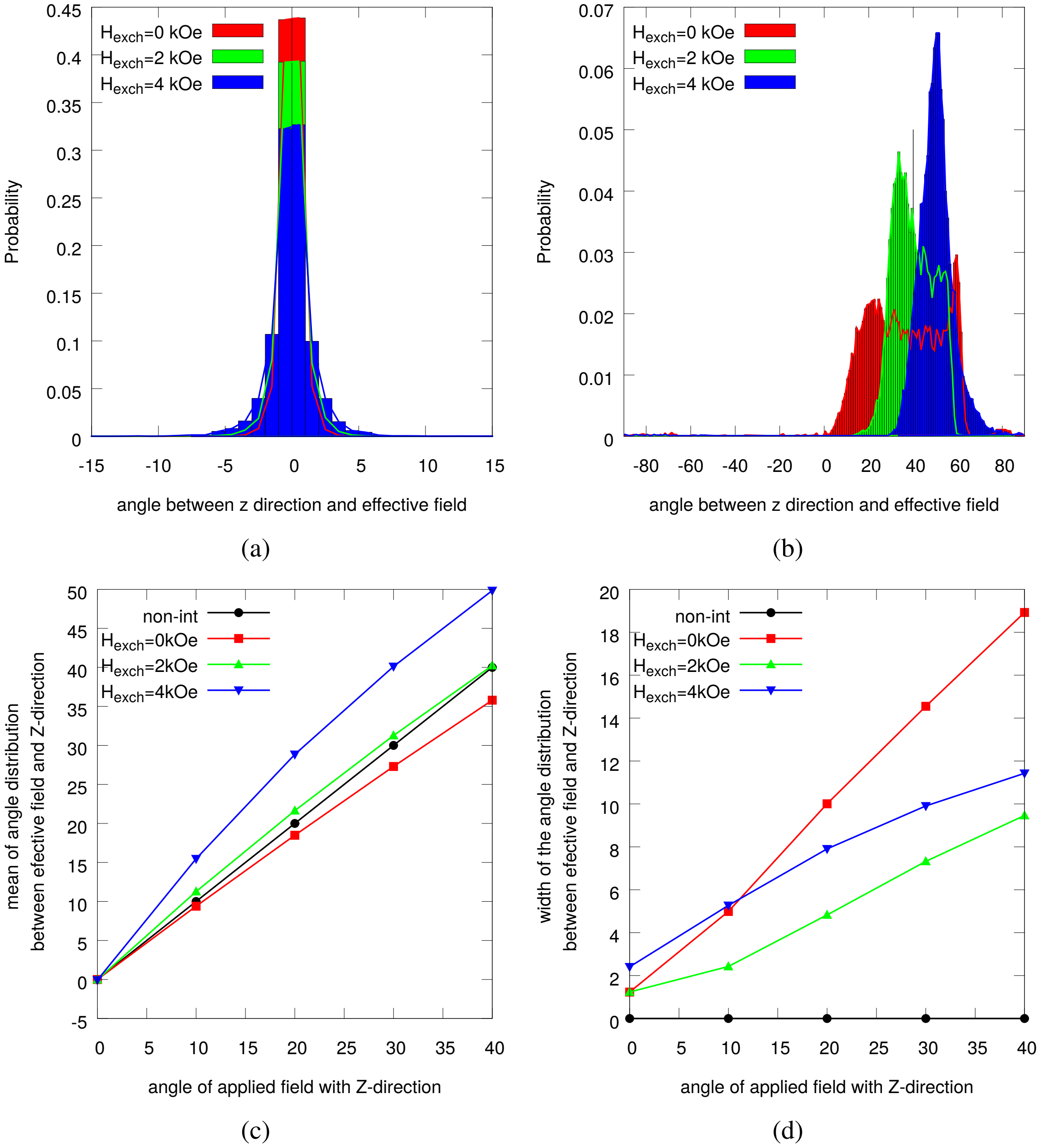

(a) (b)

(c) (d)

Fig. A.5 Distribution of angles of effective field at switching from applied field at 0 °(a) and 40°(b). The mean and width of the angle distribution are given in (c) and respectively (d).

Nomenclature

List of Abbreviation

AC	Alternating current
ASTC	Advanced Storage Technology Consortium
BPM	Bit pattern media
CGC	Coupled granular continuous
CGS	centimetre–gram–second system of units
ECC	Exchange coupled composite
FORC	First order reversal curve
HAMR	Heat assisted magnetic recording
HDD	Hard disk drive
IFD	Interaction field distribution
kMC	Kinetic Monte-Carlo
MC	Monte-Carlo
MOKE	Magneto Optic Kerr Effect
NN	Nearest neighbour
PMR	Perpendicular magnetic recording
RHL	Rectangular hysteresis loop
SFD	Switching field distribution

SI	International System of Units
SNR	Signal to noise ratio
SQUID	Superconducting Quantum Interference Device
SW	Stoner-Wohlfarth
VSM	Vibrating Sample Magnetometer

List of Symbols

χ	magnetic susceptibility
ψ	angle of easy axis
ρ_m	Volumetric charge density
ρ_{ab}	FORC distribution
σ_m	Surface charge density
σ_{SFD}	width of switching field distribution
τ	Neel relaxation time
θ	angle of magnetisation
θ_0	angle of applied field
φ	angle between easy axis and magnetic field
$\vec{\mu}$	magnetic moment
$\vec{r_{x,y,z}}$	the X,Y,Z-component of the position vector r
$\vec{r}$	position vector
$\vec{z_f}$	Z-component of the position vector for the field grain
$\vec{z_s}$	Z-component of the position vector for the source grain
a	Lattice parameter
$C(r)$	Radial magnetic correlation function
$D(H_c)$	Distribution of coercivity fields

$D(H_u)$	Distribution of shift field
D_w	Domain wall width
ds	Number of grains per domain
E_b	Energy barrier
E_z	Zeeman energy
E_{ani}	Anisotropy energy
E_{exch}	Exchange energy
E_{mag}	Magnetostatic energy
$e_{x,y,z}$	versor of X,Y, Z-direction
f_0	Attempt frequency
H	magnetic field
h	height
H_{ex}^{ij}	Exchange field between magnetic moment i and j
H_K	Anisotropy field
H_S	Switching field
H_{ap}	Applied/external field
H_{cr}	Critical field
H_{dipole}	Dipole field
H_{eff}	Effective field
H_{exch}	Average exchange field at saturation
H_{ij}	Magnetostatic field between magnetic moment i and j.
H_{mag}	Average magnetostatic field at saturation
J	Exchange coupling constant
J_{ij}	Exchange constant between spin i and j.

K_0	Zero order anisotropy constant
K_1	First order anisotropy constant
K_2	Second order anisotropy constant
k_b	Boltzmann constant
l_{ex}	Exchange length
M	magnetisation
m	magnetic moment unit vector
M_s	Saturation magnetisation
N_d	Demagnetisation tensor for uniform magnetised sample
ni	order of nearest neighbour
P_V	probability of a volume grain
R_{sd}	Single-domain radius
S_i,S_j	Magnetic moment of atom i, j.
T	Temperature
T_B	Blocking temperature
T_C	Curie temperature
t_m	Measurement time
V	Volume
V_{cr}	Critical volume for superparamagnetic behaviour
W	Demagnetisation tensor
$w_{12,21}$	Escape rates
W_{dip}	Demagnetisation tensor for dipole approximation
W_{dm}	Domain width
<A>	average value of A

D	grain diameter
Ng	Number of grain per cluster for toy model
pkdst	packing density
R	External field sweep rate
U	Scalar potential for magnetostatic field

References

[1] B.D. Cullity. *Introduction to magnetic materials*. Wiley-IEEE Press, 2011.

[2] Ralph Skomski. *Simple models of magnetism*. Oxford University Press, 2008.

[3] D. Jiles. *Introduction to magnetism and magnetic materials*. Chapman and Hall, 1991.

[4] http://www.ieeemagnetics.org/images/stories/magnetic_units.pdf. Accessed: 2017-06-20.

[5] Amikam Aharoni. Introduction to the Theory of Ferromagnetism. *Oxford Sci. Publ.*, I:303, 2007.

[6] W.F. Brown Jr. *Micromagnetics*. John Wiley & Sons, 1963.

[7] Ji Sung Lee, Jin Myung Cha, Ha Young Yoon, Jin-Kyu Lee, and Young Keun Kim. Magnetic multi-granule nanoclusters: A model system that exhibits universal size effect of magnetic coercivity. *Sci. Rep.*, 5(1):12135, dec 2015.

[8] Roger Wood. Future hard disk drive systems. *J. Magn. Magn. Mater.*, 321(6):555–561, mar 2009.

[9] S. N. Piramanayagam. Perpendicular recording media for hard disk drives. *J. Appl. Phys.*, 102(1):011301, jul 2007.

[10] Junichi Yasumori, Yoshiaki Sonobe, S.J. Greaves, and Kim Kong Tham. Approach to High-Density Recording Using CGC Structure. *IEEE Trans. Magn.*, 45(2):850–855, feb 2009.

[11] S. Iwasaki and Y. Nakamura. The magnetic field distribution of a perpendicular recording head. *IEEE Transactions on Magnetics*, 14(5):436–438, Sep 1978.

[12] K K Tham, Y Sonobe, and K Wago. Magnetic and Read–Write Properties of Coupled Granular/Continuous Perpendicular Recording Media and Magnetization Reversal Process. *IEEE Trans. Magn.*, 43(2):671–675, feb 2007.

[13] HJ Richter. The transition from longitudinal to perpendicular recording. *Journal of Physics D: Applied Physics*, 40(9):R149, 2007.

[14] H. J. Richter, A. Lyberatos, U. Nowak, R. F L Evans, and R. W. Chantrell. The thermodynamic limits of magnetic recording. *J. Appl. Phys.*, 111(3), 2012.

[15] http://idema.org/?page_id=416. Accessed: 2017-06-20.

[16] H J Richter, A Y Dobin, R T Lynch, D Weller, R M Brockieo Heinonen, K Z Gao, J J M Xuer, P Asselin, M F Erden, H J Richter, A Y Dobin, R T Lynch, D Weller, and R M Brockie. Recording potential of bit-patterned media Recording potential of bit-patterned media. 222512(2006):2–5, 2016.

[17] Rhys Alun Griffiths, Aled Williams, Chloe Oakland, Jonathan Roberts, Aravind Vijayaraghavan, and Thomas Thomson. Directed self-assembly of block copolymers for use in bit patterned media fabrication. *Journal of Physics D: Applied Physics*, 46(50):503001, 2013.

[18] http://blog.seagate.com/business/seagate-continues-to-lead-as-hamr-technology-advances/. Accessed: 2017-06-20.

[19] Dieter Weller, Gregory Parker, Oleksandr Mosendz, Eric Champion, Barry Stipe, Xiaobin Wang, Timothy Klemmer, Ganping Ju, and Antony Ajan. A HAMR Media Technology Roadmap to an Areal Density of 4 Tb/in^2. *IEEE Trans. Magn.*, 50(1):1–8, jan 2014.

[20] G. Ju, Y. Peng, K. Chang, Y. Ding, A. Q. Wu, X. Zhu, H. Amini, T. J. Klemmer, Y. Kubota, L. Gao, Z. Fan, K. Wang, T. Rausch, P. Subedi, S. Kalarickal, D. Dimitrov, M. Ma, C. J. Rea, D. W. Karns, X. Chen, J. W. Dykes, M. A. Seigler, E. Gage, R. Chantrell, and J. Thiele. High density heat assisted magnetic recording media and advanced characterization: progress and challenges. In *2015 IEEE Magnetics Conference (INTERMAG)*, pages 1–1, May 2015.

[21] Y Sonobe, D Weller, Y Ikeda, M Schabes, K Takano, G Zeltzer, B.K. Yen, M.E. Best, S.J. Greaves, H Muraoka, and Y Nakamura. Thermal stability and SNR of coupled granular/continuous media. *IEEE Trans. Magn.*, 37(4):1667–1670, jul 2001.

[22] Y Sonobe, K.K. Tham, T Umezawa, C Takasu, J.A. Dumaya, and P.Y. Leo. Effect of continuous layer in CGC perpendicular recording media. *J. Magn. Magn. Mater.*, 303(2):292–295, aug 2006.

[23] Y. Sonobe, H. Muraoka, K Miura, Y. Nakamura, K. Takano, H Do, A Moser, B K Yen, Y Ikeda, and N. Supper. Coupled granular/continuous perpendicular recording media with soft magnetic underlayer. *J. Appl. Phys.*, 91(10):8055, 2002.

[24] S.J. Greaves, H. Muraoka, Y. Sonobe, M. Schabes, and Y. Nakamura. Pinning of written bits in perpendicular recording media. *J. Magn. Magn. Mater.*, 235(1-3):418–423, oct 2001.

[25] D. Suess, J. Lee, J. Fidler, and T. Schrefl. Exchange-coupled perpendicular media. *J. Magn. Magn. Mater.*, 321(6):545–554, mar 2009.

[26] D. Suess, T. Schrefl, R. Dittrich, M. Kirschner, F. Dorfbauer, G. Hrkac, and J. Fidler. Exchange spring recording media for areal densities up to 10Tbit/in2. *J. Magn. Magn. Mater.*, 290-291:551–554, apr 2005.

[27] R.H. Victora and X. Shen. Exchange coupled composite media for perpendicular magnetic recording. *IEEE Trans. Magn.*, 41(10):2828–2833, oct 2005.

[28] K. Yu Guslienko, O. Chubykalo-Fesenko, O. Mryasov, R. Chantrell, and D. Weller. Magnetization reversal via perpendicular exchange spring in FePt/FeRh bilayer films. *Phys. Rev. B*, 70(10):104405, sep 2004.

[29] D. Suess, M. Fuger, C. Abert, F. Bruckner, and C. Vogler. Superior bit error rate and jitter due to improved switching field distribution in exchange spring magnetic recording media. *Sci. Rep.*, 6(October 2015):27048, 2016.

[30] Thomas P. Nolan, Bogdan F. Valcu, and Hans J. Richter. Effect of Composite Designs on Writability and Thermal Stability of Perpendicular Recording Media. *IEEE Trans. Magn.*, 47(1):63–68, jan 2011.

[31] Y. Peng, X. W. Wu, J. Pressesky, G. P. Ju, W. Scholz, and R. W. Chantrell. Cluster size and exchange dispersion in perpendicular magnetic media. *J. Appl. Phys.*, 109(12):123907, jun 2011.

[32] X. W. Wu, Yingguo Peng, and Binquan Wang. Magnetic cluster size and cluster size distribution study on perpendicular media. *Appl. Phys. Lett.*, 93(15):152514, oct 2008.

[33] Florin Zavaliche, Bogdan F. Valcu, and Joachim Ahner. Direct measurement of the magnetic cluster size using high-resolution magnetic force microscopy. *IEEE Trans. Magn.*, 51(1), 2015.

[34] Virat Mehta, Tianhan Wang, Yoshihiro Ikeda, Ken Takano, Bruce D. Terris, Benny Wu, Catherine Graves, Hermann A. Dürr, Andreas Scherz, Jo Stöhr, and Olav Hellwig. Extracting magnetic cluster size and its distributions in advanced perpendicular recording media with shrinking grain size using small angle x-ray scattering. *Appl. Phys. Lett.*, 106(20):202403, may 2015.

[35] Binni Varghese, S. N. Piramanayagam, Wee Kiat Lee, and Hang Khume Tan. Noise Characterization of Perpendicular Recording Media by Cluster Size Measurements. *IEEE Trans. Magn.*, 50(5):1–6, may 2014.

[36] C Papusoi, M Desai, and R Acharya. Evaluation of intergranular exchange coupling and magnetic domain size in CoCrPt–SiO X thin films with perpendicular anisotropy. *J. Phys. D. Appl. Phys.*, 48(21):215005, jun 2015.

[37] S. Sato, S. Kumagai, and R. Sugita. Effects of sub-domain structure on initial magnetization curve and domain size distribution of stacked media. *J. Magn. Magn. Mater.*, 377:147–152, mar 2015.

[38] http://www.psi-k.org/codes.shtml. Accessed: 2017-06-20.

[39] http://nmag.soton.ac.uk/nmag/. Accessed: 2017-08-13.

[40] http://math.nist.gov/oommf/. Accessed: 2017-08-13.

[41] http://mumax.github.io/. Accessed: 2017-08-13.

[42] http://www.magpar.net/. Accessed: 2017-08-13.

[43] http://suessco.com/simulations/solutions/femme-software/. Accessed: 2017-08-13.

[44] http://magnetism.eu/43-software.htm. Accessed: 2017-08-13.

[45] E.C. Stoner and E.P. Wohlfarth. A mechanism of magnetic hysteresis in heterogeneous alloys. *Philosophical Transactions of the Royal Society of London. Series A, Mathematical and Physical Sciences*, 240(826):599–642, 1948.

[46] H. Pfeiffer. Determination of anisotropy field distribution in particle assemblies taking into account thermal fluctuations. *physica status solidi (a)*, 118(1):295–306, 1990.

[47] L. D. Landau and E. M. Lifshitz. On the theory of the dispersion of magnetic permeability in ferromagnetic bodies. *Phys. Z. Sowietunion*, 8:153–169, 1935.

[48] T.L. Gilbert. Classics in Magnetics A Phenomenological Theory of Damping in Ferromagnetic Materials. *IEEE Trans. Magn.*, 40(6):3443–3449, nov 2004.

[49] William Fuller Brown. Thermal Fluctuations of a Single-Domain Particle. *Physical Review*, 130(5):1677–1686, 1963.

[50] H.A. Kramers. Brownian motion in a field of force and the diffusion model of chemical reactions. *Physica*, 7(4):284–304, apr 1940.

[51] H. Pfeiffer. Influence of thermal fluctuations on the magnetic properties of particle assemblies. *physica status solidi (a)*, 122(1):377–389, 1990.

[52] R. Chantrell, N. Walmsley, J. Gore, and M. Maylin. Calculations of the susceptibility of interacting superparamagnetic particles. *Physical Review B*, 63(2):024410, December 2000.

[53] L. Breth, D. Suess, C. Vogler, B. Bergmair, M. Fuger, R. Heer, and H. Brueckl. Thermal switching field distribution of a single domain particle for field-dependent attempt frequency. *J. Appl. Phys.*, 112(2):0–4, 2012.

[54] W Wernsdorfer, E. Bonet Orozco, K Hasselbach, A Benoit, B Barbara, N Demoncy, A Loiseau, H Pascard, and D Mailly. Experimental Evidence of the N?el-Brown Model of Magnetization Reversal. *Phys. Rev. Lett.*, 78(9):1791–1794, mar 1997.

[55] Hans Jürgen Richter. The transition from longitudinal to perpendicular recording. *J. Phys. D. Appl. Phys.*, 40(9):R149–R177, may 2007.

[56] D. G. Porter, E. Glavinas, P. Dhagat, J. A. O?Sullivan, R. S. Indeck, and M. W. Muller. Irregular grain structure in micromagnetic simulation. *J. Appl. Phys.*, 79(8):4695, 1996.

[57] O. Hovorka, R. F. L. Evans, R. W. Chantrell, Y. Liu, K. a. Dahmen, and A. Berger. Validation of ΔH(M,ΔM)-technique for identification of switching field distributions in the presence of thermal relaxation. *Journal of Applied Physics*, 108(12):123901, 2010.

[58] Dorin Cimpoesu, Alexandru Stancu, and Leonard Spinu. Micromagnetic simulation of the complex transverse susceptibility in nanostructured particulate systems. *J. Appl. Phys.*, 99(8):30–33, 2006.

[59] D. Choo, Roy Chantrell, R. Lamberton, A. Johnston, and K. O'Grady. A model of the magnetic properties of coupled ferromagneticantiferromagnetic bilayers. *J. Appl. Phys.*, 101(9):31–33, 2007.

[60] http://math.lbl.gov/voro++/download/prev.html. version 0.4.5.

[61] Chris Rycroft. Voro++: A three-dimensional voronoi cell library in c++. 2009.

[62] P. J. Flanders and M. P. Sharrock. An analysis of time-dependent magnetization and coercivity and of their relationship to print-through in recording tapes. *Journal of Applied Physics*, 62(7):2918, 1987.

[63] K O'Grady Roy W Chantrel, G N Coverdale. Time dependence and rate dependence of the coercivity of particulate recording media. 1469:26–29, 1988.

[64] Y. Peng, X. W. Wu, J. Pressesky, G. P. Ju, W. Scholz, and R. W. Chantrell. Cluster size and exchange dispersion in perpendicular magnetic media. *Journal of Applied Physics*, 109(12):123907, 2011.

[65] The parameters were based on private communication with Seagate.

[66] AJ Newell. A generalization of the demagnetizing tensor for nonuniform magnetization. *Journal of Geophysical Research*, 98(7):9551–9555, 1993.

[67] Amikam Aharoni. Demagnetizing factors for rectangular ferromagnetic prisms. *J. Appl. Phys.*, 83(6):3432–3434, mar 1998.

[68] J A Osborn. Demagnetizing factors of the general ellipsoid. *Phys. Rev.*, (h 8), 1945.

[69] private communication with Jim Miles.

[70] Virat Mehta, Tianhan Wang, Yoshihiro Ikeda, Ken Takano, Bruce D. Terris, Benny Wu, Catherine Graves, Hermann A. Dürr, Andreas Scherz, Jo Stöhr, and Olav Hellwig. Extracting magnetic cluster size and its distributions in advanced perpendicular recording media with shrinking grain size using small angle x-ray scattering. *Appl. Phys. Lett.*, 106(20):202403, may 2015.

[71] Tianhan Wang, Virat Mehta, Yoshihiro Ikeda, Hoa Do, Kentaro Takano, Sylvia Florez, Bruce D. Terris, Benny Wu, Catherine Graves, Michael Shu, Ramon Rick, Andreas Scherz, Joachim Stöhr, and Olav Hellwig. Magnetic design evolution in perpendicular magnetic recording media as revealed by resonant small angle x-ray scattering. *Appl. Phys. Lett.*, 103(11):112403, sep 2013.

[72] F. Casoli, L. Nasi, F. Albertini, S. Fabbrici, C. Bocchi, F. Germini, P. Luches, A. Rota, and S. Valeri. Morphology evolution and magnetic properties improvement in FePt epitaxial films by in situ annealing after growth. *J. Appl. Phys.*, 103(4):043912, feb 2008.

[73] N.A. Buznikov and K.N. Rozanov. The effect of stripe domain structure on dynamic permeability of thin ferromagnetic films with out-of-plane uniaxial anisotropy. *J. Magn. Magn. Mater.*, 285(3):314–326, jan 2005.

[74] Michael T. Gastner and Beáta Oborny. The geometry of percolation fronts in two-dimensional lattices with spatially varying densities. *New J. Phys.*, 14(10):103019, oct 2012.

[75] Béla Bollobás and Oliver Riordan. The critical probability for random Voronoi percolation in the plane is 1/2. *Probab. Theory Relat. Fields*, 136(3):417–468, nov 2006.

[76] Hugo Duminil-Copin, Aran Raoufi, and Vincent Tassion. Exponential decay of connection probabilities for subcritical Voronoi percolation in R^d, url = http://arxiv.org/abs/1705.07978, year = 2017. pages 1–8, may.

[77] Abbas Ali Saberi. Recent advances in percolation theory and its applications. *Phys. Rep.*, 578:1–32, may 2015.

[78] H Ebeling and G. Wiedenmann. Detecting structure in two dimensions combining Voronoi tessellation and percolation. *Phys. Rev. E*, 47(1):704–710, jan 1993.

[79] Binbin Ding, Chaolin Li, Meng Zhang, Gang Lu, and Fei Ji. Numerical analysis of percolation cluster size distribution in two-dimensional and three-dimensional lattices. *Eur. Phys. J. B*, 87(8), 2014.

[80] M. El-Hilo, K. O'Grady, and R.W. Chantrell. Fluctuation fields and reversal mechanisms in granular magnetic systems. *J. Magn. Magn. Mater.*, 248(3):360–373, aug 2002.

[81] M. El-Hilo and I. Bsoul. Interaction effects on the coercivity and fluctuation field in granular powder magnetic systems. *Phys. B Condens. Matter*, 389(2):311–316, feb 2007.

[82] R Street and J C Woolley. A Comparison of Magnetic Viscosity in Isotropic and Anisotropic High Coercivity Alloys. *Proc. Phys. Soc. Sect. B*, 69(12):1189–1199, dec 1956.

[83] O. Laslett, Sergiu Ruta, R.W. Chantrell, J. Barker, G. Friedman, and Ondrej Hovorka. Consistent energy barrier distributions in magnetic particle chains. *Phys. B Condens. Matter*, 486:173–176, apr 2016.

[84] O. Laslett, Sergiu Ruta, J. Barker, Roy Chantrell, G. Friedman, and Ondrej Hovorka. Interaction effects enhancing magnetic particle detection based on magneto-relaxometry. *Appl. Phys. Lett.*, 106(1):012407, jan 2015.

[85] O. Hovorka, J. Barker, G. Friedman, and R. W. Chantrell. Role of geometrical symmetry in thermally activated processes in clusters of interacting dipolar moments. *Phys. Rev. B - Condens. Matter Mater. Phys.*, 89(10), 2014.

[86] O. Hovorka, J. Pressesky, G. Ju, A. Berger, and R. W. Chantrell. Distribution of switching fields in magnetic granular materials. *Appl. Phys. Lett.*, 101(18), 2012.

[87] O. Hovorka, R.F.L. Evans, and R.W. Chantrell. Rate-dependence of the switching field distribution in nanoscale granular magnetic materials. *Applied Physics Letters*, 97(6):062504, 2010.

[88] a.P. Roberts, C.R. Pike, and K.L. Verosub. First-order reversal curve diagrams: a new tool for characterizing the magnetic properties of natural samples. *J. Geophys. Res.*, 105(B12):28461–475, 2000.

[89] Christopher R Pike, Andrew P Roberts, Mark J Dekkers, and Kenneth L Verosub. An investigation of multi-domain hysteresis mechanisms using FORC diagrams. *Phys. Earth Planet. Inter.*, 126(1-2):11–25, 2001.

[90] Adrian R Muxworthy. Assessing the ability of first-order reversal curve (FORC) diagrams to unravel complex magnetic signals. *J. Geophys. Res.*, 110(B1):B01105, 2005.

[91] Andrew P Roberts, David Heslop, Xiang Zhao, and Christopher R Pike. Understanding fine magnetic particle systems through use of first-order reversal curve diagrams. *Rev. Geophys.*, 52(4):557–602, dec 2014.

[92] Christopher R. Pike, Andrew P. Roberts, and Kenneth L. Verosub. Characterizing interactions in fine magnetic particle systems using first order reversal curves. *J. Appl. Phys.*, 85(9):6660, 1999.

[93] C. Papusoi, K. Srinivasan, and R. Acharya. Study of grain interactions in perpendicular magnetic recording media using first order reversal curve diagrams. *J. Appl. Phys.*, 110(8):083908, 2011.

[94] Dustin A Gilbert, Gergely T Zimanyi, Randy K Dumas, Michael Winklhofer, Alicia Gomez, Nasim Eibagi, J L Vicent, and Kai Liu. Quantitative decoding of interactions in tunable nanomagnet arrays using first order reversal curves. *Sci. Rep.*, 4:4204, 2014.

[95] I. D. Mayergoyz. Hysteresis models from the mathematical and control theory points of view. *J. Appl. Phys.*, 57(8):3803, 1985.

[96] I. D. Mayergoyz. *Mathematical Models of Hysteresis*. Springer New York, New York, NY, 1991.

[97] Alexandru Stancu, Christopher Pike, Laurentiu Stoleriu, Petronel Postolache, and Dorin Cimpoesu. Micromagnetic and Preisach analysis of the First Order Reversal Curves (FORC) diagram. *J. Appl. Phys.*, 93(10):6620, 2003.

[98] Costin-Ionut Dobrota and Alexandru Stancu. What does a first-order reversal curve diagram really mean? A study case: Array of ferromagnetic nanowires. *J. Appl. Phys.*, 113(4):043928, 2013.

[99] Costin-Ionut Dobrotă and Alexandru Stancu. Tracking the individual magnetic wires' switchings in ferromagnetic nanowire arrays using the first-order reversal curves (FORC) diagram method. *Phys. B Condens. Matter*, 457:280–286, jan 2015.

[100] Michael Winklhofer and Gergely T. Zimanyi. Extracting the intrinsic switching field distribution in perpendicular media: A comparative analysis. *Journal of Applied Physics*, 99(8):08E710, 2006.

[101] private communication with Seagate.

[102] Richard J. Harrison and Joshua M. Feinberg. FORCinel: An improved algorithm for calculating first-order reversal curve distributions using locally weighted regression smoothing. *Geochemistry, Geophys. Geosystems*, 9(5), 2008.

[103] Thomas Schrefl, Tetsuya Shoji, Michael Winklhofer, Harald Oezelt, Masao Yano, and Gergely Zimanyi. First order reversal curve studies of permanent magnets. *J. Appl. Phys.*, 111(7):07A728, 2012.

[104] P. Postolache, M. Cerchez, L. Stoleriu, and A. Stancu. Experimental evaluation of the preisach distribution for magnetic recording media. *IEEE Trans. Magn.*, 39(5):2531–2533, sep 2003.

[105] Bogdan F. Valcu, Dustin A. Gilbert, and Kai Liu. Fingerprinting inhomogeneities in recording media using the first-order reversal curve method. *IEEE Trans. Magn.*, 47(10):2988–2991, 2011.

[106] Aurelian Rotaru, Jin Hee Lim, Denny Lenormand, Andrei Diaconu, John B. Wiley, Petronel Postolache, Alexandru Stancu, and Leonard Spinu. Interactions and reversal-field memory in complex magnetic nanowire arrays. *Phys. Rev. B - Condens. Matter Mater. Phys.*, 84(13):1–9, 2011.

[107] O. Hovorka, Y. Liu, K.a. Dahmen, and A. Berger. On the ability to determine intrinsic switching field distributions from hysteresis loops in the partially correlated magnetization reversal regime. *Journal of Magnetism and Magnetic Materials*, 322(4):459–468, February 2010.

[108] Ikuya Tagawa and Yoshihisa Nakamura. Relationships between high density recording performance and particle coercivity distribution. *IEEE Trans. Magn.*, 27(6):4975–4977, 1991.

[109] A. Berger, Y. Xu, B. Lengsfield, Y. Ikeda, and E.E. Fullerton. $\Delta H(M, \Delta M)$ method for the determination of intrinsic switching field distributions in perpendicular media. *IEEE Trans. Magn.*, 41(10):3178–3180, oct 2005.

[110] Andreas Berger, B. Lengsfield, and Y. Ikeda. Determination of intrinsic switching field distributions in perpendicular recording media (invited). *J. Appl. Phys.*, 99(8):08E705, apr 2006.

[111] Yang Liu, Karin Dahmen, and a. Berger. Determination of intrinsic switching field distributions in perpendicular recording media: Numerical study of the ΔH(M,ΔM) method. *Phys. Rev. B*, 77(5):054422, 2008.

[112] Yang Liu, Karin A. Dahmen, and A. Berger. The role of dipolar interactions for the determination of intrinsic switching field distributions. *Appl. Phys. Lett.*, 92(22):2006–2009, 2008.

[113] Yang Liu, Ondrej Hovorka, Andreas Berger, and Karin a. Dahmen. Effects of nonuniform exchange and magnetostatic interactions on the determination of intrinsic switching field distributions. *Journal of Applied Physics*, 105(12):123905, 2009.

[114] Junichi Yasumori, Yoshiaki Sonobe, S.J. Greaves, and Kim Kong Tham. Approach to High-Density Recording Using CGC Structure. *IEEE Trans. Magn.*, 45(2):850–855, feb 2009.

[115] K K Tham, Y Sonobe, and K Wago. Magnetic and Read–Write Properties of Coupled Granular/Continuous Perpendicular Recording Media and Magnetization Reversal Process. *IEEE Trans. Magn.*, 43(2):671–675, feb 2007.

[116] G. Varvaro and F. Casoli. *Ultra-High-Density Magnetic Recording: Storage Materials and Media Designs*. Pan Stanford Publishing, 2016.

[117] W.M. Li, W.K. Lim, J.Z. Shi, and J. Ding. The effect of capped layer thickness on switching behavior in perpendicular CoCrPt based coupled granular/continuous media. *J. Magn. Magn. Mater.*, 340:50–56, aug 2013.